Energy Conversion and Management 323 (2025) 119263

Contents lists available at ScienceDirect

Energy Conversion and Management

journal homepage: www.elsevier.com/locate/enconman

Research Paper

Multi-criteria decision-making optimization of a two-staged solar power plant for low radiation zone through the social decision units

Damla Kilic Erikgenoğlu [a], Oguz Arslan [a,*], Asli Ergenekon Arslan [b]

[a] Bilecik Şeyh Edebali University, Faculty of Engineering, Department of Mechanical Engineering, Bilecik, Turkey
[b] Quality Control in Manufacturing Programme, Vocational School, Bilecik Seyh Edebali University, Bilecik, Turkey

ARTICLE INFO

Keywords:
Low solar radiation
Multi-criteria decision-making
Social aspects
Two-stage solar power plant

ABSTRACT

The effective use of renewable energy has been the most common problem of the last few years. The optimal designs of renewable energy systems are the most crucial issue among these problems. However, the optimal points can differ according to the perspectives. In this study, the effects of the different social aspects were investigated on the optimal design of the two-staged solar power plant operating under low solar radiation. In this regard, three social perspectives were handled to optimize the design parameters, including investor, engineering and consumer sights. Thus, different system designs were formed considering different thermodynamical parameters, solar radiation values, and working fluids. The formed designs were then thermodynamically analyzed through energy and exergy methods and economically analyzed through the net present value (NPV) method to obtain the input and output values to determine the optimal points. Finally, the efficiency analysis technique with output satisficing (EATWOS) analysis was handled for three different social aspects to make a decision on the optimal system. The social aspects were included in the optimization through the analytical hierarchic process (AHP) for inputs and outputs. The results show that the social perspectives have essential effects on the optimal designs of the energy systems. As a result, the system's energy and exergy efficiency for the investor basis were determined as 20.88 % and 22.42 %, respectively. This system can produce 93.55 MW of power generation with a profit of 103 million US$ at the end of 20 years. The system's energy and exergy efficiency for the engineering basis were determined as 20.56 % and 22.08 %, respectively. This system can produce 71.17 MW of power generation with a profit of 80 million US$. The system's energy and exergy efficiency for the consumer basis were determined as 19.65 % and 21.09 %, respectively. This system can produce 88.03 MW of power generation with a profit of 92 million US$.

1. Introduction

Increasingly, there is a global shift toward cleaner and renewable energy sources to reduce greenhouse gas emissions and mitigate climate change. This transition involves improving energy efficiency, promoting renewable energy technologies, and exploring innovative solutions to sustainably meet the growing energy demand. Therefore, research on clean and renewable energy sources, such as wind, solar, geothermal, and biogas, which can be an alternative to fossil sources, has increased in the last decades. Solar energy draws attention since it is an endless, clean, and accessible resource.

One of the most beneficial ways to use solar energy is concentrated solar collectors, which collect the sun's rays coming to the surface in a particular area. Many types of concentrated solar collectors exist, such as parabolic troughs, central receiver towers, linear Fresnel, and paraboloidal dishes. Parabolic trough solar collectors (PTSC) are widely used in power plants due to their lower cost in comparison to other collector types [1,2]. PTSC enables to evaluate the solar energy obtaining working fluid with higher temperatures up to 400C [3,4] depending on its structural technology and allows a continuous and stable power source through the integration with a thermal energy storage (TES) unit [5], preventing the daily and seasonal fluctuations. The higher outlet temperature of PTSCs enables the use of water as the working fluid in the steam Rankine cycle (SRC) with a relatively higher efficiency [6,7]. However, there is still potential to increase the system efficiency since SRC waste heat is available depending on the thermodynamic working conditions [8]. In their previous study, the authors investigated the single-staged solar power system designed for the low radiation zone [9]. The system is designed in a combination of solar

* Corresponding author.
E-mail address: oguz.arslan@bilecik.edu.tr (O. Arslan).

https://doi.org/10.1016/j.enconman.2024.119263
Received 7 July 2024; Received in revised form 14 October 2024; Accepted 9 November 2024
Available online 19 November 2024

Nomenclature

A	area (m^2)
b	distance between plates (m)
B_t	cash flow
Bo	Bond number
c_p	specific heat (kJ/kgK)
C	cost (US$)
CEPCI	chemical engineering plant cost index
CR	concentration ratio
D	diameter (m)
e	baffle spacing (m)
$\dot{E}$	energy (kW)
$\dot{E}x$	exergy (kW)
F_{BM}	bare module
F_R	heat removal factor
F'	collector efficiency factor
G	mass flux (kg/m^2s)
h	enthalpy (kJ/kg), heat transfer coefficient (W/m^2)
H	daily solar radiation (W/m^2), height (m)
H_0	extraterrestrial radiation (W/m^2)
I	hourly solar radiation (W/m^2)
k	thermal conductivity (W/m°C)
K_t	clearness index
l	wall thickness (m)
L	length (m)
m	mass (tons)
$\dot{m}$	mass flow rate (kg/s)
M	quantity of coal
n_{pass}	number of passes
N	number of PTSC
N_P	number of plates
NCV	net calorific value
NPV	net present value
Nu	Nusselt number
P	pressure (kPa)
PR	tube pitch ratio
r	radius (m), discount rate (%)
R	thermal resistance
Re	Reynolds number
R''_f	fouling factors
s	entropy (kJ/kgK)
S	sunshine duration
S_0	day length
SI	sustainability index
t	plate thickness (m)
T	temperature (°C)
U	heat transfer coefficient (W/m^2 °C)
U_L	coefficiency of collector heat loss (W/m^2 °C)
V	volume (m^3)
Z	altitude of site
$\dot{Q}$	heat energy (kW)
W	width (m)
$\dot{W}$	power (kW)

Greek Symbols

α_r	absorptivity of receiver
γ	correction factor for diffuse radiation
γ_x	environmental parameter
δ	declination angle
ε	exergy efficiency (%)
η	energy efficiency (%)
μ	dynamic viscosity (Pa·s)
θ	incidence angle, tube layout angle
θ_z	zenith angle
ρ	density (kg/m^3)
σ	surface tension (N/m)
τ_{cover}	transmissivity of the cover glazing
τ_{PTSC}	effective transmissivity of PTSC
φ	latitude angle
ψ	specific exergy (kJ/kg)
ω	hour angle
ω_s	sunset-hour angle

Subscripts

0	dead state
a	ambient, aperture
b	beam or direct normal irradiation
c	cold
cr	critical
d	diffuse, Destruction
h	hot
i	inside
l	lost
m	moving surface
o	outside
P	pump
r	receiver
s	shell and tube
t	tank, total, tube
T	turbine
u	useful

Abbreviations

AHP	analytical hierarchic process
CST	cold storage tank
DNI	direct normal irradiation
EATWOS	efficiency analysis technique with output satisficing
GDM	General Directorate of Meteorology
HE	heat exchanger
HST	hot storage tank
MCDM	multi-criteria decision-making
ORC	organic Rankine cycle
PB	power block
PTSC	parabolic trough solar collector
SF	solar field
SRC	steam Rankine cycle
TES	thermal energy storage

fields (SF), including PTSC, TES, and power blocks (PB), under 24-hour operating conditions without any external energy source. As a result, they determined that the system with SRC provided the optimum design with the highest net present value (*NPV*). The optimum system's energy, exergy, and economic analysis results are reported as 10.19 %, 10.94 %, and 9.012 million US$, respectively. Although it is possible to design an economically feasible system operating under low solar radiation, the authors indicated that it was possible to increase efficiency by integrating a second cycle operating under lower thermodynamical conditions.

Two-staged cycles were developed to evaluate the waste heat released to the environment and increase the system efficiency, and these cycles became the focus of attention for researchers [10]. Alkassem [11] analyzed a power plant with combined Brayton and Rankine

cycles integrated into the central receiver solar collectors. The results reported that the hybrid system provides a lower energy cost and enhances annual generation. Bahari et al. [12] developed a PTSC-based combined power cycle consisting of a regenerative SRC and an organic Rankine cycle (ORC). As a result, the optimum cycle exergy efficiency and levelized cost of electricity production at the best design point were determined as 63.89 % and 0.153 USD/kWh, respectively. Li et al. [13], in their study, proposed an ORC-SRC based on solar energy. The combined cycle using a mixture of biphenyl and diphenyl oxide as the working fluid in the ORC was reported to achieve a maximum efficiency of 45.3 %. Khandelwal et al. [14] performed a thermodynamic analysis of a combined power cycle based on PTSC with a cascaded TES system for different heat transfer fluids. Nazari et al. [15] performed the thermodynamic and exergo-economic analysis of the combined SRC and ORC. The use of R152a in the combined cycle was reported to have the best thermodynamic performance. Cao et al. [16] investigated a supercritical CO_2 Brayton and organic Rankine (ORC) combined cycle based on solar energy utilization. In the system developed for a region with a solar radiation value over 1400 kWh/m^2, the optimum efficiency and net power were determined as 35.07 % and 16.63 MW, respectively. Li et al. [17] investigated the system with the two-stage SRC and ORC cycles designed using PTSC. The analysis was conducted for a region with a direct normal irradiation (DNI) of 800 W/m^2, and the system efficiency was determined to be 15.62 %. Mirjavadi et al. [18] examined the comparison of two-stage SRC-ORC and SRC-Kalina cycles. It was stated that the system with the Kalina sub-cycle was superior to the system with the ORC sub-cycle designed for the region with a DNI of 750 W/m^2. Habibi et al. [19] presented a hybrid system consisting of a partial evaporation SRC, an ORC, and a TES. The system was driven by PTSC and was investigated from the energy and exergoeconomic aspects. The proposed system's net power output and exergy efficiency were determined to be 782 kW and 18.61 %, respectively. In the previous study of the authors [9], they indicated that single-staged designs are more effective even when the solar radiation values are relatively lower (approximately DNI of 500 W/m^2) compared to other PTSC studies in the literature (DNI of 750–1000 W/m^2). Although SRC was discovered as the optimal solution for the handled low radiation zone, there is still potential to be evaluated in ORC. In this study, the applicability of SRC-ORC combined cycles to improve the efficiency of PTSC-driven power generation systems operating under low solar radiation values was investigated. In this regard, a two-staged solar thermal power plant, including the components of SRC and ORC, was explicitly designed for areas with low solar radiation. A region with the highest DNI of 541 W/m2 was chosen as the study area. The system's performance was evaluated from the thermodynamic perspective, as well as economic viability and environmental impact. Since the most critical challenge of a solar power plant is radiation fluctuations and how to provide the energy needed to produce steam during the night or on cloudy days, a dynamic analysis was conducted for a complete year to create a realistic model through the analytical calculation prepared by Excel.

The other important point is to make a decision on the optimal point amongst the parametrically performed designs considering the outputs such as efficiency, power generation and economics [20,21]. There are many methods to decide on the optimal point, including machine learning and multi-objective [22–24]. These methods were successfully applied to the solar power systems. Ehsan et al. [25] optimized a dry-cooled supercritical concentrated solar power (s-CSP) plant to maximize the power output. All the components were analyzed and sized in their study considering the climatic conditions. As a result, they conducted the optimal sizes of the system components, such as the TES unit, cooling tower and solar field, through the parametrical analysis. Boukelia et al. [3,4] conducted an optimization study of a parabolic trough solar thermal plant using an artificial neural network (ANN) tool. They successfully applied to generate the new system designs with different thermodynamical parameters. The optimal point was made based on the economic indicators of the designs. Although the developed model is helpful, it has some difficulties from the multi-objective perspectives. Turja et al. [26] conducted a multi-objective optimization of an s-CSP plant. They used machine learning algorithms such as artificial neural network (ANN) and the genetic algorithm. Finally, they used the technique for order of preference by similarity to ideal solution (TOPSIS) as the multi-criteria decision-making (MCDM) method for multi-objective optimization. This application is a helpful tool for optimizing the thermodynamic parameters on the forecasting basis of the systems. However, the separate effects of the parameters are significant for this kind of analysis. Arslan et al. [27] used the efficiency analysis technique with output satisficing (EATWOS) to decide on the optimal design of an ORC plant. In this study, each parameter's effecting degree (weight) was concluded equally in the analysis. The equal weight could be effective when the parameters are selected as the same kind such as temperature or pressure. When different types of parameters are used, the weights of the parameters should be carefully determined. Arslan et al. [28] included the analytical hierarchic process (AHP) in EATWOS to determine the weights of outputs. So, AHP was successfully used to measure the qualitative effects. Since an expert view was included in the MCDM tool, the analysis was successfully applied for the optimization.

The determination of the optimal designs of an energy system can differ depending on the targets and perspectives. At this point, the social concerns could be practical on the output of a system design affected by

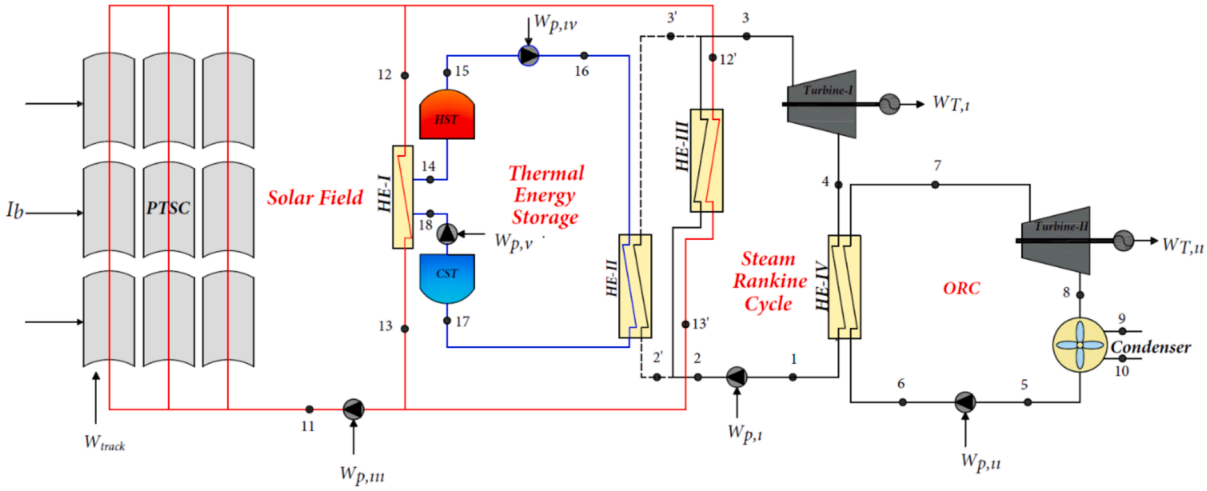

Fig. 1. Schematic diagram of the system.

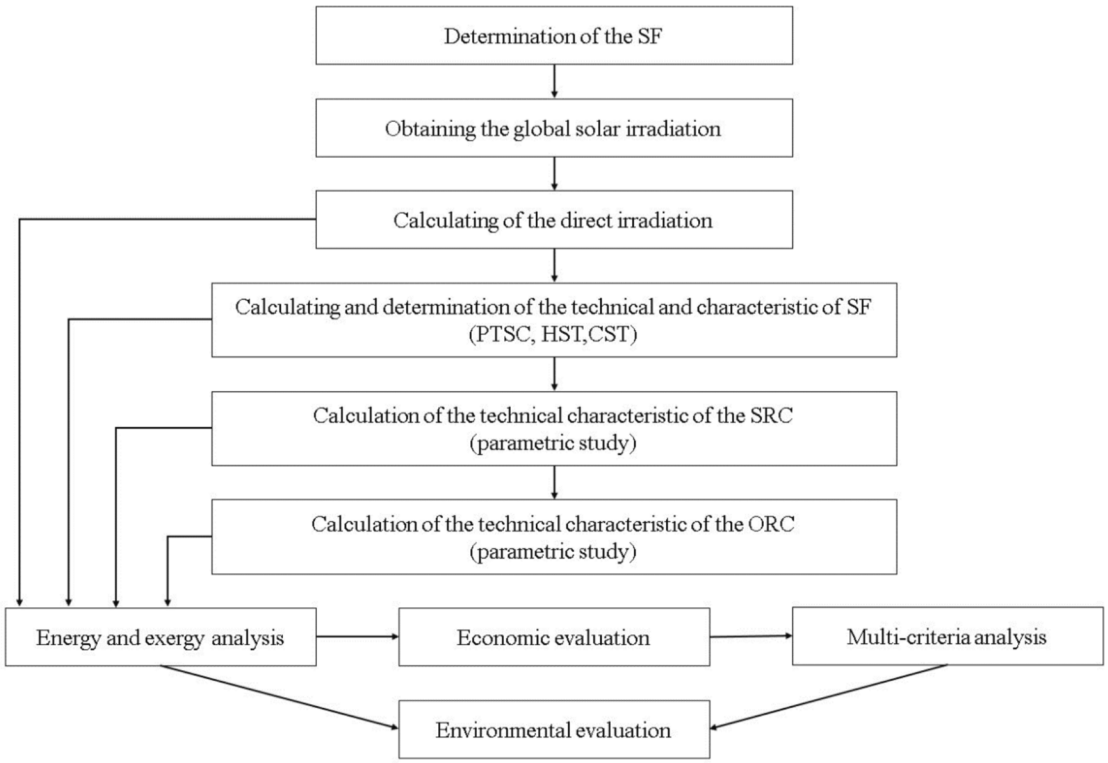

Fig. 2. Calculation flow chart.

Table 1
Technical properties of PTSC [9,31].

PTSC	Value
$D_{o,r}$(m)	0.07
$D_{i,r}$(m)	0.066
U_L(W/m°C)	3.82
h_{fi}(W/m^2)	300
k(W/m °C)	16
τ_{cover}	0.90
τ_{PTC}	0.94
α_r	0.87
γ	0.95
W(m)	5.76
L(m)	15
CR	47
N	15,489

input parameters. An investor aims to get more benefits with less investment cost, whereas an engineer aims for the highest generation with the highest efficiency. The cost issues are related to efficiency for an engineering approach since higher efficiency means less cost at the optimal point. However, a consumer deals with the power tariffs he must pay. Therefore, according to the social aspects, there would be different optimums for the energy plants. In this study, the effects of the social aspects on the optimal design were investigated for the two-staged solar power plant operating under low radiation. Three social aspects, including the investor, technical (engineering), and consumer views, were investigated in this regard to make a decision on the optimal system to draw a path for governors and decision-makers. The efficiency analysis technique with output satisficing (EATWOS) analysis was handled for three different social aspects to make a decision on the optimal system. The social aspects were included in the optimization through the analytical hierarchic process (AHP) for inputs and outputs since it enables the illustration of the social parameters in numeric depending on their importance scaling. The input and output values were obtained from the power plant's formed design. In this regard, 945 designs operating with R600a and 630 designs operating with R152a were formed according to climatic conditions. The plant was thermodynamically investigated for different parameters, including solar radiation, investment cost, temperature and pressure scales to form the input data. So, the outputs, including energy efficiency, exergy efficiency, sustainability index (SI), net power generation, and net present value (NPV) of the system, were obtained to make a decision on the optimal solution. Solar radiation related to installation points was performed at different levels, including the minimum, moderate, and maximum, for the hourly dynamic evaluation for a complete year.

2. System Description

The system model was created specifically for the environmental conditions of Bilecik province (40.1° latitude and 29.9° longitude) in Turkey, where the annual solar radiation value is relatively low, ranging from 1400 to 1550 kWh/m^2 with a maximum direct normal radiation of 541 kW [29]. Given the mountainous and rugged terrain of Bilecik, installing a power plant in the area presents specific challenges.

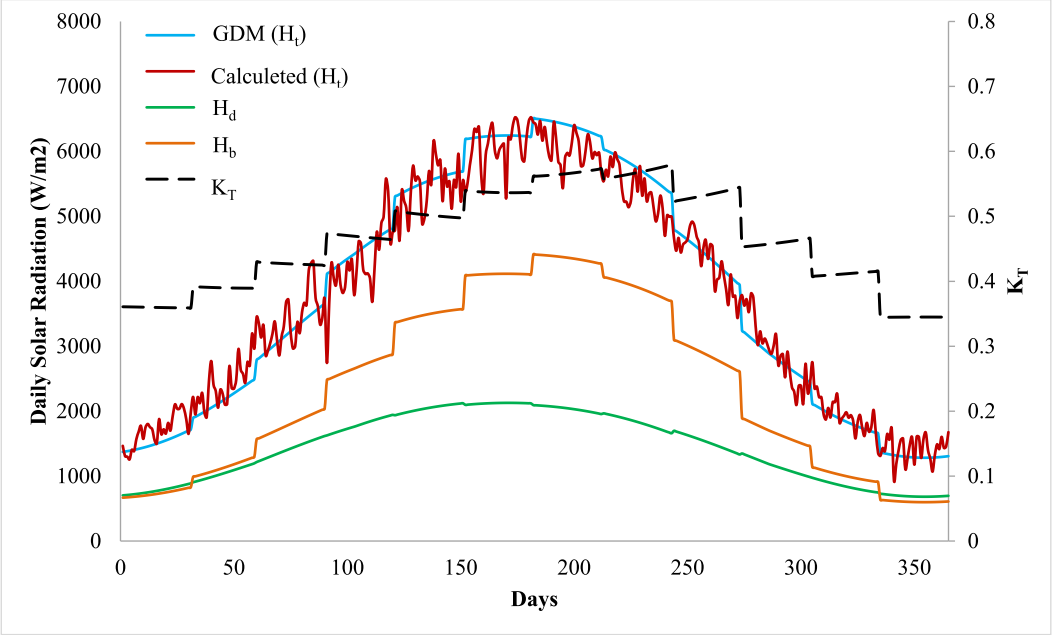

Fig. 3. Daily total solar radiation, direct solar radiation, diffuse solar radiation and K_T values.

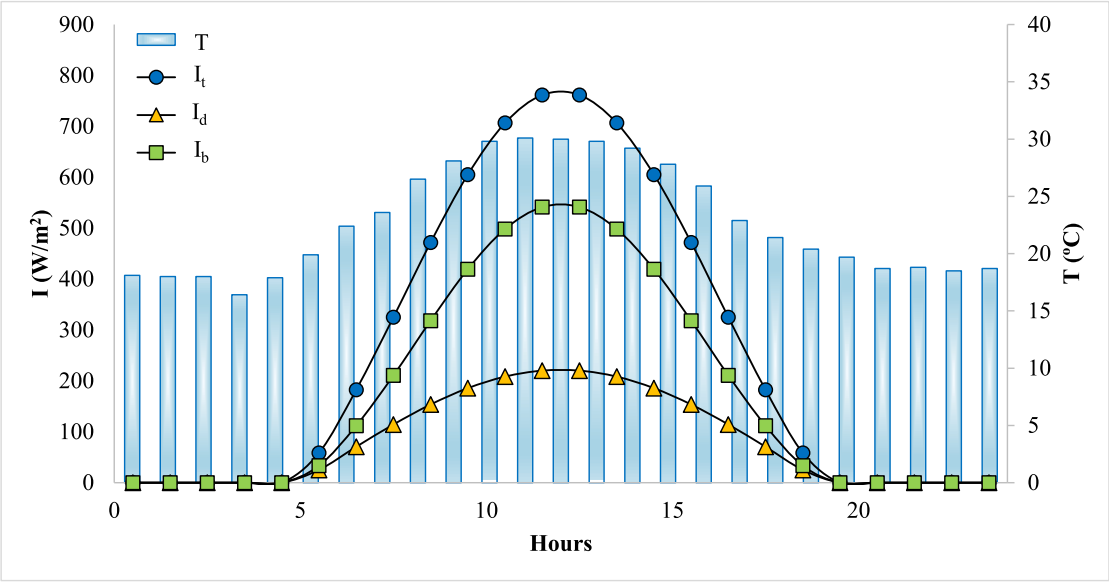

Fig. 4. Hourly solar radiation and temperature (T) values for the day maximum irradiation (July 1).

Although the mountainous and rugged terrain of Bilecik may pose challenges for solar power due to potential shading issues, there are still possibilities for solar energy generation. Considering the shading, transportation, and distance to networks, the available areas were determined for installing solar collectors. Detailed information about the designated solar power plant area is given in the previous study by the authors [9]. The proposed system comprises four key components: SF, TES, SRC, and ORC. The schematic diagram of the proposed system is illustrated in Fig. 1, providing a visual representation of how these components are interconnected and function together.

In SF, PTSCs are commonly used in areas with low solar radiation. In the designed system, some heat (at x mass ratio) provided from SF is used for power generation, while the remaining (at 1-x mass ratio) feeds the TES system. The energy transferred to the TES system in the heat exchanger (HE-I) is stored in the hot storage tank (*HST*) to be evaluated when solar energy is insufficient. The energy transferred to the power cycle from HE-II activated in the nonsolar time and HE-III activated in the solar time conditions generates high-pressure superheated steam in the working fluid (at point 3) in the SRC. The fluid in this state generates electricity by operating the Turbine-I. Since the SRC is suitable for operation at high temperatures, the fluid at point 4 still has a high energy potential. Waste heat is evaluated through the sub-cycle added to benefit from this energy. Two-stage power generation is provided by the waste heat transferred from HE-IV to the ORC. Since no cooling water source exists in the selected region, air cooling in the condenser has been considered. The proposed system uses a shell-and-tube heat exchanger for liquid–vapor heat transfer and a plate type heat exchanger for liquid–gas heat transfer. Under these circumstances, the two-stage solar power cycle system was evaluated from the energy, exergy, economic, and environmental points of view. The calculation steps are given in

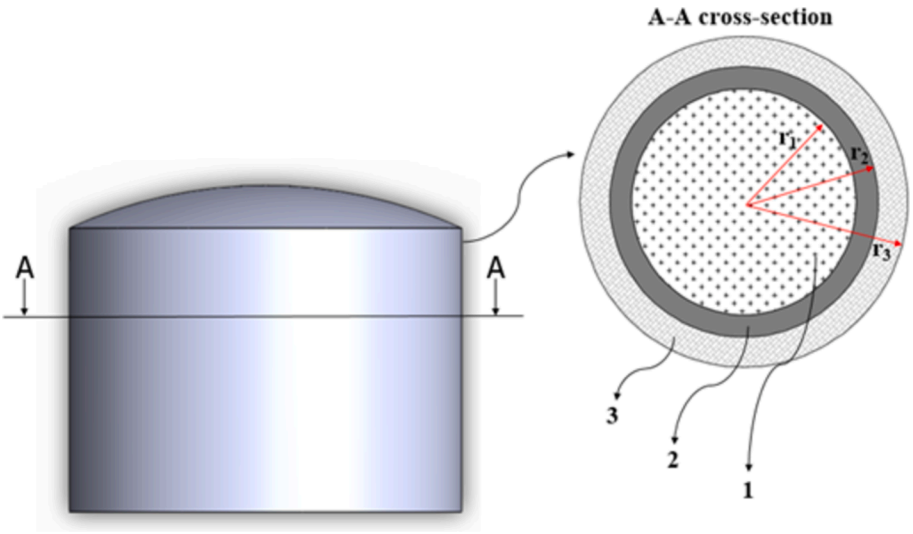

Fig. 5. Model of TES tank.

Table 2
The technical properties of TES.

Property	Value
D_t(m)	30
H(m)	9.2
V(m^3)	6616.31
m(tons)	10162.65

Table 3
Properties of TES system [38,39].

Component	Explanation	Material	Radius (m)	Thickness (mm)	k(W/m °C)
1	Storage material	Molten salt	–	–	0.55
2	Stainless steel	AlS/316	15	30	13.4
3	Insulation	Glass wool	–	100	0.038

Fig. 2.

Since the most critical challenge of a solar power plant is radiation fluctuations and how to provide the energy needed to produce steam during the night or on cloudy days, a dynamic analysis was conducted for a complete year to create a realistic model in Excel through the analytical calculations given as follows.

2.1. Design of the solar Field

PTSC have a reflective surface that redirects sunlight towards a central receiver pipe, where a fluid is heated, turning it into a heat source. For the optimal utilization of solar rays, the PTSCs are positioned in a horizontal North-South (N-S) axis and equipped with a solar tracking system that allows movement in the East-West (E-W) direction. As determined in previous research, the distance between PTSCs is set at 5.1 m to minimize shading effects [9]. Table 1 presents the detailed technical specifications of the PTSCs. These specifications provide essential information about the physical characteristics and performance parameters of the PTSCs used in the system. It includes necessary details such as dimensions, material properties, tracking system capabilities, and other relevant features for understanding the design and operation of the PTSCs. As for the heat transfer fluid used in the solar field, a thermic oil called Therminol VP-I has been selected since it demonstrates favorable heat transfer properties and effective temperature control [30]. This study assumes that the temperature at the PTCS outlet for Therminol VP-I is kept at 400 °C.

Table 4
Properties of fluids used in system design [45,46].

Properties	Therminol VP-I	Molten salt	R718	R152a	R600a
$T_{boiling}$(°C)	257.0	–	100	−24	−11.7
$T_{melting}$(°C)	–	99	–	–	–
T_{cr}(°C)	430	–	374.0	113.3	134.7
P_{cr}(MPa)	–	–	22.06	4.52	3.63
ρ(kg/m^3)	990.6	1920	795.2	812.3	508.7
c_p(kj/kgK)	2.305	1.66	2.16	2.01	2.67

It is essential to know about DNI to accurately analyze systems with solar tracking, such as PTSC. Unlike diffuse solar radiation, direct solar radiation cannot be directly calculated. It is determined by subtracting the diffuse solar radiation from the total solar radiation. Total solar radiation data can be obtained from meteorological stations or estimated using empirical equations. The daily total solar radiation values measured for Bilecik were obtained from the General Directorate of Meteorology (GDM) [32]. The daily total solar radiation values calculated using 20 different empirical equations were statistically compared with those obtained from the General Directorate of Meteorology. In this context, the Kilic and Ozturk model, presented in Equation (1), is the most statistically appropriate model [32,33]. The coefficient of determination (R^2), Mean Absolute Percentage Error (MAPE) and the root mean square error (RMSE) values for this model were determined to be 0.97, 0.08 and 1.21, respectively, indicating a high level of agreement between the calculated values and the actual measurements [32]. Accordingly, the daily total solar radiation incident on the horizontal plane (H_t) is given by:

$$\frac{H_t}{H_0} = a + b \bullet (S/S_0) \tag{1}$$

where H_0, S, and S_0 define daily extraterrestrial radiation, daily sunshine duration, and day length, respectively. Then, the Barbaro model [34] approved for the studied area [32] was used to calculate the daily diffuse solar radiation (H_d) incident to the horizontal plane:

$$\frac{H_d}{H_t} = 1.0492 - 1.13246 \bullet K_T \tag{2}$$

where K_T is the day's clearness index. Accordingly, daily direct solar radiation (H_b) can be determined by [34]:

Table 5
The technical properties of the used shell and tube type heat exchangers [47–49].

Shell and Tube Heat Exchangers Properties	Value
n_{pass}	1
L(m)	12
$D_{i,t}$(m)	0.016
$D_{o,t}$(m)	0.0508
l(m)	0.0015
θ(°)	30
e(m)	1.5
PR	1.25
D_s(m)	1
k(W/mK)	42.7 (Chromium alloy)

$$H_b = H_t - H_d \tag{3}$$

Total solar radiation values obtained from the GDM, calculated H_t, H_d and H_b and K_T are given in Fig. 3.

Hourly total solar radiation values (I_t) can be determined from H_t values using the relations developed by Collares-Pereira and Rabl [35,36]. Accordingly, the hourly total solar radiation (I_t) is given by:

$$I_t = H_t \frac{\pi}{24}(a + b \bullet cos\omega)\frac{cos\omega - cos\omega_s}{sin\omega_s - \frac{\pi\omega_s}{180}cos\omega_s} \tag{4}$$

The hourly diffuse solar radiation (I_d) value can be determined using the equation suggested by Liu and Jordan [36]:

$$I_d = H_d \frac{\pi}{24}\frac{\cos\omega - \cos\omega_s}{\sin\omega_s - \frac{\pi\omega_s}{180}\cos\omega_s} \tag{5}$$

Accordingly, the hourly beam (DNI) solar radiation (I_b) value can be determined as follows:

$$I_b = I_t - I_d \tag{6}$$

Solar radiation was calculated for each day and hour of the year. The proposed system's analysis was carried out hourly for a complete year. Accordingly, July was determined as the month with the highest solar potential. Hourly solar radiation and temperature values for July 1, which has the highest solar radiation value, are given in Fig. 4.

When Fig. 5 is examined, the highest I_b on 1 July was observed as 541 W/m^2 between 12:00 and 13:00. The useful heat energy ($\dot{Q}_u$) that can be obtained from a single collector is determined by Equation (12). This equation quantifies the amount of valuable or beneficial energy considering various factors and parameters [37]:

$$\dot{Q}_u = F_R \bullet A_r[S \bullet CR - \pi \bullet U_L \bullet (T_{11} - T_a)] \tag{7}$$

Here, F_R is the heat removal factor, S is the heat absorbed by the receiver,CR is the concentration ratio of the PTSC, $and U_L$ is the heat loss coefficient. T_{11} and T_a are the inlet temperature of heat transfer fluid and the ambient temperature, respectively. The thermal efficiency of the PTSC can be calculated by [1]:

$$\eta_{PTSC} = \frac{\dot{Q}_u}{I_b} \tag{8}$$

Table 6
The technical properties of the used plate type heat exchangers [47–49].

Plate Type Heat Exchangers Properties	Value
H(m)	0.6
W(m)	0.3
t(m)	0.0007
b(m)	0.003
k(W/mK)	13.5 (Stainless Steel AISI 304)
N_P(plate number)	20
β (chevron angle)	30

Table 7
Energy and Exergy balances of system components.

Component.	Energy Analysis	Exergy Analysis
PTSC	$\dot{m}_{11}h_{11} + \dot{W}_{track} + \dot{Q}_u = \dot{m}_{12}h_{12}$	$\dot{m}_{11}\psi_{11} + \dot{W}_{track} + \dot{E}x_{solar} = \dot{m}_{12}\psi_{12} + \dot{E}x_{d,PTSC}$
HST	$\dot{m}_{15}h_{15} + \dot{Q}_{l,HST} = \dot{m}_{14}h_{14}$	$\dot{m}_{14}\psi_{14} - \left(1 - \frac{T_0}{T_{14}}\right) \bullet \dot{Q}_{l,HST} - \dot{m}_{15}\psi_{15} = \dot{E}x_{d,HST}$
CST	$\dot{m}_{18}h_{18} + \dot{Q}_{l,CST} = \dot{m}_{17}h_{17} + \dot{W}_{p,v}$	$\dot{m}_{17}\psi_{17} - \dot{m}_{18}\psi_{18} - \left(1 - \frac{T_0}{T_{17}}\right) \bullet \dot{Q}_{l,CST} + \dot{W}_{p,v} = \dot{E}x_{d,CST}$
HE-I	$\dot{m}_{12}h_{12} + \dot{m}_{18}h_{18} = \dot{m}_{13}h_{13} + \dot{m}_{14}h_{14}$	$\dot{m}_{12}\psi_{12} + \dot{m}_{18}\psi_{18} = \dot{m}_{13}\psi_{13} + \dot{m}_{14}\psi_{14} + \left(1 - \frac{T_0}{T_{12}}\right) \bullet \dot{Q}_{HE-I} + \dot{E}x_{d,HE-I}$
HE-II	$\dot{m}_{16}h_{16} + \dot{m}_{2'}h_{2'} = \dot{m}_{17}h_{17} + \dot{m}_{3'}h_{3'}$	$\dot{m}_{16}\psi_{16} + \dot{m}_{2'}\psi_{2'} = \dot{m}_{17}\psi_{17} + \dot{m}_{3'}\psi_{3'} + \left(1 - \frac{T_0}{T_{16}}\right) \bullet \dot{Q}_{HE-II} + \dot{E}x_{d,HE-II}$
HE-III	$\dot{m}_{12'}h_{12'} + \dot{m}_2h_2 = \dot{m}_{13'}h_{13'} + \dot{m}_3h_3$	$\dot{m}_{12'}\psi_{12'} + \dot{m}_2\psi_2 = \dot{m}_{13'}\psi_{13'} + \dot{m}_3\psi_3 + \left(1 - \frac{T_0}{T_{12'}}\right) \bullet \dot{Q}_{HE-III} + \dot{E}x_{d,HE-III}$
Pump- I	$\dot{m}_1h_1 + \dot{W}_{P-I} = \dot{m}_2h_2$	$\dot{m}_1\psi_1 + \dot{W}_{P-I} = \dot{m}_2\psi_2 + \dot{E}x_{d,P-I}$
Pump- II	$\dot{m}_5h_5 + \dot{W}_{P-II} = \dot{m}_6h_6$	$\dot{m}_{15}\psi_5 + \dot{W}_{P-II} = \dot{m}_6\psi_{26} + \dot{E}x_{d,P-II}$
Pump- III	$\dot{m}_{13}h_{13} + \dot{W}_{P-III} = \dot{m}_{11}h_{11}$	$\dot{m}_{13}\psi_{13} + \dot{W}_{P-III} = \dot{m}_{11}\psi_{11} + \dot{E}x_{d,P-III}$
Pump- IV	$\dot{m}_{15}h_{15} + \dot{W}_{P-IV} = \dot{m}_{16}h_{16}$	$\dot{m}_{15}\psi_{15} + \dot{W}_{P-IV} = \dot{m}_{16}\psi_{16} + \dot{E}x_{d,P-IV}$
Pump- V	$\dot{m}_{17}h_{17} + \dot{W}_{P-V} = \dot{m}_{18}h_{18}$	$\dot{m}_{15}\psi_{15} + \dot{W}_{P-V} = \dot{m}_{16}\psi_{16} + \dot{E}x_{d,P-V}$
Turbine- I	$\dot{m}_3h_3 = \dot{m}_4h_4 + \dot{W}_{T-I}$	$\dot{m}_3\psi_3 = \dot{m}_4\psi_4 + \dot{W}_{T-I} + \dot{E}x_{d,T-I}$
Turbine- II	$\dot{m}_7h_7 = \dot{m}_8h_8 + \dot{W}_{T-II}$	$\dot{m}_7\psi_7 = \dot{m}_8\psi_8 + \dot{W}_{T-II} + \dot{E}x_{d,T-II}$
Condenser	$\dot{m}_8h_8 + \dot{m}_9h_9 = \dot{m}_5h_5 + \dot{m}_{10}h_{10}$	$\dot{m}_8h_8 + \dot{m}_9h_9 = \dot{m}_5h_5 + \dot{m}_{10}h_{10} + \left(1 - \frac{T_0}{T_8}\right) \bullet \dot{Q}_{con} + \dot{E}x_{d,con}$

The detailed information about the solar irradiation analysis is given in Appendix A.

2.2. Design of thermal energy storage system

The thermal energy storage (TES) system comprises a hot storage tank *HST* and a cold storage tank (*CST*). The purpose of this system is to store the heat accumulated during the day so that it can be utilized during the night when sunlight is unavailable or on cloudy days when solar energy is insufficient. The liquid discharged from the *HST* is transferred to the *CST*, completing the storage cycle. The technical properties of the storage tanks are given in Table 2.

Insulation is applied to minimize heat transfer from the storage tanks to the surrounding environment. The selection of insulation materials is crucial since materials with higher heat transfer coefficients facilitate more excellent heat transfer. Conversely, materials with lower heat transfer coefficients are employed when reducing heat transfer is desired. The chosen storage material for the TES system is a molten salt mixture consisting of 17.50 % $LiNO_3$, 14.18 % $NaNO_3$, 50.53 % KNO_3, and 17.78 % $NaNO_2$ by weight. This specific mixture possesses desirable properties for TES applications, including a lower freezing point (99 °C), higher heat capacity (1.66 kJ/kgK), higher upper-temperature limit

Table 8
The basis of the emissions and the annual amount released into the environment [56].

Fuel type	Emission* CO_2	NO_2	SO_2
Lignite	0.47848	0.00782	0.00077

*per kg-fuel.

Table 9
The comparison and weighting matrix.

		Input	Output
IS	**CM**	I_b 1 5 5 5 5 5 C_{inv} 1 1 4 5 4 5 P_2 0.20 0.25 1 3 1 3 T_3 0.20 0.20 0.33 1 0.33 1 P_6 0.20 0.25 1 3 1 3 T_7 0.20 0.20 0.33 1 0.33 1	SI 1 0.33 0.50 1 0.33 W_{net} 3 1 0.50 1 0.50 η 2 2 1 0.50 0.33 ε 1 1 2 1 0.33 NPV 3 2 3 3 1
	WM	I_b 0.3524 C_{inv} 0.3239 P_2 0.1104 T_3 0.0514 P_6 0.1104 T_7 0.0514	SI 0.1022 W_{net} 0.1766 η 0.1738 ε 0.1662 NPV 0.3812
ES	**CM**	I_b 1 3 3 3 3 3 C_{inv} 0.33 1 0.5 0.5 0.5 0.5 P_2 0.33 2 1 3 1 3 T_3 0.33 2 0.33 1 0.33 1 P_6 0.33 2 1 3 1 3 T_7 0.33 2 0.33 1 0.33 1	SI 1 0.33 0.33 0.33 1 W_{net} 3 1 1 0.5 2 η 3 1 1 0.5 2 ε 3 2 2 1 1 NPV 1 0.5 0.5 1 1
	WM	I_b 0.3533 C_{inv} 0.0762 P_2 0.1896 T_3 0.0956 P_6 0.1896 T_7 0.0956	SI 0.0943 W_{net} 0.2244 η 0.2244 ε 0.3086 NPV 0.1481
CS	**CM**	I_b 1 1 1 1 1 1 C_{inv} 1 1 2 2 2 2 P_2 1 0.5 1 1 1 1 T_3 1 0.5 1 1 1 1 P_6 1 0.5 1 1 1 1 T_7 1 0.5 1 1 1 1	SI 1 0.5 1 1 2 W_{net} 2 1 1 1 0.50 η 1 1 1 1 2 ε 1 1 1 1 2 NPV 0.5 2 0.5 0.5 1
	WM	I_b 0.1647 C_{inv} 0.2599 P_2 0.1438 T_3 0.1438 P_6 0.1438 T_7 0.1438	SI 0.1968 W_{net} 0.2113 η 0.2149 ε 0.2149 NPV 0.1620

Table 10
The identification for the model enumerating.

Model indicator	$I_{b,m}$ (W/m^2)	P_3 (kPa)	T_3 (^{o}C)	P_7 (kPa)		T_7 (^{o}C)	
				R152a	R600a	R152a	R600a
1	150	650	240	1400	900	60	65
2	250	1000	270	1600	1000	65	70
3	350	1600	300	1800	1100	70	75
4	450	2000	330	–	–	75	–
5	541	3000	350	–	–	–	–
6	–	–	360	–	–	–	–
7	–	–	370	–	–	–	–
8	–	–	380	–	–	–	–

(425 °C), enhanced long-term thermal stability (total weight loss of 7.6 %), reduced corrosion behavior (15.75 μm/year), lower cost, and higher thermal conductivity (0.55 W/mK) [38]. The selected molten salt is more available than commonly used molten solar salt consisting of 60 % $NaNO_3$ and 40 % KNO_3 by weight since it is available for the higher temperatures of high-radiation areas (over 220 °C of melting point) [4]. From the freezing issues of the low-solar radiation zones, the selected molten salt has a lower melting point in comparison to other available molten salts such as $LiNO_3$-$NaNO_3$-KNO_3 (117.4 °C) and $LiNO_3$-$NaNO_3$-KNO_3-MgKN (101.2 °C) [38]. Fig. 5 illustrates the model of the storage tanks, showcasing their design and structure. Furthermore, Table 3 details the specific properties of the TES model.

The TES system is driven by three operating modes: charge, storage, and discharge. During the charging period, the heat obtained from the sun is stored in the *HST*. Although the molten salt has a maximum operating temperature of 390 °C, it is adjusted to 386 °C [40,41], considering the heat losses from the storage tank to the environment. The heat stored during insolation is discharged for use at night or on cloudy days. During discharge mode, the heat can be transmitted from the TES to the PB. TES consists of charging, storage, and discharging processes in hot and cold tanks. For the charging stage, the inlet heat of *HST* can be defined by [42]:

$$\dot{Q}_{HST} = \dot{Q}_{14} - \dot{Q}_{l,HST} \tag{9}$$

Here, $\dot{Q}_{l,HST}$ refers to the heat lost from the storage tank during the charging period, and it is calculated by [42,43]:

$$\dot{Q}_{l,HST} = (UA)_{HST} \bullet (T_{HST} - T_a) \tag{10}$$

where U and A are the overall heat transfer coefficient and heat transfer surface area of the storage tank, respectively. The $(UA)_{HST}$ is calculated by [9,44]:

$$(UA)_{HST} = \frac{1}{R_{top}} \tag{11}$$

Here, R_{top} is the total thermal resistance of the tank walls. The detailed analysis is given in Appendix B.

2.3. Design of two-stage power block

The power block (PB) of the system consists of a two-stage cycle, which aims to achieve higher power output and increased efficiency compared to single-stage systems. Unlike single-stage systems that release waste heat from the condenser into the environment, the two-stage cycle utilizes this waste heat of the steam Rankine cycle (SRC) to generate additional power through an organic Rankine cycle (ORC). The R718 (water) steam cycle was determined to be the most suitable fluid for the single-stage cycle to achieve optimal performance and maximum

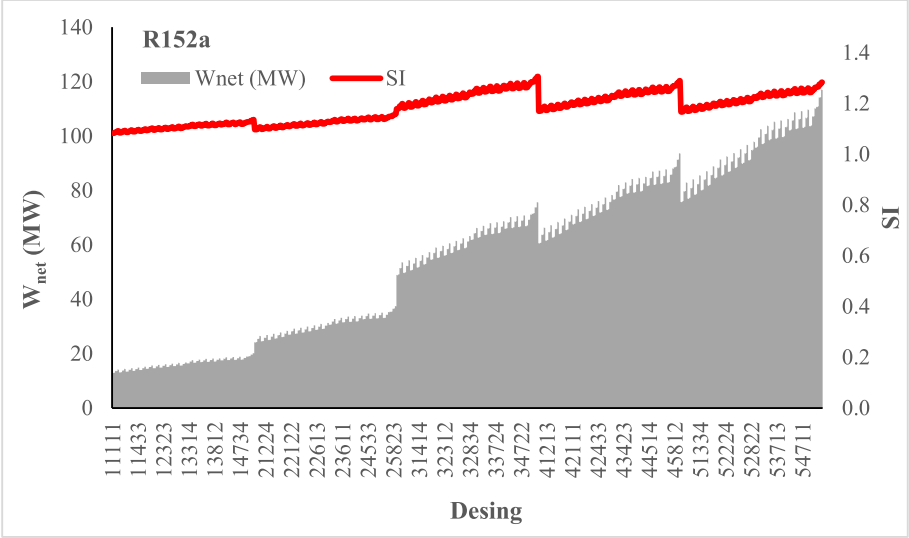

Fig. 6. W_{net} values of the formed designs for R152a.

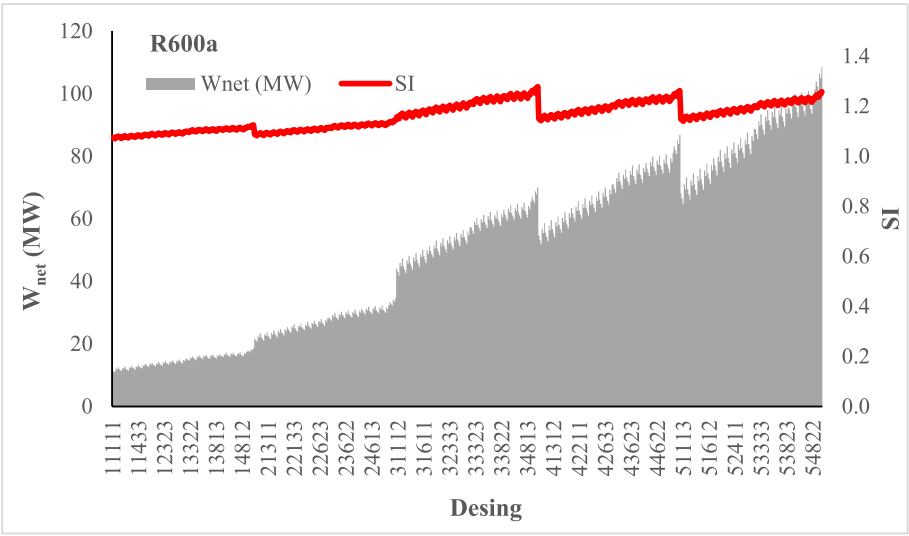

Fig. 7. W_{net} values of the formed designs for R600a.

efficiency in the authors' previous study [9]. Additionally, in the added organic Rankine cycle (ORC), which operates at lower temperatures, refrigerants R152a and R600a were selected since they are well-suited for harnessing waste heat with lower ozone depletion and global warming potentials. The properties of these fluids are detailed in Table 4. In calculations, turbine and pump efficiencies are included as 85 % and 80 % respectively [9].

The assumptions made in heat exchanger modeling include steady-state conditions, negligible heat losses from the surface, neglecting changes in kinetic and potential energies, and ignoring pressure drop in the tube side. These assumptions simplify the analysis and calculations, enabling a more focused evaluation of the heat transfer process within the heat exchanger. This study utilizes two different types of heat exchangers: a shell and tube heat exchanger and a plate type heat exchanger. The heat exchanger area (A_{HE}) can be expressed by [47,48]:

$$A_{HE} = \frac{\dot{Q}_{HE}}{U \bullet \Delta T_{LMTD}} \tag{12}$$

where U is the total heat transfer coefficient. ΔT_{LMTD} is defined logarithmic mean temperature. A shell and tube heat exchanger is a type of heat transfer device consisting of a cylindrical body and parallel pipes positioned within this body [49]. The shell and tube heat exchanger in this study served as the condenser. This heat exchanger design allows for effective heat exchange between the two fluids, optimizing the cooling process of the organic fluid within the system. The U is a calculated value that quantifies heat transfer efficiency in a shell and tube heat exchanger. The resulting coefficient provides valuable insights into the heat exchanger's performance and heat transfer effectiveness between the fluids. The U is calculated by [49]:

$$U = \frac{D_{o,t}}{D_{i,t}}\frac{1}{h_i} + \frac{\ln(D_{o,t}/D_{i,t})}{2\pi kL} + \frac{1}{h_o} + \frac{D_{o,t}}{D_{i,t}}R''_{fi} + R''_{fo} \tag{13}$$

The detailed analysis for the shell and tube heat exchanger is given in Appendix C. Table 5 provides the used shell and tube type heat exchangers' technical specification.

Plate type heat exchangers consist of an assembled series of plates. The hot and cold fluids flow through separate channels formed by the narrow gaps (b) between the plates, allowing for efficient heat transfer. This design ensures that the fluids do not mix during the process, enabling effective heat exchange. This study selects HE-I, HE-II, HE-III,

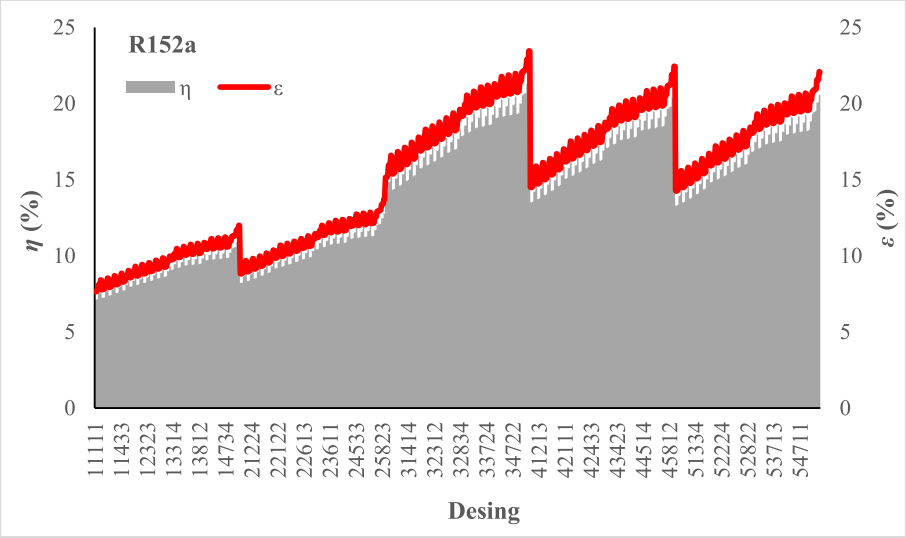

Fig. 8. η and ε variation of the formed designs for R152a.

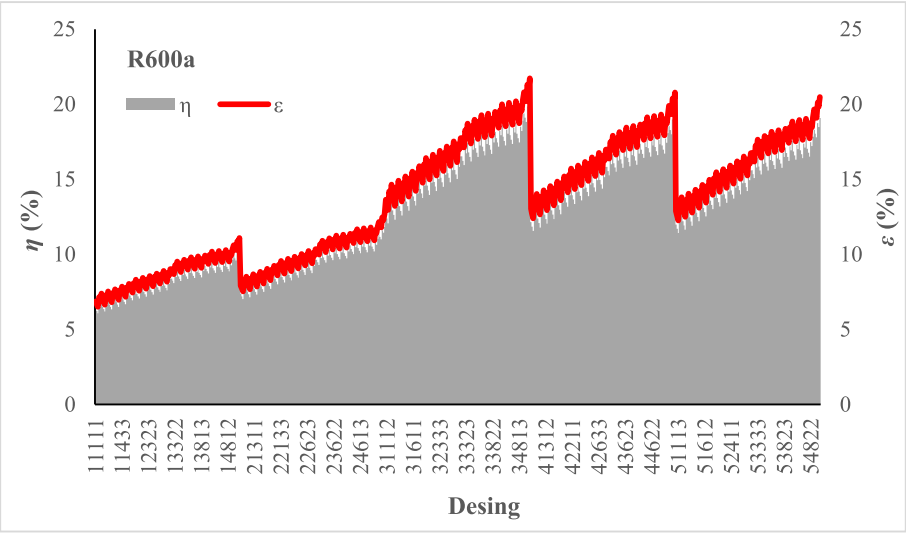

Fig. 9. η and ε variation of the formed designs for 600a.

and HE-IV as the plate type heat exchangers. The U for the plate type heat exchanger is calculated [50]:

$$U = \frac{1}{\frac{1}{h_i} + \frac{t}{k} + \frac{1}{h_o}} \tag{14}$$

where t, k, and h are defined as plate thickness, thermal conductivity of material, and heat transfer coefficient (inlet and outlet), respectively. The detailed analysis of plate type heat exchanger is given in Appendix D. Table 6 provides the used plate type heat exchangers' technical specifications, including dimensions, material composition, and other relevant parameters.

3. Thermodynamic evaluation

Table 7 provides the energy and exergy balance equations for all the components within the system being analyzed. These equations describe the energy and exergy fluxes associated with each element and help to understand the energy and exergy transformations occurring within the system. Here, the terms h and ψ define the enthalpy and exergy flux, respectively. The specific exergy of a flow can be calculated as [39]:

$$\psi = (h - h_0) - T_0(s - s_0) \tag{15}$$

where h and s are defined as enthalpy and entropy, respectively. The subscript "0" identifies the reference state conditions taken as 25 °C and 1 atm for this study.

Energy (η) and exergy (ε) efficiency of the system are given as [39]:

$$\eta = \frac{\dot{W}_{net}}{I_{b,m}} \tag{16}$$

$$\varepsilon = \frac{\dot{W}_{net}}{\dot{E}x_{solar}} \tag{17}$$

Here, $\dot{W}_{net}$ is the net power output in the system and is expressed by:

$$\dot{W}_{net} = \dot{W}_{T-I} + \dot{W}_{T-II} - \dot{W}_{P-I} - \dot{W}_{P-II} - \dot{W}_{P-III} - \dot{W}_{P-IV} - \dot{W}_{P-V} - \dot{W}_{track} - \dot{W}_{fan} \tag{18}$$

$\dot{E}x_{solar}$ represents the exergy of solar radiation and is calculated [1]:

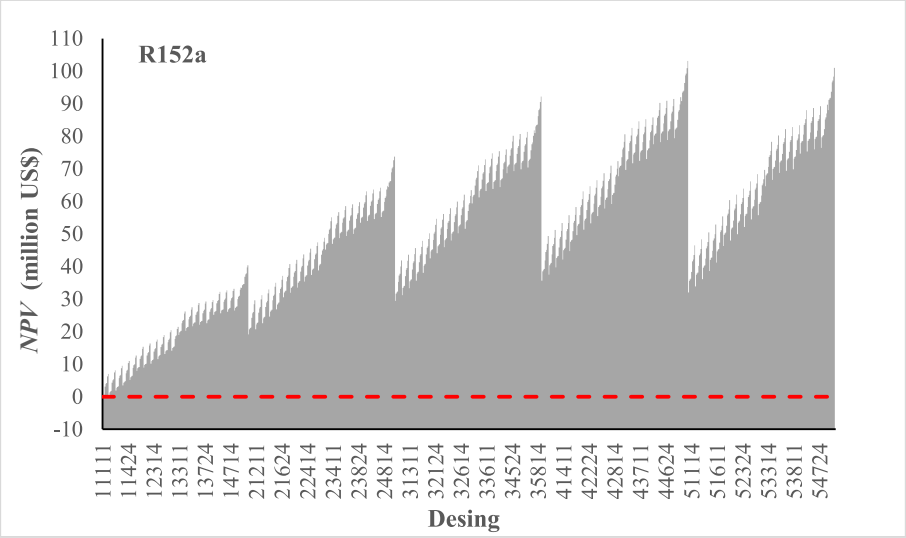

Fig. 10. *NPV* variation of the formed designs for 152a.

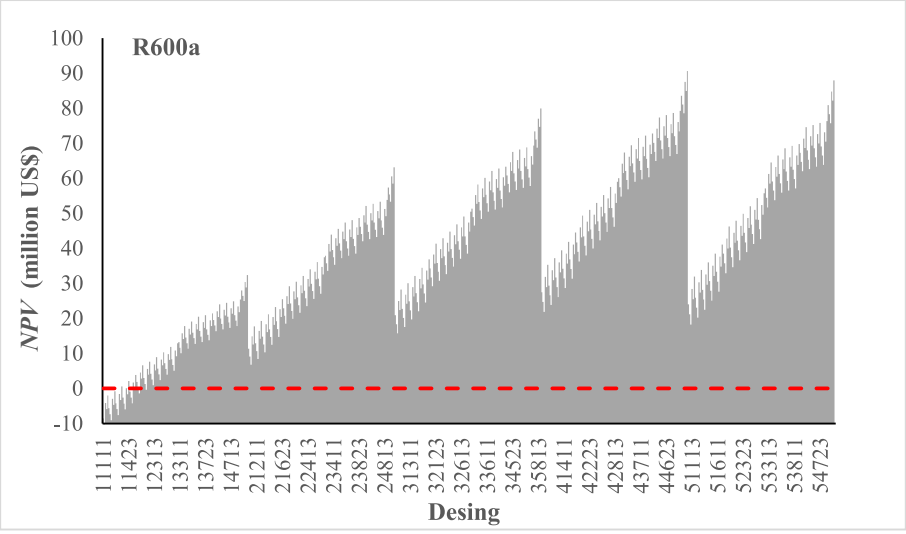

Fig. 11. *NPV* variation of the formed designs for 600a.

$$\dot{E}x_{solar} = I_d\left[1+\frac{1}{3}\left(\frac{T_0}{T_{sun}}\right)^4-\frac{4}{3}\left(\frac{T_0}{T_{sun}}\right)\right] \tag{19}$$

Here, T_{sun} is the sun's temperature, taken as 5800 K [1]. The sustainability index (*SI*) is one of the most used exergy-based sustainability indices. The *SI* is given as [51]:

$$SI = \frac{1}{1-\varepsilon} \tag{20}$$

4. Economic evaluation

NPV method serves as a financial instrument employed for assessing the economic viability of an investment or project. This methodology evaluates the profitability of an investment by juxtaposing the present value of anticipated cash inflows with the initial investment cost. By computing this value, researchers can gauge the financial feasibility of investing in the system. A positive value signifies that the anticipated cash inflows from the investment surpass the initial investment cost, suggesting the project's suitability for investment. Conversely, a negative value suggests that the expected cash inflows are insufficient to cover the initial investment, indicating that the project may not be financially viable. The *NPV* can be expressed as [52]:

$$NPV = \sum_{t=0}^{n}\frac{B_t}{(1+r)^t} \tag{21}$$

where n, B_t, and r are defined as the project's useful life, cash flow in t he year of t, and discount rate, respectively. The detailed analysis is given in Appendix E.

5. Environmental evaluation

Global energy demand is largely met by coal, which has led to several adverse environmental impacts, such as greenhouse gas emissions and acid rain. So, it is important to consider potential emissions when evaluating a system's environmental impact. In this study, environmental analysis is based on the principle of determining the amount of harmful gas emissions to the environment if coal were used instead of solar energy in the designed system.

The evaluation focuses on estimating the annual reduction in gas emissions throughout the lifespan of the designed system, which is set at

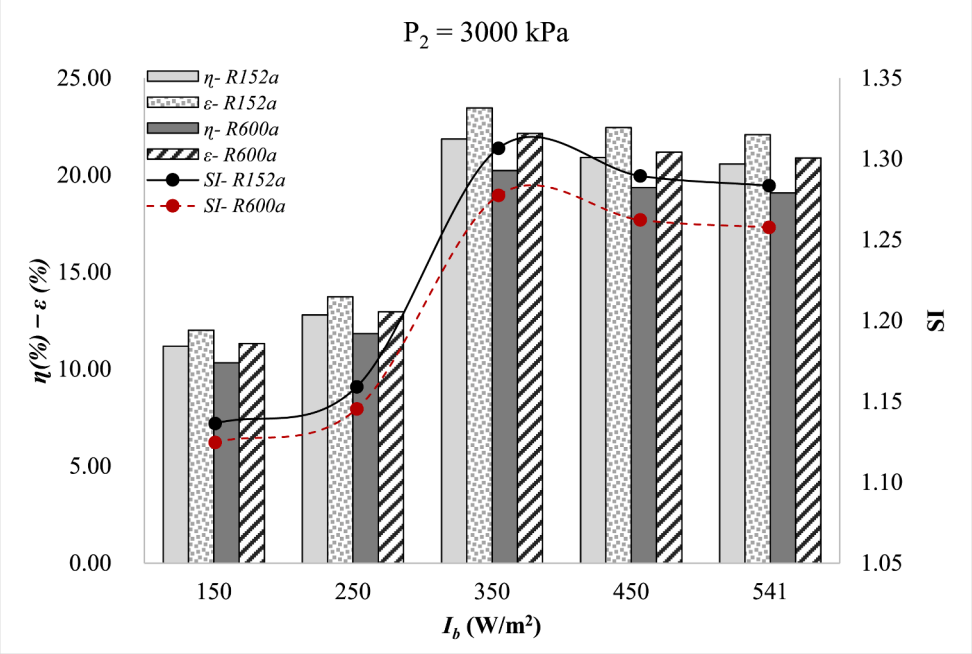

Fig. 12. Variation of η, ε, and SI values by DNI.

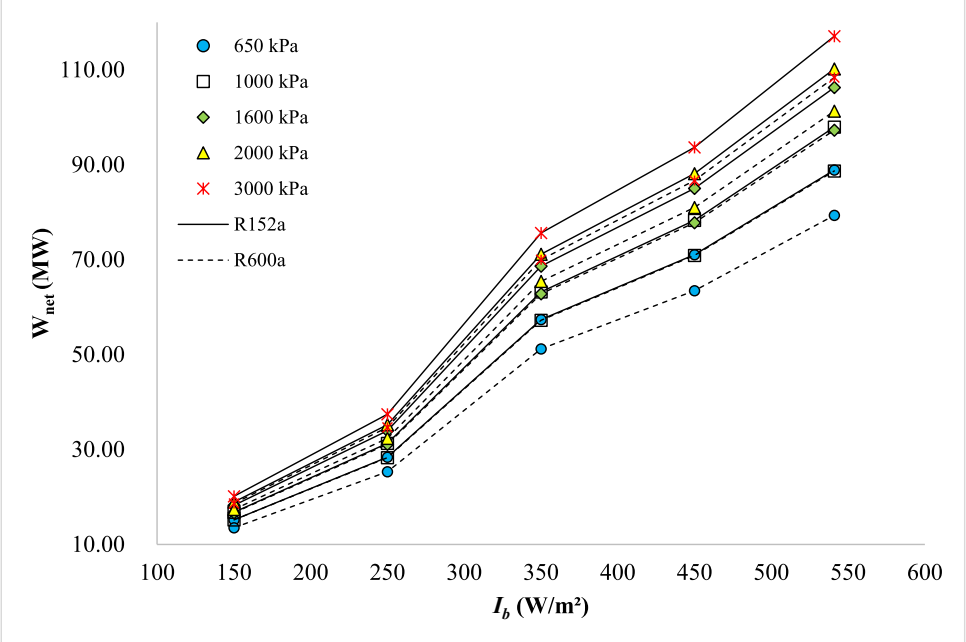

Fig. 13. Variation of W_{net} values by DNI.

20 years. The energy input (E_i) required to produce the same outcome is calculated by [53]:

$$E_i = \frac{\dot{W}_{net,annual}}{\eta_{plant}} \tag{22}$$

where η_{plant} is defined as the efficiency of coal power plants and is taken 27 % [54]. Therefore, the quantity of coal (M) necessary to produce the same energy input is calculated as [53]:

$$M = \frac{E_i}{NCV} \tag{23}$$

where NCV is the net calorific value of soma lignite coal and is taken as 5.57 kWh/kg [32,44,55]. Accordingly, the environmental parameters (γ_x) are calculated as [32]:

$$\gamma_x = M \bullet n \bullet x \tag{24}$$

where n and x are defined as the power plant's lifetime and the average amount of CO_2, NO_2, and SO_2 emitted in the environment. The basis of the emissions and the annual amount released into the atmosphere are given in Table 8.

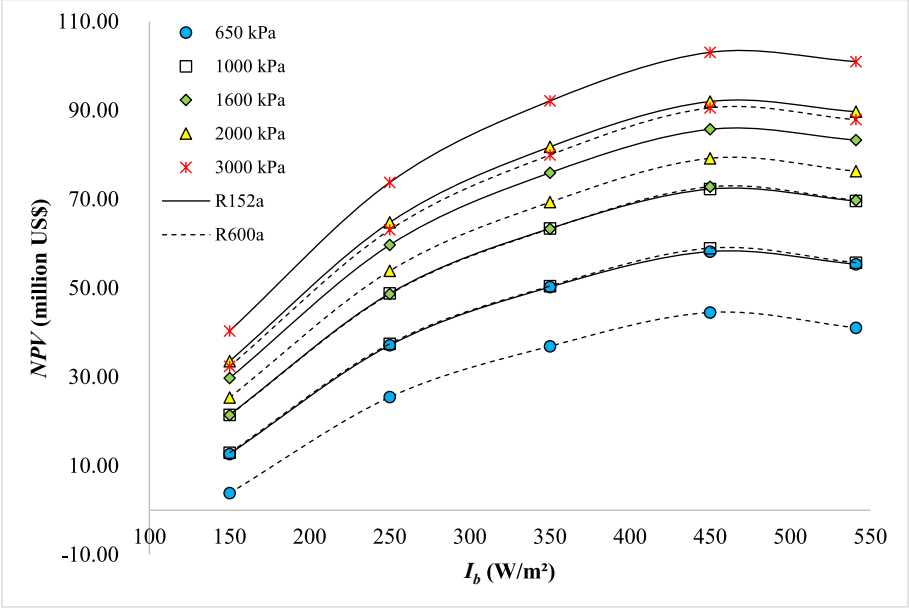

Fig. 14. Variation of NPV values by DNI.

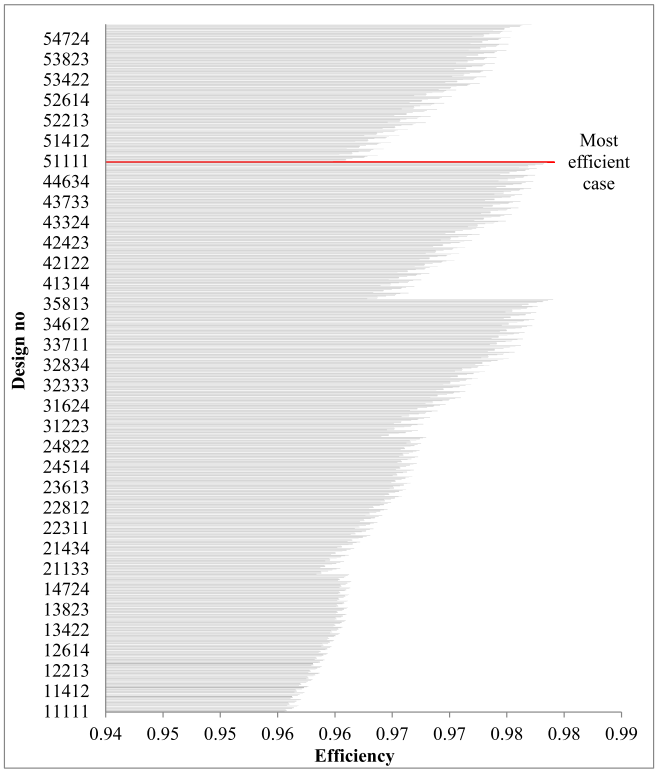

Fig. 15. Investor-based MCDM results for R152a.

6. Multi-Criteria Decision-Making analysis

Multi-criteria decision-making (MCDM) analysis was a successful tool for engineering optimizations [57–59]. Efficiency Analysis Technique with Output Satisficing (EATWOS) is a sufficient technique depending on the successful results for energy problems since it maximizes the output values for the minimal input values [60]. So, the efficiency of the i^{th} design with inlet parameters in a number of k is given by [28,60]:

$$E_i = \sum_{j=1}^{n} \frac{\left[op_j\right] \bullet \left[v_j\right]_{AHP}}{\left[ip_1 \quad \cdots \quad ip_k\right] \bullet \left[w_j\right]_{AHP}} \tag{25}$$

where j indicates the output parameter obtained by the thermodynamic analysis of the energy system. w_k and v_j are the weights of input and output parameters, respectively. In this study, the weights were determined by Analytical Hierarchic Process (AHP) considering three social aspects, including the investor sight, consumer sight and engineering

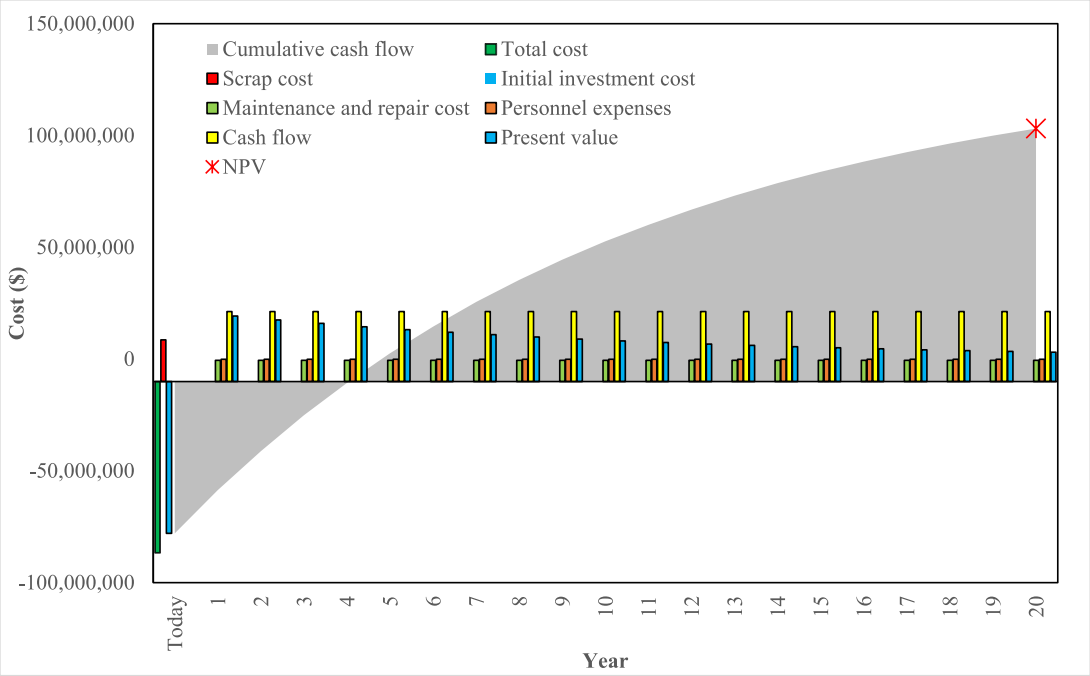

Fig. 16. Investor-based NPV analysis results for R152a.

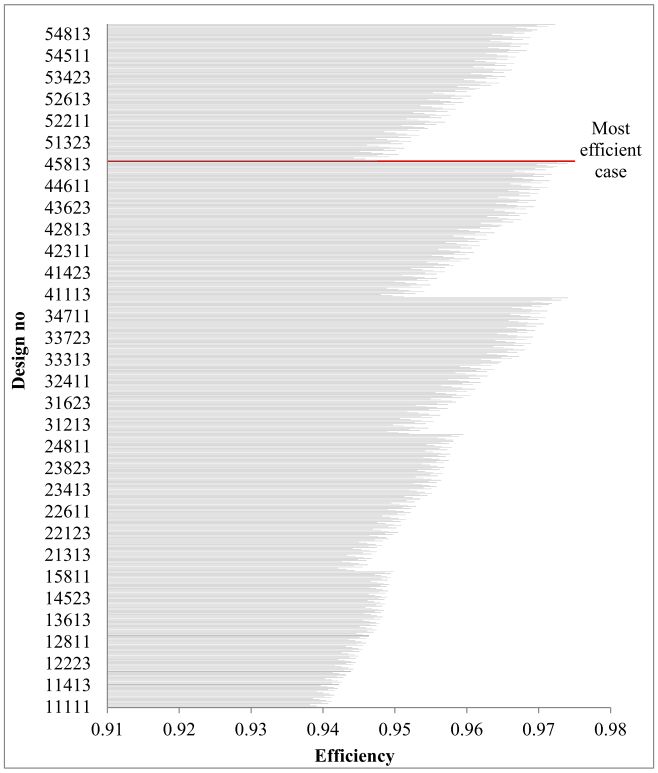

Fig. 17. Investor-based MCDM results for R600a.

(technical) sight since AHP is capable to view the expert and handled perspectives [28,61]. The detailed information about the hybrid analysis of AHP and EATEOS is given in Appendix F.

These weighting matrices are formed based on three social aspects, including investor sight (IS), engineering (ES) sight and consumer sight (CS). Power generation has different social aspects, including the investor, technical (engineering) and consumer sights. An investor aims to get more benefits with less investment cost, whereas an engineer aims for the highest generation with the highest efficiency. The cost issues are related to efficiency for an engineering approach since higher efficiency means less cost at the optimal point. However, a consumer deals with the power tariffs he must pay. Under these social aspects, the parameters affecting the design were determined to obtain decision units and a comparison matrix, considering the expert view [58,61,62]. In forming

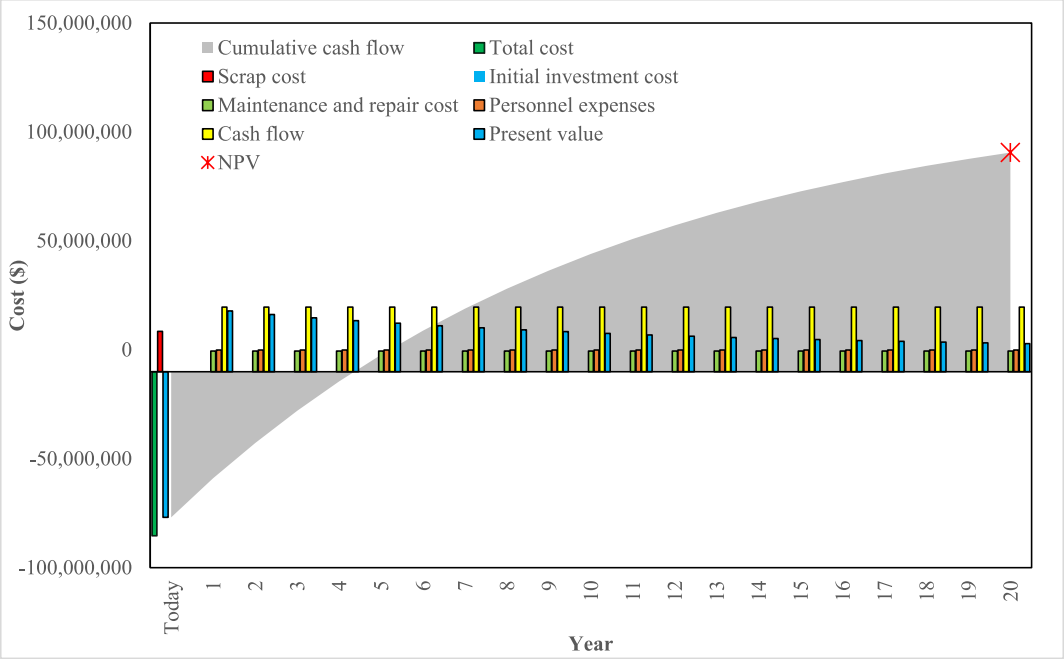

Fig. 18. Investor-based NPV analysis results for R600a.

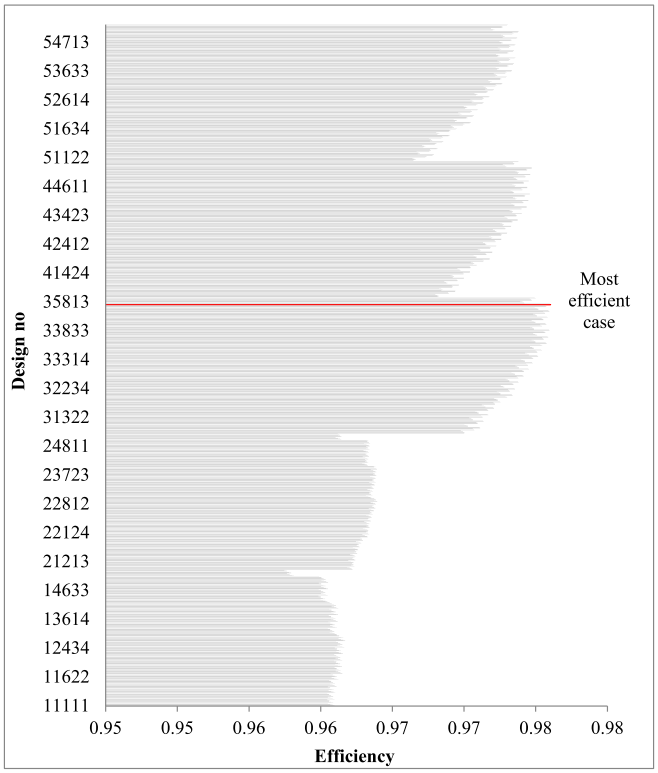

Fig. 19. Engineering-based MCDM results for R152a.

the comparison matrix (CM) matrix for the investor sight (IS), the beam (DNI) irradiation (I_b) and the investment costs (C_{inv}) are the most important input parameters, whereas the net present value (*NPV*), and generated net electricity (W_{net}) are the most crucial output parameters. From the engineering sight (ES), the technical parameters directly affecting the generation process, such as temperature (T) and pressure (P), are the most important input parameters, whereas the energy (η) and exergy efficiencies (ε), and W_{net} are the most crucial output parameters. From the consumer sight (CS), the economic parameters are the most critical input parameters since the consumers are just interested in how much they pay [62]. So, the most important input parameter is the C_{inv} since it directly affects the unit prices of the electricity generation. The most important output parameters for CS are determined as the W_{net} and NPV for the same reason. In the viewpoint of importance scale given in Table 10, the pair comparative evaluations were conducted between each determined decision unit. So, the CMs

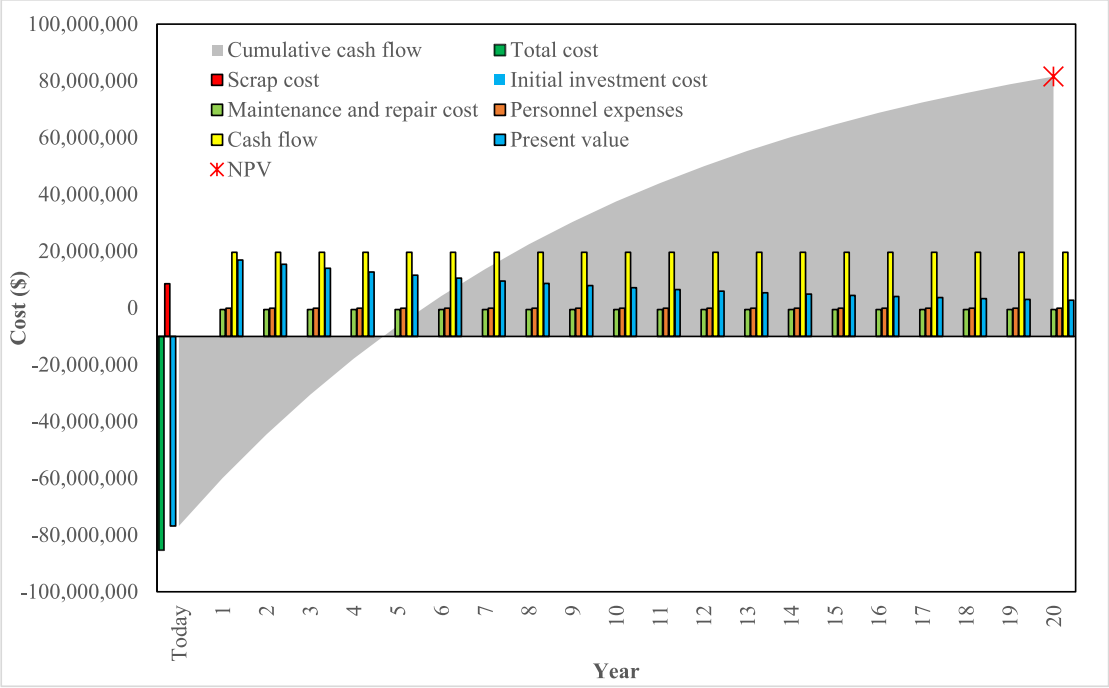

Fig. 20. Engineering-based NPV analysis results for R152a.

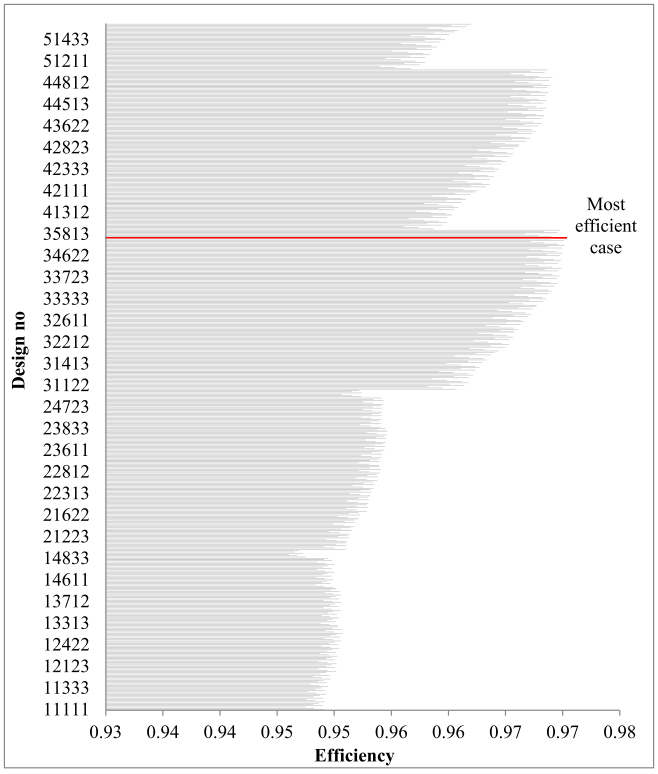

Fig. 21. Engineering-based MCDM results for R600a.

were formed, and WMs were determined. The accuracy and applicability of this process were verified for the values of CR less than 0.1. The CR values of input parameters were calculated as 0.0368, 0.0531, and 0.0878 for IS, ES, and CS, respectively. The CR values of output parameters were calculated as 0.0849, 0.0592, and 0.0894 for IS, ES, and CS, respectively. The obtained CMs and WMs are given in Table 9.

7. Results and Discussion

The designed system consists of SF, TES, SRC, and ORC. System performance was evaluated considering DNI values varying between 150–541 W/m^2. First and second law analyses of the system model designed using two different refrigerants (R152a, R600a) were made, and sustainability evaluation was made depending on the exergy. The

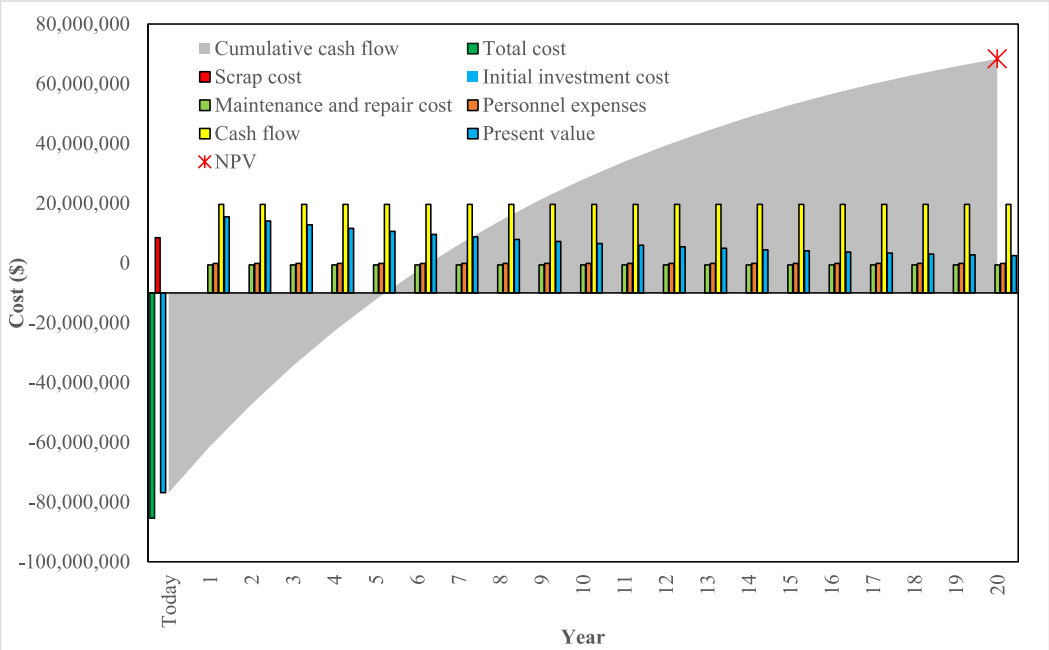

Fig. 22. Engineering-based NPV analysis results for R600a.

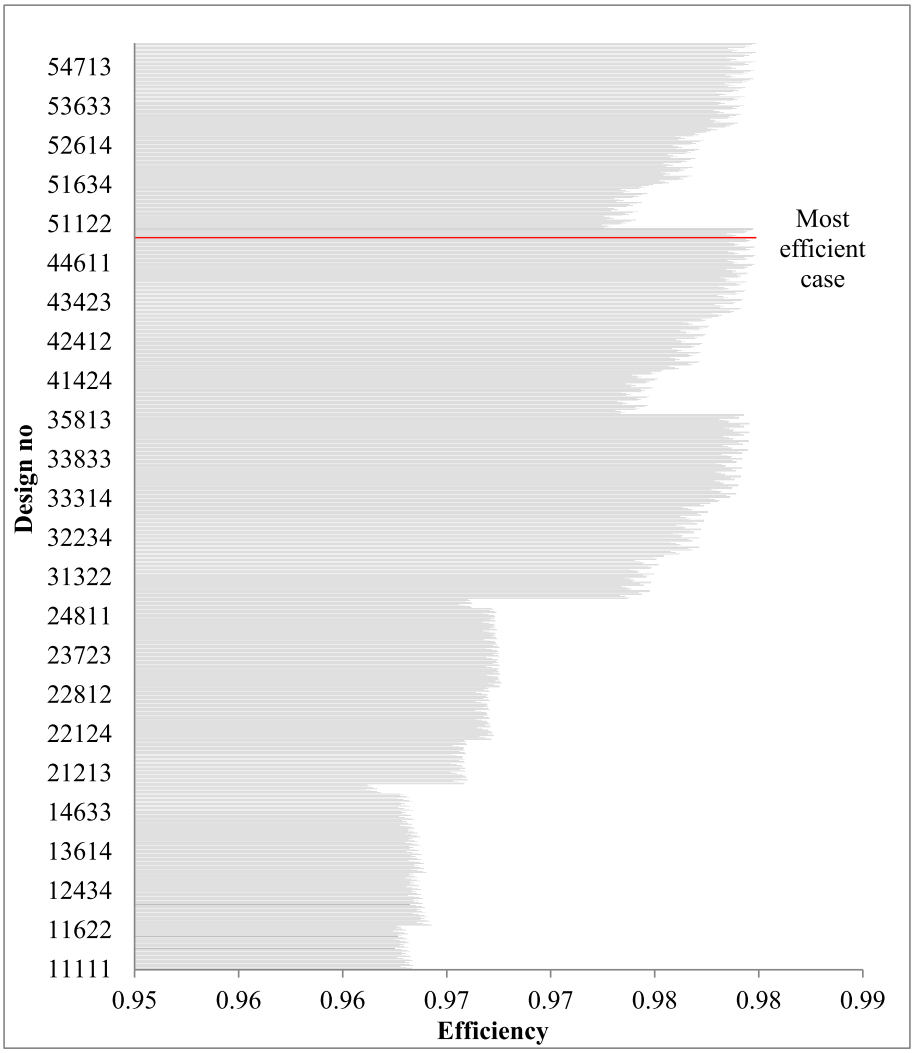

Fig. 23. Consumer-based MCDM results for R152a.

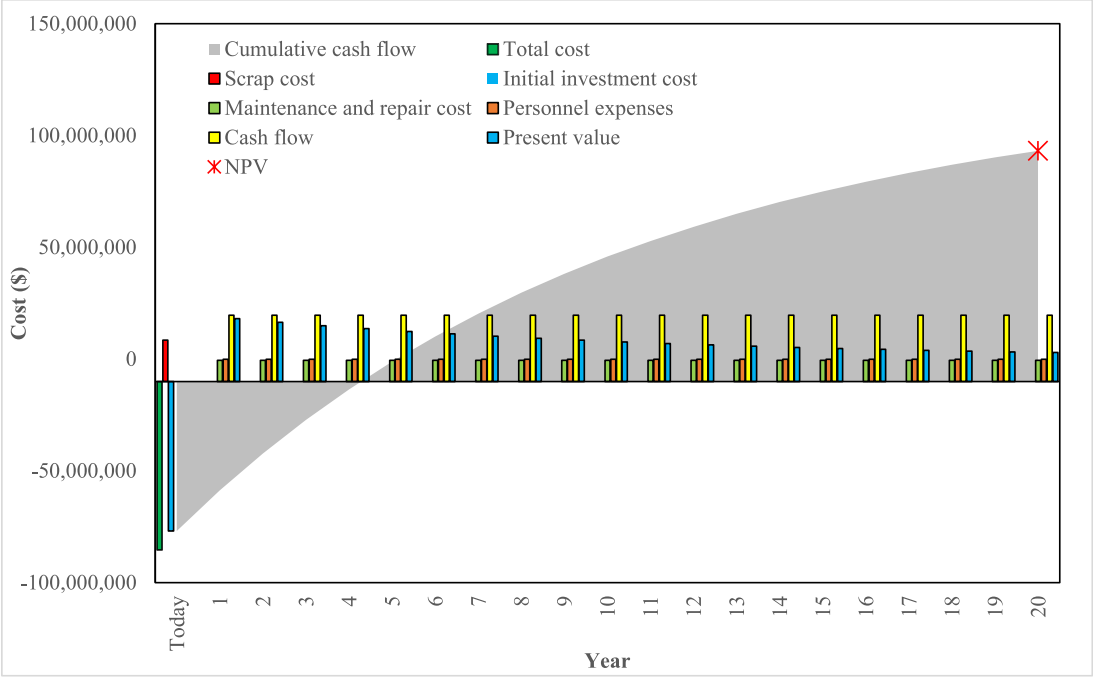

Fig. 24. Consumer-based MCDM results for R152a.

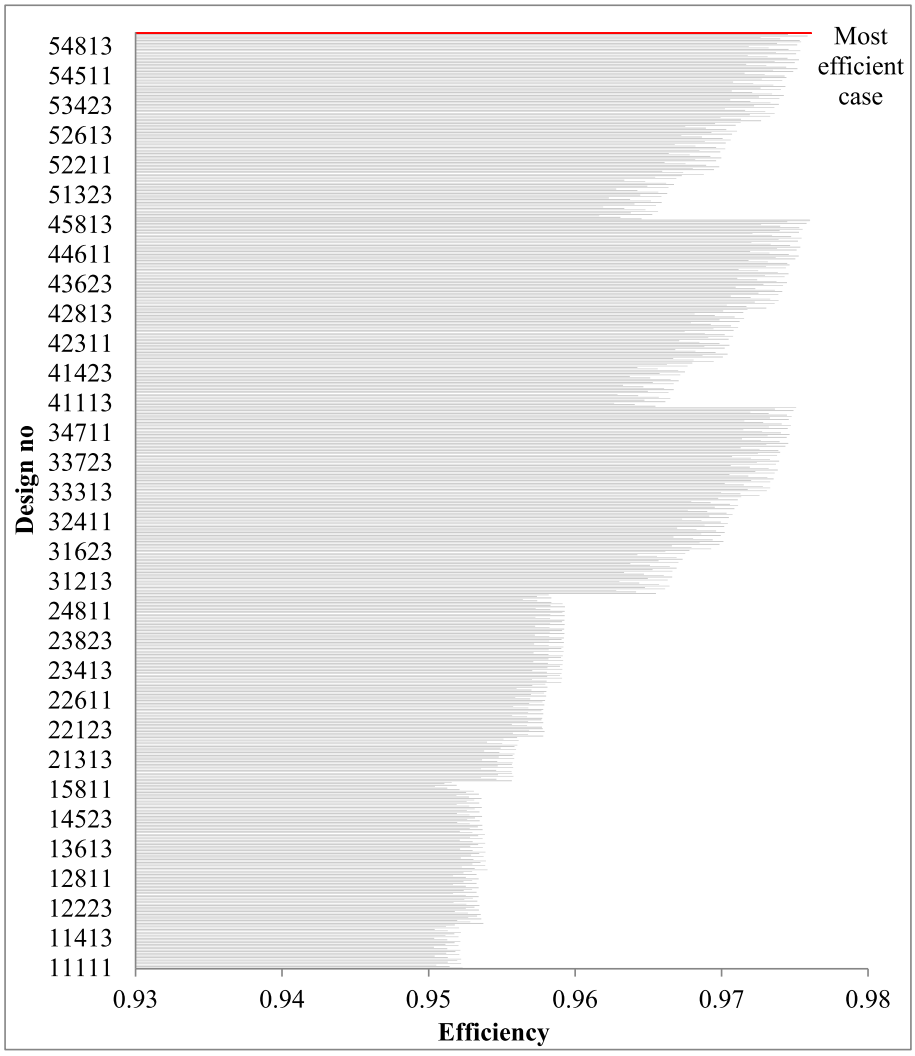

Fig. 25. Consumer-based MCDM results for R600a.

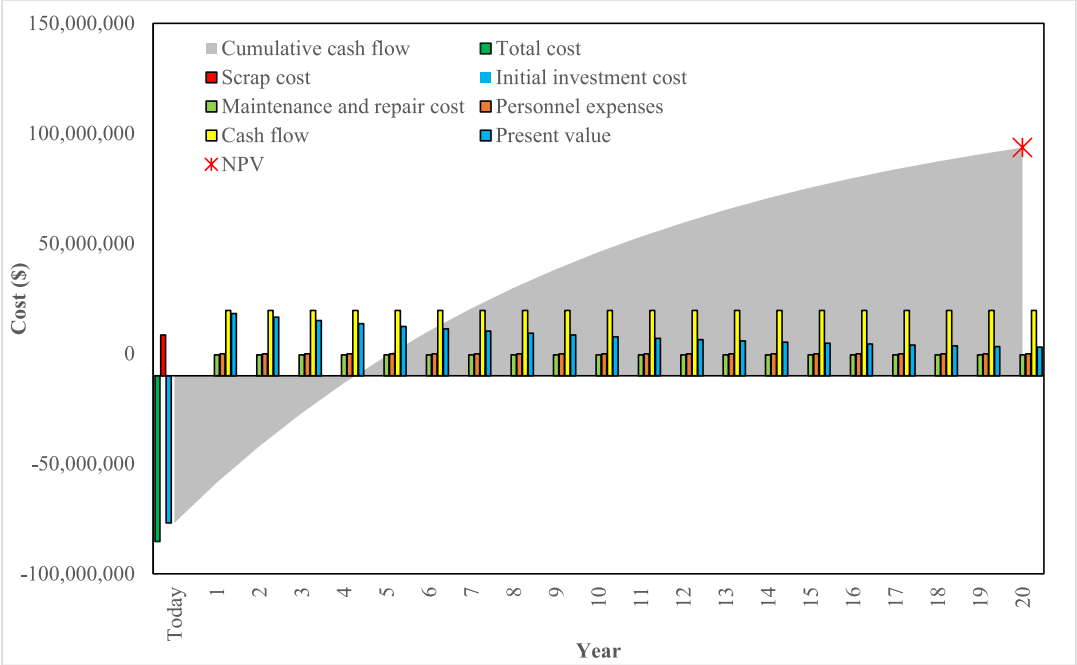

Fig. 26. Consumer-based MCDM results for R600a.

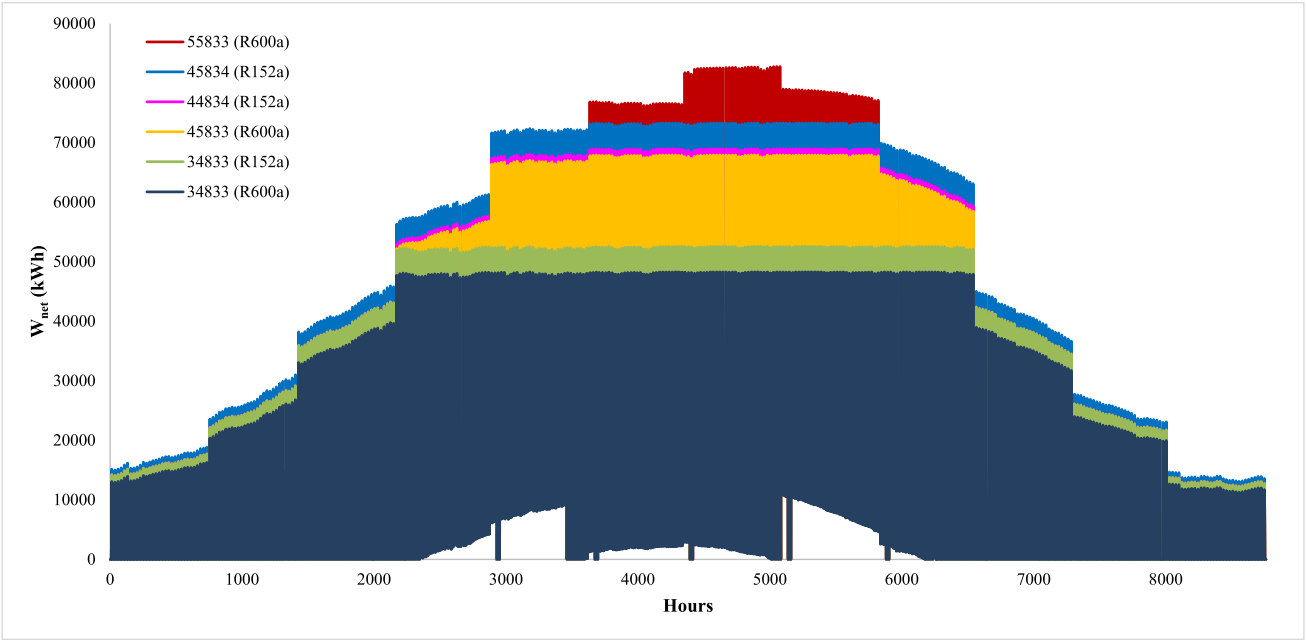

Fig. 27. Consumer-based MCDM results for R600a.

cost analysis of the system was made using the *NPV* method, and environmental analysis was carried out to determine the effects of the system on the environment. Additionally, the system was analyzed on an investor-based, engineering-based, and consumer-based basis using the multi-criteria decision-making method.

A dynamic model based on an hourly basis was conducted to determine the optimal operating conditions of the designed system. In this study, the following parameters are considered. The authors have considered the optimal values determined for SF and TES in their previous studies [9] as fixed parameters in this work. Accordingly, T_{11}, T_{12}, T_{14}, and T_{18} values are 120 °C, 400 °C, 390 °C, and 111 °C, respectively. These fixed temperature values were chosen to evaluate the performance and efficiency of the power plant under specific operating conditions. In this study, pump inlet pressure, turbine inlet temperature and turbine inlet pressure were evaluated under different parameters. Parametric values for SRC turbine inlet temperature (T_3) and pressure (P_3) are 240–380 °C and 650–3000 kPa, respectively. In the ORC, where R152a working fluid is used, the turbine inlet temperature (T_7) and pressure (P_7) are 60–75 °C and 1400–1800 kPa, respectively. In the ORC, where R600a working fluid is used, the turbine inlet temperature and pressure are 65–75 °C and 900–1100 kPa, respectively. In the designed system, the x-mass ratio was accepted as 0.34 for the maximum benefit for day and night use [9]. According to this, 630 designs for R600 and 945 designs for R152a were formed for evaluation. The

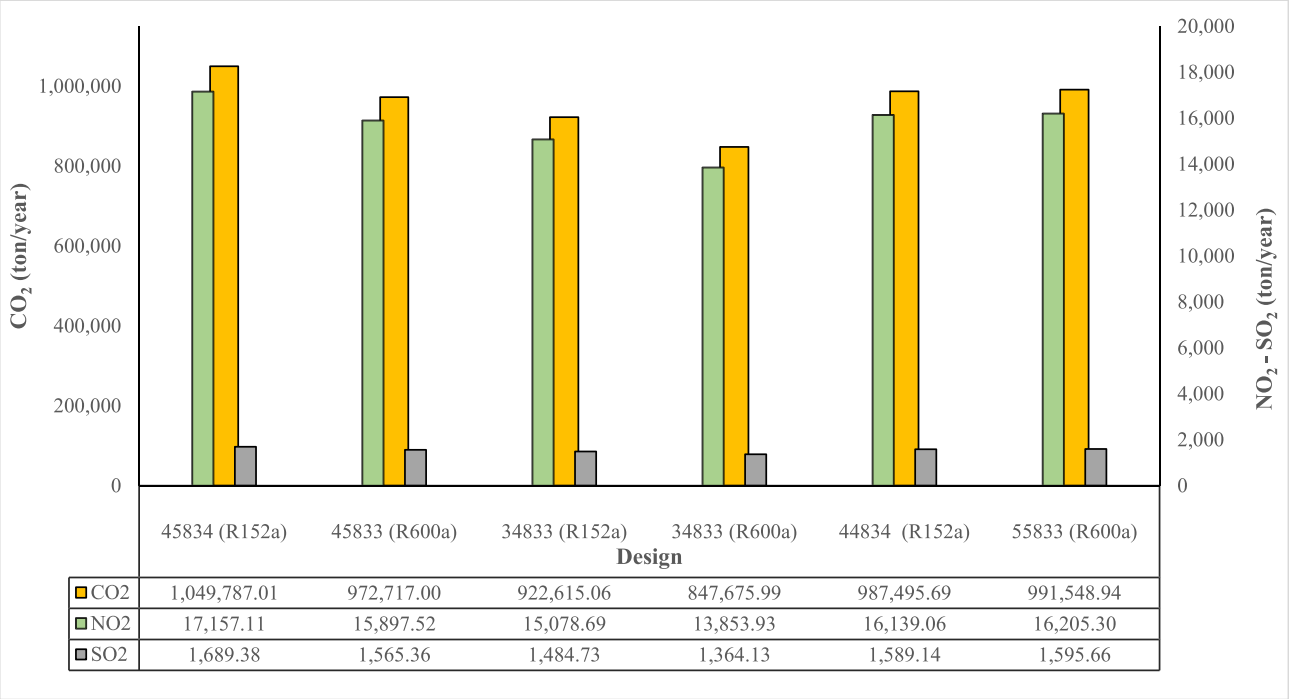

Fig. 28. The variation of the emission reduction for the optimal designs.

Table 11
Comparison and validation of the proposed system.

Reference	$I_{b,m}$ (W/m^2)	Plant type	Fluid	$\dot{W}_{net}$(MW)	η (%)	ε (%)
Present study	250	SRC-ORC	R718-R152a	37.46	12.79	13.73
		SRC-ORC	R718-R600a	34.67	11.83	12.70
	350	SRC-ORC	R718-R152a	75.63	21.86	23.46
Ref. [8]	800	SRC-ORC	R718-R134a	–	16.86	22.90
		SRC	R718	–	17.46	17.51
Ref. [9]	285	SRC	R718	19.47	11.05	11.86
		ORC	R152a	8.28	4.92	5.28
		ORC	R600a	6.41	3.99	4.29
Ref. [15]	–	SRC-ORC	R718-R152a	6.62	23.38	56.61
		ORC	R152a	3.72	21.28	60.60
Ref. [17]	800	SRC-ORC	R718-R600a	0.1	16.61	21.40
Ref. [18]	750	SRC-ORC	R718-R134a	10.5*	24.75	–
		SRC-Kalina	R718-mixture	12.5*	25.17	–
Ref. [19]	800	SRC-ORC	R718-Toluene	0.473	–	15.62

*SRC outputs not included.

identification of the model enumerating is given in Table 10.

According to Table 10, five digits were identified to define the models formed under the handled parameters. For example, model 53,213 is explained as $I_b = 541$ W/m^2, $P_2 = 1600$ kPa, $T_3 = 270$ °C, $P_6 = 1400$ kPa for R152a (900 kPa for R600a), and $T_7 = 70$ °C for R152a (75 °C for R600a). The net power generation (W_{net}) values are given in Fig. 6 and Fig. 7 for R152a and R600a, respectively.

According to the Fig. 6, the power generation ranges between 12.88 and 20.15 MW for the DNI of 150 W/m^2. These values range between 24.13–37.46 MW, 48.83–75.63 MW, 60.49–93.68 MW, and 75.66–117.12 MW for the DNI of 250 W/m^2, 350 W/m^2, 450 W/m^2, and 541 W/m^2, respectively. The SI values range between 1.08 and 1.14 for the DNI of 150 W/m^2. These values range between 1.10–1.16, 1.18–1.31, 1.17–1.29, and 1.17–1.28 for the DNI of 250 W/m^2, 350 W/m^2, 450 W/m^2, and 541 W/m^2, respectively.

According to Fig. 7, the power generation ranges between 10.99 and 18.62 MW for the DNI of 150 W/m^2. These values range between 20.65–34.67 MW, 41.85–70.01 MW, 51.84–86.72 MW, and 64.85–108.43 MW for the DNI of 250 W/m^2, 350 W/m^2, 450 W/m^2, and 541 W/m^2, respectively. The SI values range between 1.07 and 1.12 for the DNI of 150 W/m^2. These values range between 1.08–1.15, 1.15–1.28, 1.14–1.26, and 1.14–1.26 for the DNI of 250 W/m^2, 350 W/m^2, 450 W/m^2, and 541 W/m^2, respectively. The energy efficiency (η) and exergy efficiency (ε) values are given in Fig. 8 and Fig. 9 for R152a and R600a, respectively.

According to Fig. 8, the η values range between 7.12 and 11.18 % for the DNI of 150 W/m^2. These values range between 8.21–12.79 %, 14.10–21.86 %, 13.49–20.91 %, and 13.27–20.57 % for the DNI of 250 W/m^2, 350 W/m^2, 450 W/m^2, and 541 W/m^2, respectively. The ε values range between 7.65 and 12.00 % for the DNI of 150 W/m^2. These values range between 8.81–13.73 %, 15.13–23.46 %, 14.48–22.45 %, and 14.25–22.09 % for the DNI of 250 W/m^2, 350 W/m^2, 450 W/m^2, and 541 W/m^2, respectively.

According to the Fig. 9, the η values range between 6.07 and 10.33 % for the DNI of 150 W/m^2. These values range between 7.01–11.83 %, 12.07–20.23 %, 11.56–19.35 %, and 11.42–19.08 % for the DNI of 250 W/m^2, 350 W/m^2, 450 W/m^2, and 541 W/m^2, respectively. The ε values range between 6.51 and 11.09 % for the DNI of 150 W/m^2. These values

Table 12
Comparison of the single-stage and two-stage systems.

Design	Refrigerant	Single cycle							
		$\dot{W}_{net}$(MW)	η(%)	ε(%)	NPV (US$)	SI	CO_2 (ton/year)	NO_2 (ton/year)	SO_2 (ton/year)
45,834	R152a	78.55	17.53	18.82	75,714,162.54	1.23	880,644.99	14,392.75	1,417.19
45,833	R600a	78.55	17.53	18.82	75,714,162.54	1.23	880,644.99	14,392.75	1,417.19
34,833	R152a	58.67	16.95	18.19	53,345,197.81	1.22	759,708.74	12,416.24	1,222.57
34,833	R600a	58.67	16.95	18.19	53,345,197.81	1.22	759,708.74	12,416.24	1,222.57
44,834	R152a	72.68	16.22	17.41	63,963,250.67	1.21	814,415.18	13,310.33	1,310.61
55,833	R600a	98.21	17.34	18.61	72,898,792.64	1.23	897,595.78	14,669.79	1,444.47
		Two-stage cycle							
45,834	R152a	93.55	20.88	22.42	103,074,869.34	1.29	1,049,787.01	17,157.11	1,689.38
45,833	R600a	86.72	19.35	20.78	90,587,837.24	1.26	972,717.00	15,897.52	1,565.36
34,833	R152a	71.17	20.56	22.08	80,104,399.98	1.28	922,615.06	15,078.69	1,484.73
34,833	R600a	65.42	18.90	20.29	69,340,971.72	1.25	847,675.99	13,853.93	1,364.13
44,834	R152a	88.03	19.65	21.09	92,000,020.53	1.26	987,495.69	16,139.06	1,589.14
55,833	R600a	107.77	19.23	20.64	87,929,159.81	1.26	991,548.94	16,205.30	1,595.66

range between 7.53–12.70 %, 12.96–21.72 %, 12.41–20.78 %, and 12.26–20.49 % for the DNI of 250 W/m^2, 350 W/m^2, 450 W/m^2, and 541 W/m^2, respectively. The NPV values are given in Fig. 10 and Fig. 11 for R152a and R600a, respectively.

According to Fig. 10, the NPV ranges between −0.69 and 40.39 million US$ for the DNI of 150 W/m^2. These values range between 19.17–73.77 million US$, 29.43–92.13 million US$, 35.64–103.07 million US$, and 32.01–101.00 million US$ for the DNI of 250 W/m^2, 350 W/m^2, 450 W/m^2, and 541 W/m^2, respectively.

According to Fig. 11, the NPV ranges between −10.25 and 32.36 million US$ for the DNI of 150 W/m^2. These values range between 6.83–63.11 million US$, 15.73–79.96 million US$, 21.88–90.59 million US$, and 18.27–87.93 million US$ for the DNI of 250 W/m^2, 350 W/m^2, 450 W/m^2, and 541 W/m^2, respectively.

According to Figs. 6-11, the energy and exergy efficiency values increase with the increase of turbine inlet pressures. Although the higher pressure requires more power consumption to obtain the handled conditions, the enthalpy of the fluid is higher depending on the thermodynamical behavior, resulting in more power generation. Also, the highest efficiencies were obtained at a moderate solar radiation (DNI) of 350 W/m^2 even though the power generation increase with the increase of DNI. The main reason for this result can be explained by the decrease in conversion ratio depending on the reduction of the useful energy sourced by the increased losses of SF. The *NPV* values increase till a particular point of DNI with 450 W/m^2. Then, the *NPV* starts to decrease, although the net power generation increases. The first reason for this result is the rapid increase in the installation cost depending on the requirements of the equipment, such as TES and heat exchangers. The second reason is the shorter period of sunshine time for low-radiation zones since the NPV is handled for a complete year. According to the analysis, it was determined that the energy collected by the solar collectors in the systems working under the DNI of 150 W/m^2 and 250 W/m^2 could only be used to generate power during insolation and to prevent the fluid in the TES tanks from freezing. The TES system can be used actively at DNI values between 350–541 W/m^2. The lowest η, ε, W_{net}, NPV, and SI values were obtained for the design with $P_3 = 650$ kPa, $T_3 = 250$ °C, $P_7 = 900$ kPa, and $T_7 = 75$ °C. The highest η, ε, W_{net}, NPV, and SI values were obtained for the design with $P_3 = 3000$ kPa, $T_3 = 380$ °C, $P_7 = 100$ kPa, and $T_7 = 75$ °C. The variation of η, ε, and SI by the DNI is given in Fig. 12 for the highest results. The variation of W_{net} and NPV by the DNI is shown in Fig. 13. The variation of W_{net} by the DNI is given in Fig. 13 and Fig. 14, respectively.

The designed system was analyzed from the perspective of investors, engineers and consumers using the multi-criteria decision-making method. When examined from the investor's perspective, the most effective model in the design models using R152a is given in Fig. 15.

According to the Fig. 15, the design 45,834 was obtained as the most efficient design. In this case, the parameters of I_b, C_{int}, P_3, T_3, P_7 and T_7 are 450 W/m^2, 77.96 million US$, 3000 kPa, 380 °C, 1800 kPa, and 75 °C, respectively. The η, ε, SI, W_{net}, and NPV values of this design point are 20.88 %, 22.42 %, 1.29, 93.55 MW and 103.07 million US$, respectively. The energy efficiencies of components range between 78 % and 99 %, and the exergy efficiencies of components range between 79 % and 98 %. The initial investment cost is relatively high since the equipment cost of solar energy systems is relatively higher. The payback period of the system was determined to be 4.8 years as seen Fig. 16. The detailed information about the results is given in Appendix G.

When examined from the investor's perspective, the most effective model in the design models using R600a is given in Fig. 17.

According to Fig. 17, design 45,833 was obtained as the most efficient design. In this case, the parameters of I_b, C_{int}, P_3, T_3, P_7 and T_7 are 450 W/m^2, 76.81 million US$, 3000 kPa, 380 °C, 1100 kPa, and 75 °C, respectively. The η, ε, SI, W_{net}, and NPV values of this design point are 19.35 %, 20.78 %, 1.29, 86.72 MW and 90.59 million US$, respectively. The designed system targets higher net power generation with lower investment costs in these optimal solutions. The energy efficiencies of components range between 78 % and 99 %, and the exergy efficiencies of components range between 68 % and 99 %. In the light of Figs. 15 and 17, since the investor-based model is a profit-oriented approach, the optimal solutions are obtained at the DNI values (450 W/m^2) with the highest *NPV*. The initial investment cost is relatively high since the equipment cost of solar energy systems is relatively higher. The system's payback period was determined to be 5.2 years as seen Fig. 18. The detailed information about the results is given in Appendix H.

When examined from an engineering perspective, Fig. 19 shows the most effective model in the design models using R152a.

According to the Fig. 19, the design 34,833 was obtained as the most efficient design. In this case, the parameters of I_b, C_{int}, P_3, T_3, P_7 and T_7 are 350 W/m^2, 78.28 million US$, 2000 kPa, 380 °C, 1800 kPa, and 70 °C, respectively. The η, ε, SI, W_{net}, and NPV values of this design point are 20.56 %, 22.08 %, 1.28, 71.17 MW and 80.10 million US$, respectively. The energy efficiencies of components range between 74 % and 99 %, and the exergy efficiencies of components range between 80 % and 99 %. The initial investment cost is relatively high since the equipment cost of solar energy systems is relatively higher. The system's payback period has been determined to be 5.7 years as seen in Fig. 20. The detailed information about the results is given in Appendix I.

When examined from an engineering perspective, Fig. 21 shows the most effective model in the design models using R600a.

According to the Fig. 21, the design 34,833 was obtained as the most efficient design. In this case, the parameters of I_b, C_{int}, P_3, T_3, P_7 and T_7 are 350 W/m^2, 75.87 million US$, 2000 kPa, 380 °C, 1100 kPa, and 75 °C, respectively. The η, ε, SI, W_{net}, and NPV values of this design point are 18.90 %, 20.29 %, 1.25, 65.42 MW and 69.34 million US$, respectively. In the light of Figs. 17 and 18, since the engineering-based model is an efficiency-oriented approach, the optimal solutions are obtained at

the DNI values (350 W/m^2) with the highest energy and exergy efficiencies. The designed system targets the highest net power generation with lower DNI and investment cost in these optimal solutions. The energy efficiencies of components range between 74 % and 99 %, and the exergy efficiencies of components range between 80 % and 99 %. The initial investment cost is relatively high since the equipment cost of solar energy systems is relatively higher. The system's payback period was determined to be 6.2 years as seen Fig. 22. The detailed information can be seen in Appendix J.

When examined from the consumer perspective, Fig. 23 shows the most effective model in the design models using R152a.

According to the Fig. 23, the design 44,834 was obtained as the most efficient design. In this case, the parameters of I_b, C_{int}, P_3, T_3, P_7 and T_7 are 450 W/m^2, 77.95 million US$, 2000 kPa, 380 °C, 1800 kPa, and 75 °C, respectively. The η, ε, SI, W_{net}, and NPV values of this design point are 19.95 %, 21.09 %, 1.27, 88.03 MW and 92.00 million US$, respectively. Although designs 54,834 and 55,834 also have the same efficiency score, they were not determined as the most efficient since the inputs are relatively higher. The energy efficiencies of components range between 80 % and 98 %, and the exergy efficiencies of components range between 80 % and 98 %. The initial investment cost is relatively high since the equipment cost of solar energy systems is relatively higher. The system's payback period was determined to be 5.2 years as seen Fig. 24. The detailed information can be seen in Appendix K.

When examined from the consumer perspective, Fig. 25 shows the most effective model in the design models using R600a.

According to Fig. 25, design 55,833 was the most efficient design. In this case, the parameters of I_b, C_{int}, P_3, T_3, P_7 and T_7 are 541 W/m^2, 82.46 million US$, 3000 kPa, 380 °C, 1100 kPa, and 75 °C, respectively. The η, ε, SI, W_{net}, and NPV values of this design point are 19.08 %, 20.49 %, 1.27, 108.43 MW and 87.93 million US$, respectively. Since the consumer-based model is a payment-oriented approach, the optimal solutions target the lowest payment for the power consumption. Moreover, this lowest payment is directly related to lower investment costs and higher net power generation. The energy efficiencies of components range between 80 % and 98 %, and the exergy efficiencies of components range between 80 % and 98 %. The initial investment cost is relatively high since the equipment cost of solar energy systems is relatively higher. The system's payback period was determined to be 5.6 years as see Fig. 26. The detailed information can be seen in Appendix K.

According to the dynamic evaluation, the analysis results on the hourly basis are given for the optimal solutions in Fig. 27.

According to Fig. 27, the power generation increases regularly till the approximately 2300th hour of the year for all the designs. From the approximately 6600th hour, the power generation decreases regularly. Between these hours, the power generation remains stable in accordance to the installed capacity. This stable process is the main cause that affects the cost and output parameters.

Environmental analysis is based on determining the amount of harmful gas emissions to the environment if coal were used instead of solar energy in the designed system. Fig. 28 shows the environmental analysis results of the best designs obtained through multi-criteria decision-making.

According to Fig. 28, the reduction in CO_2, NO_2, and SO_2 gases for design 45,834 model is 1,049,787.01 tons/year, 17,157.11 tons/year, and 1,689.38 tons/year, respectively. The reduction in CO_2, NO_2, and SO_2 gases for design 45,833 is 972,717.00 tons/year, 15,897.52 tons/year, and 1,565.36 tons/year, respectively. The reduction in CO_2, NO_2, and SO_2 gases for design 34,833 is 922,615.06 tons/year, 15,078.69 tons/year, and 1,484.73 tons/year, respectively. The reduction in CO_2, NO_2, and SO_2 gases for design 34,833 is 847,675.99 tons/year, 13,853.93 tons/year, and 1,364.13 tons/year, respectively. The reduction in CO_2, NO_2, and SO_2 gases for design 44,834 is 987,495.69 tons/year, 16,139.06 tons/year, and 1,589.14 tons/year, respectively. The reduction in CO_2, NO_2, and SO_2 gases for design 55,833 is 991,548.94 tons/year, 16,205.30 tons/year, and 1,595.66 tons/year, respectively.

The two-stage solar power plant was compared with the single-stage one handled in the authors' previous study [9]. The handled system was also compared with similar systems in the literature. The results are given in Table 11.

According to Table 38, the present study's results agree with the literature's results. The slight differences are sourced from the different DNI values and the refrigerants. For the current conditions, single-stage working conditions were also performed. The two-stage and single-stage systems are compared as given in Table 12.

According to Table 36, it is possible to increase the power generation by 21.31 % with an NPV increase of 50.16 %. It can improve energy efficiency by 21.30 % and exergy efficiency by 21.39 %. Also, it is available to increase the CO_2, NO_2, and SO_2 reduction by 21.44 %. An increase of 4.92 is available in SI.

8. Future scope and recommendations

A two-stage solar power plant is appropriate for locations with low DNI. However, it is crucial to determine the design point of DNI for the optimal solutions since it directly affects the sizes of the equipment as well as the capitals and thermodynamic events such as losses. So, the design point of DNI should be determined separately for the considered regions since the irradiation characteristics of the regions differ. In the optimization process of solar plants, the economics of emissions is commonly ignored since there is no emission under the operating conditions. However, the optimization analysis should also consider the indirect emission reduction that occurred by preventing fossil fuel use. Also, multi-stage solar power plants should be regarded as maximizing power generation since there is still waste potential during the process. Two-stage cycles, which utilize entirely renewable energy sources and harness waste heat, are the designs with potential for further development. However, the disadvantage of these systems is that solar energy is an intermittent energy source. In the presented study, electricity production is almost non-existent during winter due to insufficient solar energy. During these months, solar thermal energy can only be utilized to prevent the freezing of the storage material in TES. Therefore, it can be suggested that these systems should be complemented with an additional environmentally friendly energy source. Hybridizing the studied plant with continuous systems such as hydrogen generation would also affect the overall system performance since it makes the handled system available to operate without thermal storage. It would decrease the investment cost; however, the cost of a hydrogen plant should be considered in a detailed economic analysis. Also, new methods such as the Stochastic Identification of Weights (SITW) [74] can be introduced into new MCDM tools such as the Ranking Comparison (RANCOM) method [75] for more sensitive solutions.

9. Conclusion

In this study, a two-stage power plant driven by parabolic trough solar collectors designed for low-radiation zones was performed. The designed system's performance was evaluated for different installation capacities working under the different solar radiation values varying between the lowest of 150 and the highest of 541 W/m^2. The analysis of the power plant was conducted from multiple perspectives, including energy, exergy, sustainability, economics, and environment for two different available working fluids. The designed system was finally optimized using the multi-criteria decision-making method from the social aspects, including investor, engineering, and consumer sights. According to the study, the following conclusions were obtained:

- The optimal solution based on the investor sight for R152a was determined as design 45834. In this design, the values of I_b, C_{inv}, P_2, T_3, P_7 and T_7 are 450 W/m^2, 77.9 million US$, 3000 kPa, 380 °C,

1800 kPa and 75 °C, respectively. The η, ε, SI, $\dot{W}_{net}$ and *NPV* values of this design point are 20.88 %, 22.42 %, 1.29, 93.55 MW and 103 million US$, respectively. The CO_2, NO_2, and SO_2 gas reduction is 1,049,787.01 tons/year, 17,157.11 tons/year, and 1,689.38 tons/year, respectively. In this design, it is possible to increase the power generation by 19.10 % with an NPV increase of 36.14 %. It can improve energy efficiency by 19.11 % and exergy efficiency by 19.13 %. Also, it is available to increase the CO_2, NO_2, and SO_2 reduction by 19.21 %.

- The optimal solution based on the investor sight for R600a was determined as design 45833. In this design, the values of I_b, C_{inv}, P_2, T_3, P_7 and T_7 are 450 W/m^2, 76.8 million US$, 3000 kPa, 380 °C, 1100 kPa, and 75 °C, respectively. The η, ε, SI, $\dot{W}_{net}$ and *NPV* values of this design point are 19.35 %, 20.78 %, 1.26, 86.72 MW and 90.5 million US$, respectively. The CO_2, NO_2, and SO_2 gas reduction is 972,717 tons/year, 15,897.52 tons/year, and 1,565.36 tons/year, respectively. In this design, it is possible to increase the power generation by 10.40 % with an NPV increase of 19.64 %. It can improve energy efficiency by 10.38 % and exergy efficiency by 10.41 %. Also, it is available to increase the CO_2, NO_2, and SO_2 reduction by 10.46 %.
- The optimal solution based on the engineering sight for R152a was determined as design 34833. In this design, the values of I_b, C_{inv}, P_2, T_3, P_7 and T_7 are 350 W/m^2, 78.2 million US$, 2000 kPa, 380 °C, 1800 kPa, and 70 °C, respectively. The η, ε, SI, $\dot{W}_{net}$ and *NPV* values of this design point are 20.56 %, 22.08 %, 1.28, 71.17 MW and 80 million US$, respectively. The CO_2, NO_2, and SO_2 gas reduction is 922,615.06 tons/year, 15,078.69 tons/year, and 1,484.73 tons/year, respectively. In this design, it is possible to increase the power generation by 21.31 % with an NPV increase of 50.16 %. It can improve energy efficiency by 21.30 % and exergy efficiency by 21.39 %. Also, it is available to increase the CO_2, NO_2, and SO_2 reduction by 21.44 %.
- The optimal solution based on the engineering sight for R600a was determined as design 34833. In this design, the values of I_b, C_{inv}, P_2, T_3, P_7 and T_7 are 350 W/m^2, 75.8 million US$, 2000 kPa, 380 °C, 1100 kPa, and 75 °C, respectively, respectively. The η, ε, SI, $\dot{W}_{net}$ and *NPV* values of this design point are 18.90 %, 20.29 %, 1.25, 65.42 MW and 69.3 million US$, respectively, respectively. The CO_2, NO_2, and SO_2 reduction is 847,675.99 tons/year, 13,853.93 tons/year, and 1,364.13 tons/year, respectively. In this design, it is possible to increase the power generation by 11.51 % with an NPV increase of 29.99 %. It can improve energy efficiency by 11.50 % and exergy efficiency by 11.55 %. Also, it is available to increase the CO_2, NO_2, and SO_2 reduction by 11.58 %.
- The optimal solution based on the consumer sight for R152a was determined as design 44834. In this design, the values of I_b, C_{inv}, P_2, T_3, P_7 and T_7 are 450 W/m^2, 77.9 million US$, 2000 kPa, 380 °C, 1800 kPa, and 75 °C, respectively. The η, ε, SI, $\dot{W}_{net}$ and *NPV* values of this design point are 19.65 %, 21.09 %, 1.27, 88.03 MW and 92 million US$, respectively. The CO_2, NO_2, and SO_2 gas reduction is 987,495.69 tons/year, 16,139.06 tons/year, and 1,589.14 tons/year, respectively. In this design, it is possible to increase the power generation by 21.12 % with an NPV increase of 43.83 %. It can improve energy efficiency by 21.15 % and exergy efficiency by 21.14 %. Also, it is available to increase the CO_2, NO_2, and SO_2 reduction by 21.25 %.
- The optimal solution based on the consumer sight for R600a was determined as design 55833. In this design, the values of I_b, C_{inv}, P_2, T_3, P_7 and T_7 are 541 W/m^2, 82.4 million US$, 3000 kPa, 380 °C, 1100 kPa, and 75 °C, respectively, respectively. The η, ε, SI, $\dot{W}_{net}$ and *NPV* values of this design point are 19.08 %, 20.49 %, 1.26, 108.43 MW and 87.9 million US$, respectively, respectively. The CO_2, NO_2, and SO_2 gas reduction is 991,548.94 tons/year, 16,205.30 tons/year, and 1,595.66 tons/year, respectively. In this design, it is possible to increase the power generation by 9.73 % with an NPV increase of 20.62 %. It can improve energy efficiency by 10.90 % and exergy efficiency by 10.91 %. Also, it is available to increase the CO_2, NO_2, and SO_2 reduction by 10.47 %.

In conclusion, it is possible to conduct profitable design for the low radiation zones from the standpoints of all handled social aspects. However, the optimal solution of investor sight differs from that of engineering and consumer sight since investor-based designs target more economic benefits without considering environmental effects. Since there is no load of environmental issues, the economic impact of emissions was not considered in the analysis for the studied region. Although there is no emission under the operating conditions for solar energy systems, indirect emissions should be considered in government regulations. So, the differences between the investor, engineering, and consumer viewpoints would be removed for the optimal solutions since all the optimal points are approximately similar from the thermodynamic point of view.

CRediT authorship contribution statement

Damla Kilic Erikgenoğlu: Writing – original draft, Visualization, Validation, Supervision, Methodology, Investigation, Formal analysis, Data curation, Conceptualization. **Oguz Arslan:** Writing – review & editing, Validation, Supervision, Methodology, Investigation, Formal analysis, Data curation, Conceptualization. **Asli Ergenekon Arslan:** Writing – original draft, Validation, Methodology, Formal analysis, Data curation.

Declaration of competing interest

The authors declare that they have no known competing financial interests or personal relationships that could have appeared to influence the work reported in this paper.

Appendix A

The daily total solar radiation incident on the horizontal plane (H_t) is given by:

$$\frac{H_t}{H_0} = a + b \bullet (S/S_0) \tag{A.1}$$

where H_0, S, and S_0 define daily extraterrestrial radiation, daily sunshine duration, and day length, respectively. a and b are the empirical coefficients and are determined by:

$$a = 0.103 + 0.000017 \bullet Z + 0.198 \bullet \cos(\varphi - \delta) \tag{A.2}$$

$$b = 0.553 + 0.165 \bullet \cos(\varphi - \delta) \tag{A.3}$$

where, φ, δ and are Z the latitude, solar declination angles and altitude of site, respectively. The φ for Bilecik is 40°. The δ occurs between the sun's rays and the equatorial plane. It takes values between –23,45°<δ < 23,45°. The δ is computed as follows [1]:

$$\delta = 23,45 \bullet \sin\left(360 \bullet \frac{284+n}{365}\right) \tag{A.4}$$

where n is the number of days in the year (starting from 1 to 365 for a usual year). The Barbaro model [34] approved for the studied area [32] was used to calculate the daily diffuse solar radiation (H_d) incident to the horizontal plane:

$$\frac{H_d}{H_t} = 1.0492 - 1.13246 \bullet K_T \tag{A.5}$$

where K_T is the day's clearness index. Accordingly, daily direct solar radiation (H_b) can be determined by [34]:

$$H_b = H_t - H_d \tag{A.6}$$

Hourly total solar radiation values (I_t) can be determined from H_t values using the relations developed by Collares-Pereira and Rabl [35,36]. Accordingly, the hourly total solar radiation (I_t) is given by:

$$I_t = H_t \frac{\pi}{24}(a + b \bullet cos\omega)\frac{cos\omega - cos\omega_s}{sin\omega_s - \frac{\pi\omega_s}{180}cos\omega_s} \tag{A.7}$$

$$a = 0.409 + 0.5016\sin(\omega_s - 60) \tag{A.8}$$

$$b = 0.6609 - 0.4767\sin(\omega_s - 60) \tag{A.9}$$

where ω is the hour angle in degrees for the time in question, and ω_s is the sunset-hour angle. The ω can be obtained as follows [1]:

$$\omega = (solartime - 12) \bullet 15 \tag{A.10}$$

The hourly diffuse solar radiation (I_d) value can be determined using the equation suggested by Liu and Jordan [36]:

$$I_d = H_d \frac{\pi}{24}\frac{\cos\omega - \cos\omega_s}{\sin\omega_s - \frac{\pi\omega_s}{180}\cos\omega_s} \tag{A.11}$$

Accordingly, the hourly beam (DNI) solar radiation (I_b) value can be determined as follows:

$$I_b = I_t - I_d \tag{A.12}$$

The useful heat energy ($\dot{Q}_u$) that can be obtained from a single collector is determined by Equation (12). This equation quantifies the amount of valuable or beneficial energy considering various factors and parameters [37]:

$$\dot{Q}_u = F_R \bullet A_r[S \bullet CR - \pi \bullet U_L \bullet (T_{11} - T_a)] \tag{A.13}$$

Here, F_R is the heat removal factor, S is the heat absorbed by the receiver,CR is the concentration ratio of the PTSC, $and U_L$ is the heat loss coefficient. T_{11} and T_a are the inlet temperature of heat transfer fluid and the ambient temperature, respectively. The concentration ratio is calculated by [1]:

$$CR = \frac{A_a}{A_r} = \frac{(D_r - D_{o.g})}{D_{o.g}} \tag{A.14}$$

where A_a and A_r are described as the aperture area and receiver area, respectively. F_R is determined by [1]:

$$F_R = \frac{\dot{m}_{11} \bullet c_{p,therminol}}{A_r \bullet U_L}\left[1 - \exp\left(-\frac{U_L \bullet F' \bullet A_r}{\dot{m}_{11} \bullet c_{p,therminol}}\right)\right] \tag{A.15}$$

Here, F' is the collector efficiency factor and is defined by [1]:

$$F' = \frac{\frac{1}{U_L}}{\frac{1}{U_L} + \frac{D_{o,r}}{h_{fl} \bullet D_{i,r}} + \left(\frac{D_o}{2k} + ln\frac{D_{o,r}}{D_{i,r}}\right)} \tag{A.16}$$

where $D_{o,r}$, and $D_{i,r}$ are the outer and inner diameters of the receiver, respectively. The heat absorbed by the receiver (S) is defined by [1]:

$$S = I_b \bullet \eta_r \tag{A.17}$$

where η_r is defined as the optical efficiency and given as [1]:

$$\eta_r = \tau_{cover} \bullet \alpha_r \bullet \tau_{PTC} \bullet \gamma \bullet k(\theta) \tag{A.18}$$

Here, τ_{cover} is the transmissivity of the glazing cover of the receiver, α_r is the absorptivity of the receiver, τ_{PTC} is the reflectance of the mirror, γ is the intercept factor, and $k(\theta)$ is the incidence angle modifier and calculated by [1,37]:

$$k(\theta) = 1 - 2.2307x10^{-4} \bullet \theta - 1.1x10^{-4} \bullet \theta^2 + 3.18596x10^{-6} \bullet \theta^3 - 4.85509x10^{-8} \bullet \theta^4 \tag{A.19}$$

where θ indicates the incidence angle and can be calculated as follows [1];

$$cos\theta = \sqrt{cos^2\theta_z + cos^2\delta \bullet sin^2\omega} \tag{A.20}$$

The expressions θ_z, given in the equation denote the zenith angles. These values can be determined by [1]:

$$cos\theta_z = cos\varphi \bullet cos\delta \bullet cos\omega + sin\varphi \bullet sin\delta \tag{A.21}$$

Appendix B

The inlet heat of *HST* can be defined by [42]:

$$\dot{Q}_{hst} = \dot{Q}_{14} - \dot{Q}_{l,HST} \tag{B.1}$$

Here, $\dot{Q}_{l,HST}$ refers to the heat lost from the storage tank during the charging period, and it is calculated by [42,43]:

$$\dot{Q}_{l,HST} = (UA)_{HST} \bullet (T_{HST} - T_a) \tag{B.2}$$

where U and A are the overall heat transfer coefficient and heat transfer surface area of the storage tank, respectively. The $(UA)_{HST}$ is calculated by [9,44]:

$$(UA)_{HST} = \frac{1}{R_{top}} \tag{B.3}$$

Here, R_{top} is the total thermal resistance of the tank walls. R_{salt}, R_{ss}, R_{im}, and R_{air} refer to the thermal resistance of storage, stainless steel, insulation, and outside air, respectively. R_{top} is calculated by [9,44]:

$$R_{top} = R_{salt} + R_{ss} + R_{im} + R_{air} \tag{B.4}$$

$$R_{top} = \frac{1}{(2\pi r_1 L)h_{salt}} + \frac{\ln(r_2/r_1)}{2\pi L k_{ss}} + \frac{\ln(r_3/r_2)}{2\pi L k_{im}} + \frac{1}{(2\pi r_3 L)h_{air}} \tag{B.5}$$

The total heat gain of the tank during the day can be calculated by [42]:

$$\sum Q_{HST} = \dot{Q}_{HST} \bullet \Delta t_h \tag{B.6}$$

Here, Δt_h predicates the total charging time. The temperature of the *HST* can be determined by [42]:

$$T_{hst} = \frac{\sum Q_{HST}}{c_{p,HST} \bullet m_{HST}} \tag{B.7}$$

Here, m_{hst} is the total mass in the *HST*. The change in the temperature of the *HST* can be calculated by [42]:

$$T^{+}_{HST} = T_{HST} + \frac{\Delta t_h}{m_{HST} \bullet c_{p,HST}} \bullet (-(UA)_{HST} \bullet (T_{HST} - T_a) \tag{B.8}$$

The total amount of heat lost from the *HST* during the storage process is defined by [42]:

$$Q_{HST,tlost} = m_{HST} \bullet c_{p,HST} \bullet \Delta T_{HST} \tag{B.9}$$

Here, ΔT_{hst} refers to the temperature change in the *HST* and can be calculated by [42]:

$$\Delta T_{HST} = T_{HST} - T^{+}_{HST} \tag{B.10}$$

The equation that expresses the heat given by the total heat stored during insolation in the absence of insolation is defined as [42]:

$$Q_{15} = \sum Q_{HST} - Q_{HST,tlost} \tag{B.11}$$

The calculation methods mentioned here can be similarly applied to the *CST*. Accordingly, the heat given during the discharge time from the *CST* is expressed by [42]:

$$Q_{17} = \sum Q_{CST} - Q_{CST,tlost} \tag{B.12}$$

Appendix C

The heat exchanger area (A_{HE}) can be expressed by [47,48]:

$$A_{HE} = \frac{\dot{Q}_{HE}}{U \bullet \Delta T_{LMTD}} \tag{C.1}$$

where U is the total heat transfer coefficient. ΔT_{LMTD} is defined logarithmic mean temperature difference and is calculated by [48]:

$$\Delta T_{LMTD} = \frac{(T_{h,i} - T_{c,o}) - (T_{h,o} - T_{c,i})}{ln\left(\frac{T_{h,i}-T_{c,o}}{T_{h,o}-T_{c,i}}\right)} \tag{C.2}$$

The U is calculated by [49]:

$$U = \frac{D_{o,t}}{D_{i,t}}\frac{1}{h_i} + \frac{\ln(D_{o,t}/D_{i,t})}{2\pi kL} + \frac{1}{h_o} + \frac{D_{o,t}}{D_{i,t}}R''_{fi} + R''_{fo} \tag{C.3}$$

Where $D_{i,t}$ and $D_{o,t}$ are the inlet and outlet diameters of the tube side, respectively. Fouling factors (R''_f) are taken as 0.0002 m^2K/W in this study [63]. The h_i is the heat transfer coefficient of the tube side and calculated as [49]:

$$h_i = \frac{Nu \bullet k}{D_{i,t}} \tag{C.4}$$

The Nusselt number (Nu) can be determined depending on the Reynold number (Re). Accordingly, the Re number can be calculated as [64]:

$$Re = \frac{4 \bullet \dot{m}_c}{\mu \bullet \pi \bullet D_{i,t} \bullet \frac{N_T}{n_{pass}}} \tag{C.5}$$

where N_T and n_{pass} are defined as the total number of tubes and passes, respectively. The N_T can be calculated as [50]:

$$N_T = 0.785 \bullet \left(\frac{CTP}{CL}\right) \bullet \frac{D_s^2}{P_t^2 \bullet D_{o,t}^2} \tag{C.6}$$

where CTP, CL, D_s, P_t, and $D_{o,t}$ are defined as tube count calculation constant, tube layout constant, shell diameter, tube pitch, and outer diameter of the tube, respectively. CTP and CL values can be achieved from the Table 5.

Table C1
CTP and *CL* values [50].

Tube layout angle	***CL***
For 90° and 45°	1
For 30° and 60°	0.85
Number of passes	***CTP***
One pass	0.93
Two passes	0.9
Three passes	0.85

The tube pitch is calculated by [50]:

$$P_t = PR \bullet D_{o,t} \tag{C.7}$$

where PR indicates the pitch ratio. The Nu is determined to quantify the convection heat transfer on the tube side of the heat exchanger [49,65]:

$$Nu = 0.023 \bullet Re^{0.8} \bullet Pr^{0.3} \quad for \quad Re > 10^4 \text{ and } 0.6 < Pr < 100 \tag{C.8}$$

The heat transfer coefficient of the shell side (h_o) is calculated by [49]:

$$h_o = \frac{Nu \bullet k}{D_e} \tag{C.11}$$

where D_e is the equivalent diameter. This value depends on the layout angle and is calculated for 30° or 60° layout angle as [64]:

$$D_e = \frac{1.27}{D_{o,t}}(P_t^2 - 0.785 \bullet D_{o,t}^2) \tag{C.12}$$

The Re of the shell side is given by [64]:

$$Re_{shell} = \frac{D_e \bullet \dot{m}_h}{\mu \bullet A_s} \tag{C.13}$$

where A_s is the cross-sectional area of the shell perpendicular to the flow direction and is calculated by [64]:

$$A_s = 0.639 \bullet (P_t - D_{o,t}) \bullet e \bullet \sqrt{\frac{CL}{CTP} \bullet \pi \bullet N_T} \tag{C.14}$$

where e is the baffle spacing. The Nu of the shell side is given by [64]:

$$Nu = (0.037 \bullet Re_{shell}^{0.8} - 871) \bullet Pr^{1/3} 5.10^5 < Re_{shell} < 10^7 \; Pr = 0.6 - 50 \tag{C.15}$$

The average heat transfer coefficient for the phase change process on the outer surface of N_T horizontal pipes is given [48]:

$$h_{shell} = 0.729 \bullet \left[\frac{g \bullet \rho_l \bullet (\rho_l - \rho_v) \bullet k_l^3 \bullet h_{fg} + \left(0.68 \bullet C_{p,l} \bullet |T_{sat} - T|\right)}{N_T \bullet \mu_l \bullet |T_{sat} - T| \bullet D_e} \right]^{0.25} \tag{C.16}$$

where g is the acceleration of gravity.

Appendix D

The U for the flat plate heat exchanger is calculated [50]:

$$U = \frac{1}{\frac{1}{h_i} + \frac{t}{k} + \frac{1}{h_o}} \tag{D.1}$$

where t, k, and h are defined as plate thickness, thermal conductivity of material, and heat transfer coefficient (inlet and outlet), respectively. The heat transfer coefficient is calculated by [50]:

$$h = \frac{Nu \bullet k}{D_h} \tag{D.2}$$

where D_h is the hydraulic diameter calculated by [63]:

$$D_h = 2 \bullet b \tag{D.3}$$

where b is the average distance between the plates. The Nusselt number is given by [50]:

$$Nu = 0.2 \bullet Re^{0.67} \bullet Pr^{0.4} \bullet \left(\frac{\mu}{\mu_o}\right)^{0.1} \tag{D.4}$$

The Nusselt number at macro-scale for phase change case is given by [66]:

$$Nu = 18.495 \bullet \left(\frac{\beta}{\beta_{max}}\right)^{0.248} \bullet \left(\frac{G \bullet x \bullet D_h}{\mu_v}\right)^{0.235} \bullet \left(\frac{G \bullet D_h}{\mu_l}\right)^{0.351} \bullet \left(\frac{(\rho_l - \rho_v) \bullet g \bullet D_h^2}{\sigma}\right)^{0.235} \bullet \left(\frac{q}{G \bullet h_{lv}}\right)^{0.198} \bullet \left(\frac{\rho_l}{\rho_v}\right)^{-0.223} \tag{D.5}$$

where β is chevron angle ($\beta_{max} = 45\ ^\circ C$), G is mass flux, ρ is the density, g is the acceleration of gravity, σ is the surface tension, x is the dryness friction, μ is the dynamic viscosity, q is the transferred heat, and h_{lv} is the latent heat of phase change.

Appendix E

The NPV can be expressed as [52]:

$$NPV = \sum_{t=0}^{n} \frac{B_t}{(1+r)^t} \tag{E.1}$$

where n, B_t, and r are defined as the project's useful life, cash flow in t he year of t, and discount rate, respectively. The B_t value is calculated [9]:

$$B_t = C_e - C_{mr} - C_p \tag{E.2}$$

where C_e, C_{mr}, and C_p are defined as the gain of electricity, cost of maintenance and repair, and total annual personnel expenses, respectively. The cost analysis of the designed system includes the initial investment, operating cost, and salvage cost [52]. The cost of initial investment (C_{int}) is calculated by:

$$C_{int} = C_{inv} - C_{sal} \tag{E.3}$$

where C_{inv} and C_{sal} are defined as the investment cost of the system and the salvage cost of the plan, respectively. C_{sal} was taken as 10 % of the investment cost. The investment cost of the system (C_{inv}) is composed of the cost of the solar field (C_{SF}), thermal energy storage system (C_{TES}), and power block (C_{PB}).

$$C_{inv} = C_{SF} + C_{TES} + C_{PB} \tag{E.4}$$

C_{SF} and C_{TES} values were taken as respectively, 150 \$/m^2 [67] and 25,68 \$/kWh [68]. The cost of all system equipment was calculated to determine the C_{PB}. The equipment costs were modified for the year 2023 by *CEPCI*. The cost of the heat exchanger is calculated [69]:

$$C_{HE} = \frac{CEPCI_{2023}}{CEPCI_{2001}} \bullet F_{BM,HE} \bullet C_{0,HE} \tag{E.5}$$

where $CEPCI_{2001}$ and $CEPCI_{2023}$ are defined as the Chemical Engineering Plant Cost Index in 2001 and 2023, respectively. The $CEPCI$ index in 2001 and 2023 are 397 [69] and 789.6 [70], respectively. $C_{0,HE}$ and $F_{BM,HE}$ are respectively defined as the purchase cost of equipment and bare module cost factor, and are calculated as [69]:

$$F_{BM,HE} = \left[B_{1,HE} + (B_{2,HE} \bullet F_{M,HE} \bullet F_{P,HE})\right] \tag{E.6}$$

$$logF_{P,HE} = \left[c_{1,HE} + c_{2,HE}(logP_{HE}) + c_{3,HE}(logP_{HE})^2\right] \tag{E.7}$$

$$logC_{0,HE} = \left[K_{1,HE} + K_{2,HE}(logA_{HE}) + K_{3,HE}(logA_{HE})^2\right] \tag{E.8}$$

where C_{HE}, $F_{M,HE}$, $F_{P,HE}$, A_{HE}, and P_{HE} are the cost, the material factor, pressure factor, surface area, and pressure for heat exchangers, respectively. The cost of the turbine is calculated by [69]:

$$C_T = \frac{CEPCI_{2023}}{CEPCI_{2001}} \bullet F_{BM,T} \bullet C_{0,T} \tag{E.9}$$

$$logC_{0,T} = \left[K_{1,T} + K_{2,T}\left(log\dot{W}_T\right) + K_{3,T}\left(log\dot{W}_T\right)^2\right] \tag{E.10}$$

where $C_{0,T}$ and $F_{BM,T}$ are the initial cost and the bare module cost factor of the turbine, respectively. The cost of the pump is calculated by [69]:

$$C_P = \frac{CEPCI_{2023}}{CEPCI_{2001}} \bullet F_{BM,p} \bullet C_{0,p} \tag{E.11}$$

$$F_{BM,p} = \left[B_{1,p} + (B_{2,p} \bullet F_{M,p} \bullet F_{P,p})\right] \tag{E.12}$$

$$logF_{P,p} = \left[c_{1,p} + c_{2,p}(logP_p) + c_{3,p}(logP_p)^2\right] \tag{E.13}$$

$$logC_{0,p} = \left[K_{1,p} + K_{2,p}\left(log\dot{W}_p\right) + K_{3,HE}\left(log\dot{W}_p\right)^2\right] \tag{E.14}$$

where $C_{0,p}$, $F_{P,p}$, and P_p are defined as the initial cost, pressure factor, and pressure of the pump, respectively. B_1, B_2, K_1, K_2, K_3, c_1, c_2, and c_3 are constants related to the material used in each equipment within the cycle, and their values are given in Table 8.

Table E1
The constant of the cost equations [69].

Constants	Equipment			
	Shell and Tube HE	Flat Plate HE	Turbine	Pump
K_1	4.2768	4.6656	2.6259	3.3892
K_2	−0.0495	−0.1557	1.4398	0.0536
K_3	0.1431	0.1547	−0.1776	0.1538
B_1	1.63	0.96	–	1.89
B_2	1.66	1.21	–	1.35
c_1	0	0	0	−0.3935
c_2	0	0	0	0.3957
c_3	0	0	0	−0,0023
F_M	2.73	2.45	–	2.2
F_P	1	1	–	–
F_{BM}	–	–	11.6	–

The labor force requirement for the power plant was determined based on the personnel needed, including one engineer and ten workers. To calculate the personnel expenses, the minimum wage for 2024, which was 548.45 $, was considered. According to this, the total annual personnel expense is given by [9]:

$$C_p = 548.45 \bullet 12 \bullet (2.1 \bullet 1 + 1.2 \bullet 10) \tag{E.15}$$

The unit cost of electricity is assumed to be 0.133 $ [71]. Accordingly, the electricity cost is calculated by:

$$C_e = \dot{W}_{net} \bullet 0.133 \tag{E.16}$$

Appendix F

Efficiency Analysis Technique with Output Satisficing (EATWOS) is a sufficient technique depending on the successful results for energy problems

since it maximizes the output values for the minimal input values [60]. So, the efficiency of the i^{th} design with inlet parameters in a number of k is given by [28,60]:

$$E_i = \sum_{j=1}^{n} \frac{\left[op_j\right] \bullet \left[v_j\right]_{AHP}}{\left[ip_1 \quad \cdots \quad ip_k\right] \bullet \left[w_j\right]_{AHP}} \tag{F.1}$$

where j indicates the output parameter obtained by the thermodynamic analysis of the energy system. w_k and v_j are the weights of input and output parameters, respectively. ip_{ik} and op_{ik} are the distance matrices for the input and output values, respectively:

$$ip_{ik} = 1 + \frac{x_{ik}}{\sqrt{\sum_{i=1}^{K} x_{ik}^2}} - \min_i\{s_k\} \tag{F.2}$$

$$op_{ij} = 1 + \frac{y_{ij}}{\sqrt{\sum_{i=1}^{I} y_{ij}^2}} - \max_i\{r_j\} \tag{F.3}$$

where x and y are the input and output values, respectively. AHP can determine the degree of importance of the output parameters to be used for the weighting of input and output parameters in terms of the importance of scaling of experts given in Table 10.

Table F1
Importance scale [72].

Scale	Value Definitions
1	The equal importance of both factors
3	The first factor is more important than the second factor
5	The first factor is much more important than the second factor
7	The fact that the first factor has extreme importance compared to the second factor
9	The fact that the first factor has absolute superiority than the second factor
2,4,6,8	Intermediate values

According to this scale, a comparison matrix is formed for the output parameters (decision points) in a number n of the energy problem. Taking the relationship of $a_{ji} = \frac{1}{a_{ij}}$ between the matrix elements, the comparison matrix is given by [73]:

$$\mathbf{A} = \begin{bmatrix} 1 & \cdots & a_{1n} \\ \vdots & \ddots & \vdots \\ a_{n1} & \cdots & 1 \end{bmatrix} \tag{F.4}$$

where a_{ij} is the importance scale of the i^{th} criteria compared to the j^{th} criteria. For the next step, $\mathbf{A}$ is normalized using the formulation of $b_{ij} = \frac{a_{ij}}{\sum_{i=1}^{n} a_{ij}}$ to give the significance matrix $\mathbf{B}$:

$$\mathbf{B} = \begin{bmatrix} b_{11} & \cdots & b_{1n} \\ \vdots & \ddots & \vdots \\ b_{n1} & \cdots & b_{nn} \end{bmatrix} \tag{F.5}$$

Finally, the weighting matrix are determined as:

$$\left[v_j\right]_{AHP} = \begin{bmatrix} v_1 \\ \vdots \\ v_n \end{bmatrix} \tag{F.6}$$

where v_n is calculated by:

$$v_n = \frac{\sum_{j=1}^{n} b_{ij}}{n} \tag{F.7}$$

The obtained weights are acceptable if the consistency ratio of the determined weights (CR) is less than 0.10. The CR is given using with Random indicators (RI) [72,73]:

$$CR = \frac{CI}{RI} \tag{F.8}$$

where CI is the consistency indicator given by [72,73]:

$$CI = \frac{\gamma - n}{n - 1} \tag{F.9}$$

where γ is calculated with the following equation:

$$\gamma = \frac{\sum_{i=1}^{n} d_i}{n} \tag{F.10}$$

where

$$d_i = \frac{c_i}{v_i} \tag{F.11}$$

c_i is obtained from following matrix operation:

$$\mathbf{C} = \begin{bmatrix} 1 & \cdots & a_{1n} \\ \vdots & \ddots & \vdots \\ a_{n1} & \cdots & 1 \end{bmatrix} \times \begin{bmatrix} v_1 \\ \vdots \\ v_n \end{bmatrix} = \begin{bmatrix} c_1 \\ \vdots \\ c_n \end{bmatrix} \tag{F.12}$$

Random indicator (*RI*) is taken from the following table [72,73]:

Table F2
Random indicator scale [72,73].

n	*RI*	*n*	*RI*
3	0.58	8	1.41
4	0.90	9	1.45
5	1.12	10	1.49
6	1.24	11	1.51
7	1.32	12	1.48

Appendix G

.

Table G1
Thermodynamic properties of design 45,834 during insolation for R152a.

Point	Fluid	$\dot{m}$kg/s	*T* °C	*P* kPa	*h* kJ/kg	*s* kJ/kgK	*E* kW	*ψ*kj/kg
1	R718	108.37	81.32	50	340.54	1.0912	36905.6	19.76
2	R718	108.37	81.35	3000	343.57	1.0912	37234.8	22.79
3	R718	108.37	380	3000	3185.87	6.8543	345265.5	1146.81
4	R718	108.37	81.32	50	2503.75	6.8543	271341.2	464.69
5	R152a	815.8	40.03	910	271.41	1.2413	221428.8	63.42
6	R152a	815.8	40.35	1800	272.44	1.2413	222273.5	64.46
7	R152a	815.8	75	1800	554.05	2.0731	452020.3	98.04
8	R152a	815.8	42.97	910	535.57	2.0731	436939.4	79.55
9	Air	18,907	28.9	–	428.4	3.890	8,099,636	1.141
10	Air	18,907	40	–	439.54	3.927	8,310,836	1.059
11	Terminol VP-I	769.12	120	15	181.3	0.54	139441.1	20.59
12	Terminol VP-I	261.5	400	23	800.5	1.71	209330.9	291.85
13	Terminol VP-I	261.5	120	15	181.3	0.54	47409.98	18.75
14	Molten Salt	342.6	390	–	483.06	–	165507.5	210.25
18	Molten Salt	342.6	111	–	19.92	–	6825.1	17.33

Table G2
Thermodynamic properties of design 45,834 during non-sunshine time for R152a.

Point	Fluid	$\dot{m}$kg/s	*T* °C	*P* kPa	*h* kJ/kg	*s* kJ/kgK	*E* kW	*ψ*kj/kg
1	R718	29.75	81.32	50	340.54	1.0912	10131.6	19.76
2	R718	29.75	81.35	3000	343.57	1.0912	10,222	22.79
3	R718	29.75	380	3000	3185.87	6.8543	94784.97	1146.81
4	R718	29.75	81.32	50	2503.75	6.8543	74490.67	464.69
5	R152a	223.97	40.03	910	271.41	1.2413	60788.35	63.42
6	R152a	223.97	40.35	1800	272.44	1.2413	61020.23	64.46
7	R152a	223.97	75	1800	554.05	2.0731	124092.1	98.04
8	R152a	223.97	42.97	910	535.57	2.0731	119952.2	79.55
9	Air	2880	20	–	419.4	3.860	1,208,283	1.207
10	Air	2880	40	–	439.54	3.927	1,266,263	1.059
15	Molten Salt	189.21	387.8	–	479.54	–	90,733	214.99
16	Molten Salt	189.21	387.9	–	479.54	–	90,733	214.99
17	Molten Salt	189.21	113.15	–	23.49	–	4444.26	20.35

Table G3
Energy and Exergy analysis results of Thermodynamic properties of design 45,834 for R152a.

Component	$\dot{E}_{mass,i}$kW	$\dot{E}_{mass,o}$kW	$\dot{Q}$kW	$\dot{W}$kW	$\dot{E}x_{mass,i}$kW	$\dot{E}x_{mass,o}$kW	$\dot{E}x_Q$kW	$\dot{E}x_W$kW	$\dot{E}x_d$kW	η %	ε %
PTSC	139441.1	209330.7	528367.6	542.12	15836.1	76318.7	294344.2	542.12	233319.4	80	85
HST	90733.7*	91399.7*	919.58*	–	40678.2*	39781.4*	540.80*	–	356	98*	97*
CST	4444.5*	3769.1*	269.55*	3.78	3850.42*	3279*	77.89	3.79	497.32	84*	85*
HE-I	161920.9	158652.5	3238.4	–	82255.49	76940.82	1804.06	–	7118.74	98	91
HE-II	86288.7*	84562.9*	1725.77*	–	91411.27*	37970.48*	947.38*	–	54388.21*	98*	81*
HE-III	314317.0	308030.7	6286.34	–	150,619	133803.3	3502.01	–	20317.77	98	87
HE-IV	234435.6	229746.8	4688.71	–	102947.9	82123.04	744.93	–	21569.76	97	79
	64359.6*	63071.06*	1287.57*	–	28262.7*	22545.8*	204.50*	–	5921.10*	97*	79*
Pump- I	36905.59	37234.86	–	411.58	2141.40	2470.66	–	411.48	82.32	99	97
	10131.61*	10222*	–	112.99*	587.84*	678.42*	–	112.99*	22.60*	99*	97*
Pump- II	221428.8	222273.5	–	1055.84	51743.4	52588.1	–	1055.84	211.16	99	98
	60788.38*	61020.98*	–	289.85*	14205.2*	14436.8*	–	289.85*	57.90*	99*	98*
Turbine- I	345265.5	271341.2	–	62835.7	124284.2	50359.8	–	62835.7	11088.7	79	91
	94784.5*	74490.58*	–	17250.6*	34119.8*	13825.8*	–	17250.6*	3044.34*	78*	91*
Turbine- II	452020.3	436939.4	–	12818.75	79981.6	64900.7	–	12818.75	2262.13	96	97
	124092.1*	119952.1*	–	3519.7*	21957.7*	17717.7*	–	3519.7*	621.24*	96*	97*
Condenser	215510.6	211200.4	4310.21	378.16	86482.02	71769.4	245.01	378.16	14845.7	98	83
	59163.7*	57980.9*	1183.79*	57.62*	21295.62*	17256.66*	67.26*	57.62*	4029.32*	98*	81*
Overall system										20.88	22.42

*defines TES mode.

Table G4
The *NPV* analysis results of design 45,834 for R152a.

	Today	5	10	15	20
Investment					
Solar Field cost	−67,736,850.0	–	–	–	–
TES cost	−10,460,523.84	–	–	–	–
PB cost	−8,427,561.28	–	–	–	–
Cash flow (US$)					
Expenses					
Maintenance and repair cost	–	−584,718.31	−584,718.31	−584,718.31	−584,718.31
Personnel expenses	–	−92,798.01	−92,798.01	−92,798.01	−92,798.01
Incomes					
Electricity Production	–	21,942,090.94	21,942,090.94	21,942,090.94	21,942,090.94
Scrap cost	–	–	–	–	8,662,493.51
Total cash flow	–	19,135,456.17	19,135,456.17	19,135,456.17	19,135,456.17
Cumulative cash flow	−77,962,441.61	28,360,461.46	134,418,729.91	241,006,177.60	347,329,050.67
Discount rate (%13)	1.00	0.62	0.39	0.24	0.15
Present Value	−77,962,441.61	13,203,627.80	8,198,414.05	5,090,570.10	3,160,843.52
***NPV* (US$)**	103,074,869.34				

Appendix H

.

Table H1
Thermodynamic properties of design 45,833 during insolation for R600a.

Point	Fluid	$\dot{m}$kg/s	T °C	P kPa	h kJ/kg	s kJ/kgK	E kW	ψkj/kg
1	R718	108.37	81.32	50	340.54	1.0912	36905.6	19.76
2	R718	108.37	81.35	3000	343.57	1.0912	37234.8	22.79
3	R718	108.37	380	3000	3185.87	6.8543	345265.5	1146.81
4	R718	108.37	81.32	50	2503.75	6.8543	271341.2	464.69
5	R600a	645.8	41.32	550	299.66	1.3369	193517.4	51.51
6	R600a	645.8	41.54	1100	300.69	1.3369	194189.4	52.55
7	R600a	645.8	75	1100	656.45	2.3816	423936.2	96.80
8	R600a	645.8	43.72	550	643.26	2.3816	415410.1	83.60
9	Air	19,467	28.9	–	428.4	3.890	8,339,458	1.141
10	Air	19,467	40	–	439.54	3.927	8,556,912	1.059
11	Terminol VP-I	769.12	120	15	181.3	0.54	139441.1	20.59
12	Terminol VP-I	261.5	400	23	800.5	1.71	209330.9	291.85
13	Terminol VP-I	261.5	120	15	181.3	0.54	47409.98	18.75
14	Molten Salt	342.6	390	–	483.06	–	165507.5	210.25
18	Molten Salt	342.6	111	–	19.92	–	6825.1	17.33

Table H2
Thermodynamic properties of design 45,833 during non-sunshine time for R600a.

Point	Fluid	$\dot{m}$kg/s	T °C	P kPa	h kJ/kg	s kJ/kgK	E kW	ψkj/kg
1	R718	29.75	81.32	50	340.54	1.0912	10131.6	19.76
2	R718	29.75	81.35	3000	343.57	1.0912	10,222	22.79
3	R718	29.75	380	3000	3185.87	6.8543	94784.97	1146.81
4	R718	29.75	81.32	50	2503.75	6.8543	74490.67	464.69
5	R600a	177.28	41.32	550	299.66	1.3369	53126.17	51.51
6	R600a	177.28	41.54	1100	300.69	1.3369	53310.36	52.55
7	R600a	177.28	75	1100	656.45	2.3816	116382.2	96.80
8	R600a	177.28	43.72	550	643.26	2.3816	114041.6	83.60
9	Air	2966.17	20	–	419.4	3.860	1,244,059	1.207
10	Air	2966.17	40	–	439.54	3.927	1,303,756	1.059
15	Molten Salt	189.21	387.8	–	479.54	–	90,733	214.99
16	Molten Salt	189.21	387.9	–	479.54	–	90,733	214.99
17	Molten Salt	189.21	113.15	–	23.49	–	4444.26	20.35

Table H3
Energy and Exergy analysis results of design 45,833 for R600a.

Component	$\dot{E}_{mass,i}$kW	$\dot{E}_{mass,o}$kW	$\dot{Q}$kW	$\dot{W}$kW	$\dot{E}x_{mass,i}$kW	$\dot{E}x_{mass,o}$kW	$\dot{E}x_{Q}$kW	$\dot{E}x_{W}$kW	$\dot{E}x_{d}$kW	η %	ε %
PTSC	139441.1	209330.7	528367.6	542.12	15836.1	76318.7	294344.2	542.12	233319.4	80	85
HST	90733.7*	91399.7*	919.58*	–	40678.2*	39781.4*	540.80*	–	356	98*	97*
CST	4444.5*	3769.1*	269.55*	3.78	3850.42*	3279*	77.89	3.79	497.32	84*	85*
HE-I	161920.9	158652.5	3238.4	–	82255.49	76940.82	1804.06	–	7118.74	98	91
HE-II	86288.74*	84562.2*	1725.61*	–	91411.04*	37970.03*	947.20*	–	54388.21*	98*	81*
HE-III	314317.0	308030.7	6286.34	–	150,619	133803.3	3502.01	–	20317.77	98	87
HE-IV	234435.6	229746.8	4688.71	–	84294.92	64656.18	744.93	–	20383.68	98	76
	64359.6*	63071.06*	1287.57*	–	23141.37*	17749.73*	204.50*	–	5595.89*	98*	76*
Pump- I	36905.59	37234.86	–	411.58	2141.40	2470.66	–	411.48	82.32	99	97
	10131.61*	10222*	–	112.99*	587.84*	678.42*	–	112.99*	22.60*	99*	97*
Pump- II	193518.4	19189.4	–	838.68	33264.18	33935.13	–	838.68	167.73	98	99
	53126.78*	53310.74*	–	230.95*	9131.52*	9316.49*	–	230.95*	46.05*	98*	99*
Turbine- I	345265.5	271341.2	–	62835.7	124284.2	50359.8	–	62835.7	11088.7	80	91
	94784.5*	74490.58*	–	17250.6*	34119.8*	13825.8*	–	17250.6*	3044.34*	78*	91*
Turbine- II	423936.2	415410.1	–	7247.18	62514.78	53988.68	–	7247.18	1278.91	97	98
	116382.8*	114041.1*	–	1989.07*	17162.59*	14821.87*	–	1989.07*	351.66*	97*	98*
Condenser	221891.7	217453.9	4437.83	389.36	76208.94	53883.2	1113.06	389.36	21,602	98	72
	60915.3*	59697.51*	1218.78*	59.32*	18402.55*	12273.18*	305.57*	59.32*	5882.44*	98*	68*
Overall system										19.35	20.78

*defines TES mode.

Table H4
The *NPV* analysis results of design 45,833 for R600a.

	Today	5	10	15	20
Investment					
Solar Field cost	−67,736,850.0	–	–	–	–
TES cost	− 10,608,979.87	–	–	–	–
PB cost	−6,997,319.07	–	–	–	–
Cash flow (US$)					
Expenses					
Maintenance and repair cost	–	−576,066.26	−576,066.26	−576,066.26	−576,066.26
Personnel expenses	–	−92,798.01	−92,798.01	−92,798.01	−92,798.01
Incomes					
Electricity Production	–	20,331,214.46	20,331,214.46	20,331,214.46	20,331,214.46
Scrap cost	–	–	–	–	8,534,314.89
Total cash flow	–	19,662,350.20	19,662,350.20	19,662,350.20	19,662,350.20
Cumulative cash flow	−76,808,834.04	21,502,916.94	119,814,667.92	218,126,418.91	316,438,169.89
Discount rate (%13)	1.00	0.62	0.39	0.24	0.15
Present Value	−76,808,834.04	12,208,772.50	7,580,687.17	4,707,010.31	2,922,683.07
***NPV* (US$)**	90,587,837.24				

Appendix I

.

Table I1
Thermodynamic properties of design 34,833 during insolation for R152a.

Point	Fluid	$\dot{m}$kg/s	T °C	P kPa	h kJ/kg	s kJ/kgK	E kW	ψkj/kg
1	R718	81.86	81.32	50	340.54	1.0912	27876.84	19.76
2	R718	81.86	81.35	2000	342.54	1.0912	28041.21	21.76
3	R718	81.86	380	2000	3204.22	7.0626	262300.2	1103.05
4	R718	81.86	81.32	50	2569.27	7.0626	210322.3	468.09
5	R152a	654.6	40.03	910	271.41	1.2413	177661.4	63.42
6	R152a	654.6	40.35	1800	272.44	1.2413	178339.1	64.46
7	R152a	654.6	70	1800	545.58	2.0487	357135.7	96.87
8	R152a	654.6	40.03	910	527.48	2.0487	345282.4	78.76
9	Air	12,002	26.4	–	425.9	3.881	5,111,531	1.16
10	Air	12,002	40	–	439.54	3.927	5,275,800	1.059
11	Terminol VP-I	584.94	120	15	181.3	0.54	106045.7	20.59
12	Terminol VP-I	198.9	400	23	800.5	1.71	159197.2	291.85
13	Terminol VP-I	198.9	120	15	181.3	0.54	36055.53	19.93
14	Molten Salt	260.6	390	–	483.06	–	125869.3	210.25
18	Molten Salt	260.6	111	–	19.92	–	5190.5	17.33

Table I2
Thermodynamic properties of design 34,833 during non-sunshine time for R152a.

Point	Fluid	$\dot{m}$kg/s	T °C	P kPa	h kJ/kg	s kJ/kgK	E kW	ψkj/kg
1	R718	28.94	81.32	50	340.54	1.0912	9856.68	19.76
2	R718	28.94	81.35	2000	342.54	1.0912	9914.65	21.76
3	R718	28.94	380	2000	3204.22	7.0626	92743.3	1103.05
4	R718	28.94	81.32	50	2645.2	7.0626	74365.52	468.09
5	R152a	231.44	40.03	910	271.41	1.2413	62816.45	63.42
6	R152a	231.44	40.35	1800	272.44	1.2413	63056.78	64.46
7	R152a	231.44	70	1800	545.58	2.0487	126274.1	96.87
8	R152a	231.44	40.03	910	527.48	2.0487	121935.1	78.76
9	Air	2299.7	14.9	–	414.3	3.842	952,653	1.245
10	Air	2299.7	40	–	439.54	3.927	1,010,735	1.059
15	Molten Salt	185.32	387.8	–	479.54	–	88872.81	221.95
16	Molten Salt	185.32	387.88	–	479.54	–	88872.81	221.95
17	Molten Salt	185.32	113.15	–	23.49	–	4353.85	22.76

Table I3
Energy and Exergy analysis results of design 34,833 for R152a.

Component	$\dot{E}_{mass,i}$kW	$\dot{E}_{mass,o}$kW	$\dot{Q}$kW	$\dot{W}$kW	$\dot{E}x_{mass,i}$kW	$\dot{E}x_{mass,o}$kW	$\dot{E}x_Q$kW	$\dot{E}x_W$kW	$\dot{E}x_d$kW	η %	ε %
PTSC	106045.7	159197.2	401826.2	542.12	12043.9	58048.9	296,097	542.12	249549.8	74	83
HST	89520.6*	88868.3*	926.63*	–	41131.7*	38963.5*	544.9*	–	1623.3*	98*	94*
CST	4353.16*	3691.6*	282.64*	3.7*	4217.8*	3211.6*	76.3*	3.7*	933.6*	84*	76*
HE-I	123141.7	120678.8	2462.8	–	62555.7	58748.2	1372.0	–	5179.4	98	92
HE-II	84518.9*	82828.6*	1690.3*	–	89502.1*	36145.3*	927.8*	–	54284.5*	98*	80*
HE-III	239039.7	234258.9	4780.7	–	114449.5	97990.6	2663.2	–	19122.1	98	83
HE-IV	182445.4	178796.5	3648.9	–	80512.0	65030.5	579.7	–	16061.2	98	80
	64508.9*	63218.3*	1290.5*	–	28467.5*	22993.2*	204.98*	–	5678.9*	98*	80*
Pump- I	27876.8	28041.2	–	205.50	1617.52	1781.92	–	205.50	41.10	99	98
	9856.5*	9914.6*	–	72.66*	571.92*	630.28*	–	72.66*	14.51*	99*	98*
Pump- II	177661.4	178339.1	–	847.1	41515.8	42193.5	–	847.1	169.4	96	99
	62816.4*	63056.7*	–	299.51*	14679.1*	14918.4*	–	299.51*	59.93*	96*	99*
Turbine- I	262300.2	210322.3	–	44181.2	90296.3	38318.4	–	44181.2	7796.7	80	91
	92743.2*	74365.5*	–	15621.4*	31926.7*	13548.0*	–	15621.4*	2756.3*	80*	91*
Turbine- II	357135.7	345282.3	–	10075.3	63413.0	51559.6	–	10075.3	1778.0	98	97
	126274.1*	122083.1*	–	3562.40*	22421.37*	18230.1*	–	3562.40*	628.6*	98*	97*
Condenser	167620.9	164268.5	3352.4	240.1	65482.0	54228.6	160.8	240.1	11332.5	98	83
	59266.6*	58081.7*	1185.8*	45.99*	21093.7*	17114.6*	56.82*	45.93*	3968.2*	98*	81*
Overall system										20.56	22.07

*defines TES mode.

Table I4
The *NPV* analysis results of design 34,833 for R152a.

	Today	5	10	15	20
Investment					
Solar Field cost	−67,736,850.0	–	–	–	–
TES cost	−10,383,600.54	–	–	–	–
PB cost	−8,847,783.96	–	–	–	–
Cash flow (US$)					
Expenses					
Maintenance and repair cost	–	−587,120.41	−587,120.41	−587,120.41	−587,120.41
Personnel expenses	–	−92,798.01	−92,798.01	−92,798.01	−92,798.01
Incomes					
Electricity Production	–	19,284,010.30	19,284,010.30	19,284,010.30	19,284,010.30
Scrap cost	–	–	–	–	8,698,080.18
Total cash flow	–	18,604,091.88	18,604,091.88	18,604,091.88	18,604,091.88
Cumulative cash flow	−78,282,721.66	14,737,737.72	107,758,197.10	200,778,656.48	298,799,115.87
Discount rate (%13)	1.00	0.62	0.39	0.24	0.15
Present Value	−78,282,721.66	11,551,677.34	7,172,682.78	4,453,671.68	2,765,379.71
***NPV* (US$)**	80,104,399.98				

Appendix J

.

Table J1
Thermodynamic properties of design 34,833 during insolation for R600a.

Point	Fluid	$\dot{m}$kg/s	*T* °C	*P* kPa	*h* kJ/kg	*s* kJ/kgK	*E* kW	ψkj/kg
1	R718	81.86	81.32	50	340.54	1.0912	27876.84	19.76
2	R718	81.86	81.35	2000	342.54	1.0912	28041.21	21.76
3	R718	81.86	380	2000	3204.22	7.0626	262300.2	1103.05
4	R718	81.86	81.32	50	2569.27	7.0626	210322.3	468.09
5	R600a	502.6	41.32	550	299.66	1.3369	150602.4	51.51
6	R600a	502.6	41.54	1100	300.69	1.3369	151124.6	52.55
7	R600a	502.6	75	1100	656.45	2.3816	329921.1	96.80
8	R600a	502.6	42.54	550	643.26	2.3816	323285.8	83.60
9	Air	12365.4	26.4	–	425.9	3.881	5,265,910	1.16
10	Air	12365.4	40	–	439.54	3.927	5,435,140	1.059
11	Terminol VP-I	584.94	120	15	181.3	0.54	106045.7	20.59
12	Terminol VP-I	198.9	400	23	800.5	1.71	159197.2	291.85
13	Terminol VP-I	198.9	120	15	181.3	0.54	36055.53	19.93
14	Molten Salt	260.6	390	–	483.06	–	125869.3	210.25
18	Molten Salt	260.6	111	–	19.92	–	5190.5	17.33

Table J2
Thermodynamic properties of design 34,833 during non-sunshine time for R600a.

Point	Fluid	$\dot{m}$kg/s	*T* °C	*P* kPa	*h* kJ/kg	*s* kJ/kgK	*E* kW	ψkj/kg
1	R718	28.94	81.32	50	340.54	1.0912	9856.68	19.76
2	R718	28.94	81.35	2000	342.54	1.0912	9914.65	21.76
3	R718	28.94	380	2000	3204.22	7.0626	92743.3	1103.05
4	R718	28.94	81.32	50	2645.2	7.0626	74365.52	468.09
5	R600a	177.70	41.32	550	299.66	1.3369	53249.5	51.51
6	R600a	177.70	41.54	1100	300.69	1.3369	53434.1	52.55
7	R600a	177.70	75	1100	656.45	2.3816	116652.4	96.80
8	R600a	177.70	41.54	550	640.93	2.3816	114306.2	83.60
9	Air	2368.9	14.9	–	414.3	3.842	981425.2	1.245
10	Air	2368.9	40	–	439.54	3.927	104126.1	1.059
15	Molten Salt	185.32	387.8	–	479.54	–	88872.81	221.95
16	Molten Salt	185.32	387.88	–	479.54	–	88872.81	221.95
17	Molten Salt	185.32	113.15	–	23.49	–	4353.85	22.76

Table J3
Energy and Exergy analysis results of design 34,833 for R600a.

Component	$\dot{E}_{mass,i}$ kW	$\dot{E}_{mass,o}$ kW	$\dot{Q}$ kW	$\dot{W}$ kW	$\dot{E}x_{mass,i}$ kW	$\dot{E}x_{mass,o}$ kW	$\dot{E}x_Q$ kW	$\dot{E}x_W$ kW	$\dot{E}x_d$ kW	η %	ε %
PTSC	106045.7	159197.2	401826.2	542.12	12043.9	58048.9	296,097	542.12	249549.8	74	83
HST	89520.6*	88868.3*	926.63*	–	41131.7*	38963.5*	544.9*	–	1623.3*	98*	94*
CST	4353.16*	3691.6*	282.64*	3.7*	4217.8*	3211.6*	76.3*	3.7*	933.6*	84*	76*
HE-I	123141.7	120678.8	2462.8	–	62555.7	58748.2	1372.0	–	5179.4	98	92
HE-II	84518.9*	82828.6*	1690.3*	–	89502.1*	36145.3*	928.8*	–	54284.5*	98*	80*
HE-III	239039.7	234258.9	4780.7	–	114449.5	97990.6	2663.2	–	19122.1	98	83
HE-IV	182445.4	178796.5	3648.9	–	64727.9	50268.5	579.7	–	15039.0	98	77
	64508.9*	63218.3*	1290.5*	–	22886.4*	17773.1*	204.7*	–	5317.9*	98*	77*
Pump- I	27876.8	28041.2	–	205.50	1617.52	1781.92	–	205.50	41.10	99	98
	9856.5*	9914.6*	–	72.66*	571.22*	630.28*	–	72.66*	14.51*	99*	98*
Pump- II	150602.4	151124.5	–	652.6	25887.2	26409.4	–	652.6	130.5	96	99
	53249.6*	53434.0*	–	230.4*	9153.9*	9337.3*	–	230.4*	46.16*	96*	99*
Turbine- I	262300.2	210322.3	–	44181.2	90296.3	38318.4	–	44181.2	7796.7	80	91
	92743.2*	74365.5*	–	15621.4*	31926.7*	13548.0*	–	15621.4*	2756.3*	80*	91*
Turbine- II	329921.1	323285.8	–	5639.9	48651.0	42015.7	–	5639.9	995.2	98	98
	116652.3*	114306.1*	–	1994.7*	17201.9*	14855.7*	–	1994. 7*	351.4*	98*	98*
Condenser	172683.4	169229.7	3453.6	247.31	56358.6	38983.9	866.2	247.31	16755.7	98	70
	61056.4*	59835.8*	1221.6*	47.32*	17805.7*	11662.9*	306.90*	47.32*	5884.20*	98*	67*
Overall system										18.90	20.29

*defines TES mode.

Table J4
The *NPV* analysis results of design 34,833 for R600a.

	Today	**5**	**10**	**15**	**20**
Investment					
Solar Field cost	−67,736,850.0	–	–	–	–
TES cost	−10,396,167.88	–	–	–	–
PB cost	−6,161,863.27	–	–	–	–
Cash flow (US$)					
Expenses					
Maintenance and repair cost	–	−568,990.45	−568,990.45	−568,990.45	−568,990.45
Personnel expenses	–	−92,798.01	−92,798.01	−92,798.01	−92,798.01
Incomes					
Electricity Production	–	17,717,673.58	17,717,673.58	17,717,673.58	17,717,673.58
Scrap cost	–	–	–	–	8,429,488.12
Total cash flow	–	17,055,885.12	17,055,885.12	17,055,885.12	17,055,885.12
Cumulative cash flow	75,865,393.04	9,414,032.56	94,693,458.16	179,972,883.75	265,252,309.35
Discount rate (%13)	1.00	0.62	0.39	0.24	0.15
Present Value	−75,865,393.04	10,590,362.75	6,575,782.05	4,083,043.29	2,535,248.64
***NPV* (US$)**	69,340,971.72				

Appendix K

.

Table K1
Thermodynamic properties of design 44,834 during insolation for R152a.

Point	Fluid	$\dot{m}$ kg/s	T °C	P kPa	h kJ/kg	s kJ/kgK	E kW	ψ kj/kg
1	R718	107.64	81.32	50	340.54	1.0912	36655.6	19.76
2	R718	107.64	81.35	2000	342.54	1.0912	36871.8	21.76
3	R718	107.64	380	2000	3204.22	7.0626	344902.6	1103.05
4	R718	107.64	81.32	50	2569.27	7.0626	276556.1	468.09
5	R152a	834.9	40.03	910	271.41	1.2413	226590.4	63.42
6	R152a	834.9	40.35	1800	272.44	1.2413	227454.8	64.46
7	R152a	834.9	75	1800	554.05	2.0731	462557.2	98.04
8	R152a	834.9	42.97	910	535.57	2.0731	447124.8	79.55
9	Air	19348.7	28.9	–	428.4	3.890	8,288,443	1.141
10	Air	19348.7	40	–	439.54	3.927	8,504,567	1.059
11	Terminol VP-I	769.12	120	15	181.3	0.54	139441.1	20.59
12	Terminol VP-I	261.5	400	23	800.5	1.71	209330.9	291.85
13	Terminol VP-I	261.5	120	15	181.3	0.54	47409.98	18.75
14	Molten Salt	342.6	390	–	483.06	–	165507.5	210.25
18	Molten Salt	342.6	111	–	19.92	–	6825.1	17.33

Table K2
Thermodynamic properties of design 44,834 during non-sunshine time for R152a.

Point	Fluid	$\dot{m}$kg/s	T °C	P kPa	h kJ/kg	s kJ/kgK	E kW	ψkj/kg
1	R718	29.55	81.32	50	340.54	1.0912	10,063	19.76
2	R718	29.55	81.35	2000	342.54	1.0912	10122.35	21.76
3	R718	29.55	380	2000	3204.22	7.0626	94685.32	1103.05
4	R718	29.55	81.32	50	2569.22	7.0626	75922.31	468.1
5	R152a	229.19	40.03	910	271.41	1.2413	62205.3	63.42
6	R152a	229.19	40.35	1800	272.44	1.2413	62442.65	64.46
7	R152a	229.19	75	1800	554.05	2.0731	126984.8	98.04
8	R152a	229.19	42.97	910	535.57	2.0731	122748.1	79.55
9	Air	2948	20	–	419.4	3.860	1,236,448	1.207
10	Air	2948	40	–	439.54	3.927	1,295,780	1.059
15	Molten Salt	189.21	387.8	–	479.54	–	90,733	214.99
16	Molten Salt	189.21	387.9	–	479.54	–	90,733	214.99
17	Molten Salt	189.21	113.15	–	23.49	–	4444.26	20.35

Table K3
Energy and Exergy analysis results of design 44,834 for R152a.

Component	$\dot{E}_{mass,i}$kW	$\dot{E}_{mass,o}$kW	$\dot{Q}$kW	$\dot{W}$kW	$\dot{E}x_{mass,i}$kW	$\dot{E}x_{mass,o}$kW	$\dot{E}x_{Q}$kW	$\dot{E}x_{W}$kW	$\dot{E}x_{d}$kW	η %	ε %
PTSC	139441.1	209330.7	528367.6	542.12	15836.1	76318.7	294344.2	542.12	233319.4	80	85
HST	90733.7*	91399.7*	919.58*	–	40678.2*	39781.4*	540.80*	–	356	98*	97*
CST	4444.5*	3769.1*	269.55*	3.78	3850.42*	3279*	77.89	3.79	497.32	84*	85*
HE-I	161920.9	158652.5	3238.4	–	82255.49	76940.82	1804.06	–	7118.74	98	91
HE-II	86288.7*	84562.9*	1725.77*	–	91376.27*	36446.26*	947.38*	–	55877.37*	98*	81*
HE-III	314317.0	308030.7	6286.34	–	150,619	133803.3	3502.01	–	20317.77	98	87
HE-IV	239900.4	235102.4	4798.0	–	104199.5	83972.9	762.29	–	20988.83	98	80
	65859.3*	64542.12*	1317.18*	–	28605.65*	23052.9*	209.27*	–	5762.02*	98*	80*
Pump- I	36655.59	36871.87	–	270.22	2126.40	2343.66	–	270.22	54.04	99	98
	10063.61*	10122*	–	74.18*	583.84*	643.42*	–	74.18*	14.84*	99*	98*
Pump- II	226590.4	227454.8	–	1080.45	52949.57	5381.93	–	1080.45	216.1	99	99
	62205.36*	62442.65*	–	296.6*	14536.12*	14773.4*2	–	296.6*	59.52*	99*	99*
Turbine- I	344902.5	276556.2	–	58094.7	118732.2	50385.8	–	58094.7	10252.7	80	91
	94685.5*	75922.58*	–	15948.6*	32595.8*	13832.23*	–	15948.6*	2814.4*	80*	91*
Turbine- II	462557.2	447124.8	–	13117.56	81846.06	66413.63	–	13117.56	2314.86	96	97
	126984.8*	122748.1*	–	3601.13*	22469.01*	18232.38*	–	3601.13*	635.49*	96*	97*
Condenser	220534.3	216123.6	4410.68	386.97	88497.97	73442.45	250.72	386.97	15191.76	98	83
	60542.78*	59331.93*	1210.85*	58.96*	21791.6*	17658.48*	68.83*	58.96*	4123.28*	98*	81*
Overall system										19.65	21.09

*defines TES mode.

Table K4
The *NPV* analysis results of design 44,834 for R152a.

	Today	5	10	15	20
Investment					
Solar Field cost	−67,736,850.00	–	–	–	–
TES cost	−10,460,523.84	–	–	–	–
PB cost	−8,417,491.62	–	–	–	–
Cash flow (US$)					
Expenses					
Maintenance and repair cost	–	−584,650.34	−584,650.34	−584,650.34	−584,650.34
Personnel expenses	–	−92,798.01	−92,798.01	−92,798.01	−92,798.01
Incomes					
Electricity Production	–	20,640,110.88	20,640,110.88	20,640,110.88	20,640,110.88
Scrap cost	–	–	–	–	8,661,486.55
Total cash flow	–	19,962,662.53	19,962,662.53	19,962,662.53	19,962,662.53
Cumulative cash flow	−77,953,378.92	21,859,933.72	121,673,246.36	221,486,559.01	321,299,871.65
Discount rate (%13)	1.00	0.62	0.39	0.24	0.15
Present Value	−77,953,378.92	12,395,242.83	7,696,470.58	4,778,902.69	2,967,322.58
***NPV* (US$)**	92,000,020.53				

Appendix L

.

Table L1
Thermodynamic properties of design 55,833 model during insolation for R600a.

Point	Fluid	$\dot{m}$kg/s	T °C	P kPa	h kJ/kg	s kJ/kgK	E kW	ψkj/kg
1	R718	131.99	81.32	50	340.54	1.0912	44947.82	19.76
2	R718	131.99	81.35	3000	342.54	1.0912	45348.84	22.79
3	R718	131.99	380	3000	3204.22	6.8543	420503.6	1146.81
4	R718	131.99	81.32	50	2503.75	6.8543	276556.1	464.69
5	R600a	786.5	41.32	550	299.66	1.3369	235688.7	51.51
6	R600a	786.5	41.54	1100	300.69	1.3369	236505.9	52.55
7	R600a	786.5	75	1100	656.45	2.3816	516317.7	96.80
8	R600a	786.5	41.32	550	643.26	2.3816	505933.6	83.60
9	Air	25802.15	29.8	–	429.3	3.893	11,076,290	1.135
10	Air	25802.15	40	–	439.54	3.927	11,341,130	1.059
11	Terminol VP-I	936.72	120	15	181.3	0.54	169827.2	20.59
12	Terminol VP-I	318.5	400	23	800.5	1.71	254946.9	291.85
13	Terminol VP-I	318.5	120	15	181.3	0.54	57741.26	18.75
14	Molten Salt	417.3	390	–	483.06	–	201573.9	210.25
18	Molten Salt	417.3	111	–	19.92	–	8312.3	17.33

Table L2
Thermodynamic properties of design 55,833 during non-sunshine time for R600a.

Point	Fluid	$\dot{m}$kg/s	T °C	P kPa	h kJ/kg	s kJ/kgK	E kW	ψkj/kg
1	R718	40.56	81.32	50	340.54	1.0912	13811.39	19.76
2	R718	40.56	81.35	3000	342.54	1.0912	13934.61	22.79
3	R718	40.56	380	3000	3185.8	6.8543	129210.7	1146.8
4	R718	40.56	81.32	50	2383.37	6.8543	101545.5	464.6
5	R600a	241.67	41.32	550	299.66	1.3369	72421.5	51.51
6	R600a	241.67	41.54	1100	300.69	1.3369	72672.59	52.55
7	R600a	241.67	75	1100	656.45	2.3816	158652.1	96.80
8	R600a	241.67	41.32	550	643.26	2.3816	155461.3	83.60
9	Air	4023	20	–	419.4	3.852	1,687,056	1.207
10	Air	4023	40	–	439.54	3.927	1,768,435	1.059
15	Molten Salt	257.27	388.2	–	480.11	–	123519.9	215.45
16	Molten Salt	257.27	388.2	–	480.11	–	123519.9	215.45
17	Molten Salt	257.27	112.79	–	22.90	–	5891.2	20.25

Table L3
Energy and Exergy analysis results of design 55,833 for R600a.

Component	$\dot{E}_{mass,i}$kW	$\dot{E}_{mass,o}$kW	$\dot{Q}$kW	$\dot{W}$kW	$\dot{E}x_{mass,i}$kW	$\dot{E}x_{mass,o}$kW	$\dot{E}x_{Q}$kW	$\dot{E}x_{W}$kW	$\dot{E}x_{d}$kW	η %	ε %
PTSC	169827.2	254946.9	643506.1	542.12	19287.1	92954.2	382,385	542.12	308175.8	81	85
HST	124276.8*	123517.9*	1013.14*	–	55428.8*	54091.01*	595.82*	–	741.98*	97*	98*
CST	5124.8*	5891.48*	286.04*	5.14*	5209.71*	4458.4*	82,65*	5,14*	673.8*	86*	87*
HE-I	197205.7	193261.5	3944.1	–	100180.0	93572.1	2197.1	–	8805.1	98	91
HE-II	117628.6*	115276.1*	2352.5*	–	124444.4*	51723.1*	1292.0*	–	74013.3*	97*	86*
HE-III	382810.9	375154.8	7656.2	–	183,441	162698.5	4265.1	–	2007.61	97	86
HE-IV	285522.2	279811.8	5710.44	–	102663.9	78745.63	907.26	–	24825.5	97	76
	87734.15*	85979.47*	1754.68*	–	31546.17*	24196.65*	278.78*	–	7628.30	97*	76*
Pump- I	44947.8	45348.8	–	501.27	2608.04	3009.05	–	501.27	100.25	99	97
	13811.39*	13934.61*	–	154.03*	801.39*	924.61*	–	154.03*	30.81*	99*	97*
Pump- II	235688.7	236505.9	–	1021.44	40512.9	41330.05	–	1021.44	204.28	98	99
	72421.5*	72672.59*	–	313.86*	12448.6*	1269.7*	–	313.86*	62.77*	98*	99*
Turbine- I	420503.6	330471.1	–	76528.5	151367.4	61333.88	–	76528.5	13505.0	80	91
	129210.7*	101545.5*	–	23515.38*	46511.58*	18846.43*	–	23515.38*	4149.77*	80*	91*
Turbine- II	516317.7	505933.6	–	8826.44	76137.5	65573.5	–	8826.44	1557.60	97	98
	158652.1*	155461.3*	–	2712.15*	23395.26*	20204.49*	–	2712.15*	478.62*	97*	98*
Condenser	270244.9	264,840	5404.89	516.04	95031.69	67840.8	1355.61	516.04	26351.2	96	82
	83039.79*	81379*	1660.79*	80.47*	25065.01*	16709.92*	416.55*	80.47*	8019.01*	96	80
Overall system										19.08	20.49

*defines TES mode.

Table L4
The *NPV* analysis results of design 55,833 for R600a.

	Today	5	10	15	20
Investment					
Solar Field cost	−67,736,850.00	–	–	–	–
TES cost	− 15,116,068.88	–	–	–	–
PB cost	− 8,766,945.85	–	–	–	–
Cash flow (US$)					
Expenses					
Maintenance and repair cost	–	−618,434.09	−618,434.09	−618,434.09	−618,434.09
Personnel expenses	–	−92,798.01	−92,798.01	−92,798.01	−92,798.01
Incomes					
Electricity Production	–	20,724,829.66	20,724,829.66	20,724,829.66	20,724,829.66
Scrap cost	–	–	–	–	9,161,986.47
Total cash flow	–	20,013,597.56	20,013,597.56	20,013,597.56	20,013,597.56
Cumulative cash flow	−82,457,878.26	17,610,109.53	117,678,097.32	217,746,085.11	317,814,072.91
Discount rate (%13)	1.00	0.62	0.39	0.24	0.15
Present Value	−82,457,878.26	12,426,869.48	7,716,108.24	4,791,096.13	2,974,893.75
***NPV* (US$)**	87,929,159.81				

Data availability

No data was used for the research described in the article.

References

[1] Kalogirou SA. Solar energy engineering: processes and systems. Cambridge, MA: Academic Press (Elsevier); 2013.
[2] Lovegrove K, Stein W. Concentrating solar power technology: principles, developments and applications. Cambridge: Woodhead Publishing; 2012.
[3] Boukelia TE, Arslan O, Mecibah MS. ANN-based optimization of a parabolic trough solar thermal power plant. *Appl Therm Eng* 2016;107:1210–8.
[4] Boukelia TE, Arslan O, Mecibah MS. Potential assessment of a parabolic trough solar thermal power plant considering hourly analysis: ANN-based approach. *Renew Energy* 2017;105:324–33.
[5] Mosleh HJ, Ahmadi R. Linear parabolic trough solar power plant assisted with latent thermal energy storage system: A dynamic simulation. *Appl Therm Eng* 2019;161:114204.
[6] Yazdi M, Manesh MHK. Dynamic 6E analysis of direct steam generator solar parabolic trough collector power plant with thermal energy storage. *Sustainable Energy Technol Assess* 2022;49:101759.
[7] Ata S, Köse Ö, Tutumlu H, Yağli H, Koç Y, Koç A. Which power cycle is the best fit for parabolic trough solar collectors? A comparative and comprehensive case study for six sub-configurations of the three main cycles. *Energ Conver Manage* 2023;291:117338.
[8] Boukelia TE, Arslan O, Bouraoui A. Thermodynamic performance assessment of a new solar tower-geothermal combined power plant compared to the conventional solar tower power plant. Energy 2021;232:121109.
[9] Arslan O, Kilic D. Concurrent optimization and 4E analysis of organic Rankine cycle power plant driven by parabolic trough collector for low-solar radiation zone. *Sustainable Energy Technol Assess* 2021;46:101230.
[10] Al-Sulaiman FA. Exergy analysis of parabolic trough solar collectors integrated with combined steam and organic Rankine cycles. *Energ Conver Manage* 2014;77:441–9.
[11] AlKassem A. A performance evaluation of an integrated solar combined cycle power plant with solar tower in Saudi Arabia. *Renewable Energy Focus* 2021;39:123–38.
[12] Bahari M, Ahmadi A, Dashti R. Exergo-economic analysis and optimization of a combined solar collector with steam and Organic Rankine Cycle using particle swarm optimization (PSO) algorithm. *Cleaner Eng Technol* 2021;4:100221.
[13] Li P, Qian T, Li J, Lin H, Wang Y, Pei G, et al. Thermo-economic analysis of a novel partial cascade organic-steam Rankine cycle. *Energ Conver Manage* 2023;283:116941.
[14] Khandelwal N, Sharma M, Singh O, Shukla AK. Comparative evaluation of Integrated Solar combined cycle plant with cascade thermal storage system for different heat transfer fluids. *J Clean Prod* 2022;353:131519.
[15] Nazari N, Heidarnejad P, Porkhial S. Multi-objective optimization of a combined steam-organic Rankine cycle based on exergy and exergo-economic analysis for waste heat recovery application. *Energ Conver Manage* 2016;127:366–79.
[16] Cao Y, Li P, Qiao Z, Ren S, Si F. A concept of a supercritical CO_2 Brayton and organic Rankine combined cycle for solar energy utilization with typical geothermal as auxiliary heat source: Thermodynamic analysis and optimization. *Energy Rep* 2022;8:322–33.
[17] Li J, Li P, Pei G, Alvi JZ, Ji J. Analysis of a novel solar electricity generation system using cascade Rankine cycle and steam screw expander. *Appl Energy* 2016;165:627–38.
[18] Mirjavadi K, Pourfayaz F, Pourmoghadam P, Kasaeian A. A comparison of using organic Rankine and Kalina cycles as bottom cycles in a solar-powered steam Rankine cycle. *Energy Sci Eng* 2022;10(8):2714–31.
[19] Habibi H, Zoghi M, Chitsaz A, Shamsaiee M. Thermo-economic performance evaluation and multi-objective optimization of a screw expander-based cascade Rankine cycle integrated with parabolic trough solar collector. *Appl Therm Eng* 2020;180:115827.
[20] Arslan O, Ozgur MA, Kose R. Electricity Generation Ability of the Simav Geothermal Field: A Technoeconomic Approach. *Energy Sources Part A* 2012;34(12):1130–44.
[21] Arslan O, Arslan AE. Pareto principle-based advanced exergetic evaluation of geothermal district heating system: Simav case study. *Journal of Building Engineering* 2022;58:105035.
[22] Turja AI, Sadat KN, Hasan MM, Khan Y, Ehsan MM. Waste Heat Recuperation in Advanced Supercritical CO_2 Power Cycles with Organic Rankine Cycle Integration & Optimization Using Machine Learning Methods. *International Journal of Thermofluids* 2024;22:100612.
[23] Khan Y, Naqib-Ul-Islam SM, Faruque MW, Ehsan MM. Advanced Cascaded Recompression Absorption System Equipped with Ejector and Vapor-Injection Enhanced Vapor Compression Refrigeration System: ANN based Multi-Objective Optimization. *Therm Sci Eng Prog* 2024;49:102485.
[24] Turja AI, Khan IA, Rahman S, Mustakim A, Hossain MI, Ehsan MM, et al. Machine learning-based multi-objective optimization and thermal assessment of supercritical CO_2 Rankine cycles for gas turbine waste heat recovery. *Energy AI* 2024;16:100372.
[25] Ehsan MM, Guan Z, Gurgenci H, Klimenko A. Novel design measures for optimizing the yearlong performance of a concentrating solar thermal power plant using thermal storage and a dry-cooled supercritical CO_2 power block. *Energ Conver Manage* 2020;216:112980.
[26] Turja AI, Hasan MM, Ehsan MM, Khan Y. Multi-objective performance optimization & thermodynamic analysis of solar powered supercritical CO_2 power cycles using machine learning methods & genetic algorithm. Energy AI 2024;15:100327.
[27] Arslan O, Arslan AE, Acar MS. Multi-criteria making-decision modeling of b-type ORC-Binary geothermal power plant: EATWOS analysis. BSEU Journal of Science 2019;6(1):222–36.
[28] Arslan AE, Arslan O, Genc MS. Hybrid modeling for the multi-criteria decision making of energy systems: An application for geothermal district heating system. *Energy* 2024;286:129590.
[29] GEPA (General Directorate of Renewable Energy of Turkish Republic). 2023. Solar atlas of Bilecik, https://gepa.enerji.gov.tr/MyCalculator/pages/11.aspx. [accessed 05 May 2023].
[30] Daneshazarian R, Cuce E, Cuce PM, Sher F. Concentrating photovoltaic thermal (CPVT) collectors and systems: Theory, performance assessment and applications. *Renew Sustain Energy Rev* 2018;81:473–92.
[31] Yuksel YE. Thermodynamic assessment of modified Organic Rankine Cycle integrated with parabolic trough collector for hydrogen production. *Int J Hydrogen Energy* 2018;43(11):5832–41.
[32] Altiokka ABG, Arslan O. Design and optimization of absorption cooling system operating under low solar radiation for residential use. *Journal of Building Engineering* 2023;106697.
[33] Bakirci K. Models of solar radiation with hours of bright sunshine: a review. Renew Sustain Energy Rev 2009;13:2580–8.
[34] Barbaro S, Cannata G, Coppolino S, Leone C, Sinagra E. Diffuse solar radiation statistics for Italy. *Sol Energy* 1981;26(5):429–35.
[35] Collares-Pereira M, Rabl A. The average distribution of solar radiation-correlations between diffuse and hemispherical and between daily and hourly insolation values. *Sol Energy* 1979;22:155–64.
[36] Tiwari GN, Tiwari A. Handbook of Solar Energy: Theory, Analysis and Applications. Singapore: Springer; 2016.

[37] Duffie JA, Beckman WA. Solar engineering of thermal processes. 2nd ed. New York: Wiley; 1991.

[38] Mantha D, Wang T, Reddy RG. Thermodynamic modeling of eutectic point in the $LiNO_3$–$NaNO_3$–KNO_3–$NaNO_2$ quaternary system. *Sol Energy Mater Sol Cells* 2013;118:18–21.

[39] Cengel YA, Boles MA, Kanoğlu M. Thermodynamics: an engineering approach 2011;Vol. 5:p. 445)..

[40] Al-Maliki WAK, Hadi AS, Al-Khafaji HM, Alobaid F, Epple B. Novel feedwater preheating system for parabolic trough solar power plant. Energy Rep 2022;8:10665–87.

[41] Al-Maliki WAK, Alsaedi SS, Khafaji HQ, Alobaid F, Epple B. A novel dual feedwater circuit for a parabolic trough solar power plant. Sci Rep 2023;13(1):7471.

[42] Al-Sulaiman FA, Hamdullahpur F, Dincer I. Performance assessment of a novel system using parabolic trough solar collectors for combined cooling, heating, and power production. *Renew Energy* 2012;48:161–72.

[43] Javadi MA, Abhari MK, Ghasemiasl R, Ghomashi H. Energy, exergy and exergy-economic analysis of a new multigeneration system based on double-flash geothermal power plant and solar power tower. Sustainable Energy Technol Assess 2021;47:101536.

[44] Arslan O, Ozgur MA, Yildizay HD, Kose R. Fuel effects on optimum insulation thickness: an exergitic approach. *Energy Sources Part A* 2009;32(2):128–47.

[45] Solutia. Properties of THERMINOL-VP1. accessed 5 May 2022, http://twt.mpei.ac.ru/tthb/hedh/htf-vp1.pdf;; 2020.

[46] Refprop. Reference Fluid thermodynamics and transport properties. NIST reference database, Version 9.0. National Institute of Standards. NIST, USA: and Technology; 2010.

[47] Lee H. Thermal design: heat sinks, thermoelectrics, heat pipes, compact heat exchangers, and solar cells. John Wiley & Sons; 2022.

[48] Bergman TL, Lavine AS, Incropera FP, DeWitt DP. Introduction to heat transfer. John Wiley & Sons; 2011.

[49] Genceli OF. Heat Exchanger. Birsen Publication; 2005.

[50] Kakac S, Liu H, Pramuanjaroenkij A. Heat exchangers: selection, rating, and thermal design. CRC Press; 2002.

[51] Fudholi A, Zohri M, Rukman NSB, Nazri NS, Mustapha M, Yen CH, et al. Exergy and sustainability index of photovoltaic thermal (PVT) air collector: A theoretical and experimental study. *Renew Sustain Energy Rev* 2019;100:44–51.

[52] Tugcu A, Arslan O, Kose R, Yamankaradeniz N. Thermodynamics and economical analysis of geothermal assisted absorption refrigeration system: Simav case study. *J Therm Sci Technol* 2016;36:143–59.

[53] Roy J, Sarkar P, Biswas S, Choudhury A. Predictive equations for CO_2 emission factors for coal combustion, their applicability in a thermal power plant and subsequent assessment of uncertainty in CO_2 estimation. *Fuel* 2009;88(5):792–8.

[54] Arslan O, Acikkalp E, Genc G. A multi-generation system for hydrogen production through the high-temperature solid oxide electrolyzer integrated to 150 MW coal-fired steam boiler. *Fuel* 2022;315:123201.

[55] Arslan O. ANN-based Determination of Optimum Working Conditions of Residential Combustors with Respect to Optimum Insulation. *Energy Sources Part A* 2014;36(23):2603–12.

[56] Arslan O, Arslan AE. Performance evaluation and multi-criteria decision analysis of thermal energy storage integrated geothermal district heating system. *Process Saf Environ Prot* 2022;167:21–33.

[57] Arslan O, Arslan AE, Boukelia TE. Modelling and optimization of domestic thermal energy storage based heat pump system for geothermal district heating. *Energ Buildings* 2023;282:112792.

[58] Arslan AE, Arslan O, Kurtbas I. Exergoeconomic and exergoenvironmental based multi-criteria optimization of a new geothermal district heating system integrated with thermal energy storage driven heat pump. *Journal of Building Engineering* 2023;73:106733.

[59] Kayapinar O, Arslan AE, Arslan O, Genc MS. Multi-criteria analysis on the simulation-based optimal design of a new stack-type natural ventilation system for industrial buildings. Therm Sci Eng Prog 2024;51:102657.

[60] Peters M.L., & Zelewski S. (2006). Efficiency Analysis Under Consideration of Satisficing Levels for Output Quantities. In Proceedings of the 17th Annual Conference of the Production and Operations Management Society (POMS), April 28-May 01, Boston, USA.

[61] Arslan AE, Arslan O, Kandemir SY. AHP–TOPSIS hybrid decision-making analysis: Simav integrated system case study. *Journal of Thermal Analysis and Calorimerty* 2021;145:1191–202.

[62] Arslan AE. Do subjective norms and willingness to overpay have an effect on the intention to use renewable energy sources. *Anadolu Univ J Soc Sci* 2022;22(4):1221–54.

[63] Sundar LS, Punnaiah V, Sharma KV, Chamkha AJ, Sousa AC. Thermal entropy and exergy efficiency analyses of nanodiamond/water nanofluid flow in a plate heat exchanger. *Diam Relat Mater* 2021;120:108648.

[64] Erdogan A, Colpan CO, Cakici DM. Thermal design and analysis of a shell and tube heat exchanger integrating a geothermal based organic Rankine cycle and parabolic trough solar collectors. *Renew Energy* 2017;109:372–91.

[65] Venkatesaperumal R, Syed Jafar K, Elumalai PV, Abbas M, Cuce E, Shaik S, et al. Heat Transfer Studies on Solar Parabolic trough Collector Using Corrugated Tube Receiver with Conical Strip Inserts. *Sustainability* 2022;15(1):378.

[66] Amalfi RL, Vakili-Faraha, Thome JR. Flow boiling and frictional pressure gradients in plate heat exchangers. Part 2: Comparison of literature methods to database and new prediction methods. *Int J Refrig* 2016;61:185–203.

[67] Turchi, C. S., Boyd, M., Kesseli, D., Kurup, P., Mehos, M. S., Neises, T. W., ... & Wendelin, T. (2019). CSP systems analysis-final project report (No. NREL/TP-5500-72856). National Renewable Energy Lab. (NREL), Golden, CO (United States).

[68] Reddy R.G. (2013). Novel molten salts thermal energy storage for concentrating solar power generation. Technical Report DE-FG36-08GO18153, University of Alabama (UA), Tuscaloosa, Alabama, USA.

[69] Turton R, Bailie RC, Whiting WB, Shaeiwitz JA. *Analysis, synthesis and design of chemical processes*. Pearson Education; 2008.

[70] Cost indices. (2023). https://toweringskills.com/financial-analysis/cost-indices/ [accessed 7 May 2023].

[71] MENR (Ministry of Energy and Natural Resources of Turkish Republic). Electricity price for Renewables, https://www.enerji.gov.tr/tr-TR/Sayfalar/Elektrik; 2022 [accessed 05 May 2022].

[72] Saaty TL. Decision making with the analytic hierarchy process. *International Journal of Services Sciences* 2008;1(1):83–98.

[73] Saaty TL. Multi-criteria Decision Making: The Analytic Hierarchy Process. 2nd Ed. Pittsburgh: RWS Publications; 1990.

[74] Kizielewicz B, Sałabun W. SITW method: a new approach to re-identifying multi-criteria weights in complex decision analysis. Spectrum of Mechanical Engineering and Operational Research 2024;1:215–26.

[75] Więckowski J, Kizielewicz B, Shekhovtsov A, Sałabun W. RANCOM: A novel approach to identifying criteria relevance based on inaccuracy expert judgments. *Eng Appl Artif Intel* 2023;122:106114.